The Pennsylvania State University
The Graduate School
College of Engineering

ALL-OPTICAL IMAGE PROCESSING WITH NONLINEAR LIQUID CRYSTALS

A Dissertation in
Electrical Engineering

by

KUAN-LUN HONG

Submitted in Partial Fulfillment
of the Requirements
for the Degree of

Doctor of Philosophy

August 2013

The dissertation of Kuan-Lun Hong was reviewed and approved* by the following:

Iam-Choon Khoo
William E. Leonhard Professor of Electrical Engineering
Dissertation Advisor
Chair of Committee

Julio Urbina
Associate Professor of Electrical Engineering

Zhiwen Liu
Associate Professor of Electrical Engineering

Jian Xu
Associate Professor of Engineering Science and Mechanics
Adjunct Professor of Electrical Engineering

Kultegin Aydin
Professor of Electrical Engineering
Head of the Department of Electrical Engineering

* Signatures are on file in the Graduate School

ABSTRACT

Liquid crystals are fascinating materials because of several advantages such as large optical birefringence, dielectric anisotropic, and easily compatible to most kinds of materials. Compared to the electro-optical properties of liquid crystals widely applied in displays and switching application, transparency through most parts of wavelengths also makes liquid crystals a better candidate for all-optical processing. The fast response time of liquid crystals resulting from multiple nonlinear effects, such as thermal and density effect can even make real-time processing realized. In addition, blue phase liquid crystals with spontaneously self-assembled three dimensional cubic structures attracted academic attention.

In my dissertation, I will divide the whole contents into six parts. In Chapter 1, a brief introduction of liquid crystals is presented, including the current progress and the classification of liquid crystals. Anisotropy and laser induced director axis reorientation is presented in Chapter 2. In Chapter 3, I will solve the electrostrictive coupled equation and analyze the laser induced thermal and density effect in both static and dynamic ways. Furthermore, a dynamic simulation of laser induced density fluctuation is proposed by applying finite element method. In Chapter 4, two image processing setups are presented. One is the intensity inversion experiment in which intensity dependent phase modulation is the mechanism. The other is the wavelength conversion experiment in which I can read the invisible image with a visible probe beam. Both experiments are accompanied with simulations to realize the matching between the theories and practical experiment results. In Chapter 5, optical properties of blue phase liquid crystals will be introduced and discussed. The results of grating diffractions and thermal refractive index gradient are presented in this chapter. In addition, fiber arrays imaging and switching with BPLCs will be included in this chapter. Finally, I will give a brief summary and mention a few future researches in Chapter 6.

TABLE OF CONTENTS

LIST OF FIGURES

LIST OF TABLES

ACKNOWLEDGEMENTS

I wish to express my gratitude to my thesis advisor, Professor I. C. Khoo, for his patient guidance and encouragement throughout the course of this research. I would also like to thank the members of my doctoral committee, Dr. Julio Urbina, Dr. Zhiwen Liu, and Dr. Jian Xu, for their advice towards the completion of this work.

I would like to extend my appreciation to my friends and colleagues: Dr. Andres Diaz, Dr. Mike Stinger, Dr. Justin Liou, Dr. Junbin Huang, Dr. Yi Ma, and Shuo Zhao from the Nonlinear Optics Lab, for many fruitful discussions and technical support.

Last but not least, full gratitude goes to my parents and family for their unconditional love and support that have kept me going over the past five years.

CHAPTER 1 LIQUID CRYSTALS – A BRIEF INTRODUCTION

1.1 Brief History and Current Progress

Liquid crystals are wonderful materials widely investigated around the world as a matter in an intermediate phase which has both properties of solid crystals and isotropic liquids. The beginning of liquid crystals was uncovered by an Australia scientist, Reinitzer in 1888, observing two distinct melting points in a material as cholesteryl benzoate [1]. By increasing the temperature, he found the crystal transferred into a nazy liquid and further a clear liquid. This nazy phase later was also called mesogens, which was identified later by Friedel in early 1920s [2]. Then in 1991 Pierre-Gilles de Gennes is the Nobel Laureate in Physics for his studies involving liquid crystals and polymers [3]. The following development of liquid crystals was deeply influenced by his work [4]. Because of nonlinearity and electro-optical effect of liquid crystals, this special material was applied in many areas, such as huge success in liquid crystal display. Not just display, some detectors and protectors were invented by applying various properties of liquid crystals [5-9]. In addition, liquid crystals are seen as a good tuning material to give an adjustment of optical properties to nano-structure and photonic crystal fibers [10-14]. Recently, the blue phase liquid crystals, one kind of cholesteric liquid crystals, attracted lots of attention in the past decades [15-18, 108-109]. The development of this mysterious material never ends and still waits for exploration.

1.2 Classification and Structure

There are various ways to classify liquid crystals. The most basic way to classify is according to the physical parameters which control the existence of the liquid crystalline phases. Three different kinds of liquid crystals, lyotropic, polymeric, and thermotropic appear in liquid crystalline phases as a function of concentration, constituents, molecular architectural arrangement of the mesogenic monomer, and temperature, respectively.

Lyotropic liquid crystals, which can be obtained with an appropriate concentration of a material and some solvent, were first discovered in the mixtures of myelin and water. The concentration of solvent will control the existence of liquid crystal phase. The lyotropic liquid crystals are mainly used in biological studies [19].

Polymeric liquid crystals behaving like monomers liquid crystals have both the properties of polymers and liquid crystals and have much higher viscosity. According to the molecules arrangement and flexibility, the polymeric liquid crystals can be further divided into several types. More details can be found in reference [20]. In general, polymeric liquid crystals are applied in optical storage.

Thermotropic liquid crystals exhibit liquid crystal phase as a function of temperature and are most widely used. If the temperature is too high, the ordering of liquid crystals will be broken and then turn to a liquid phase. If the temperature is too low, liquid crystals will turn into a crystal form. The liquid crystal I used in this dissertation belongs to this category. There are three main classes of thermotropic liquid crystals, nematic, cholesteric, and smectic, depending on molecule arrangement and the amount of order. We will discuss thermotropic liquid crystal further in the next session [4, 19].

1.3 Thermotropical Liquid Crystals

Nemetic liquid crystal phase is characterized by molecules with no positional order but tendency to align in the same direction, illustrated as Fig. 1.1.

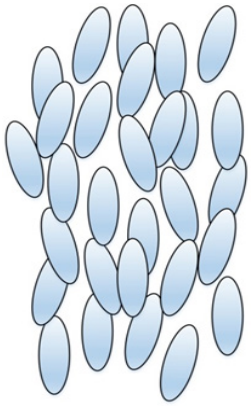

Fig. 1.1 Schematics of nematic liquid crystal phase molecule alignment

Smectic liquid crystals keep the direction order of nematic liquid crystals and maintain a layer positional order, shown as below:

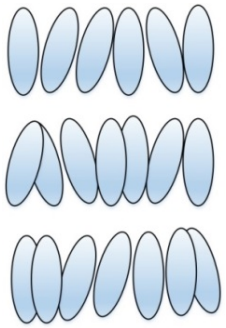

Fig. 1.2 Schematics of smectic liquid crystal phase molecule alignment

Cholesterics liquid crystals are also called chiral nematic liquid crystals, keeping the same physical properties. In this structure, the directors actually form in a continuous helical pattern, illustrated as Fig. 1.3.

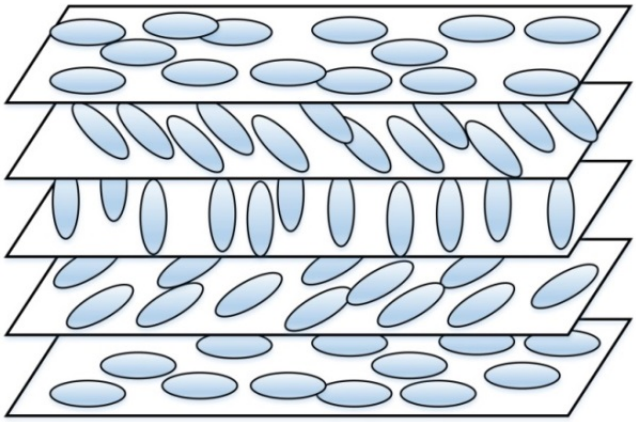

Fig. 1.3 Schematics of cholesteric phase liquid crystal molecule alignment

We may regard nematics as a special case of cholesterics with the pitch $p \to \infty$, illustrated as Fig. 1.4 (a). Since the optical property of the nematic, a uniaxial material, is integrally related to the director axis, the helical arrangement of the latter in a cholesteric certainly introduces new optical properties, particularly in the propagation and reflection of light from cholesteric liquid crystal cells. Fig. 1.4 (b) and Fig. 1.4 (c) show two commonly occurring director axis alignments: planar twisted and fingerprint, respectively.

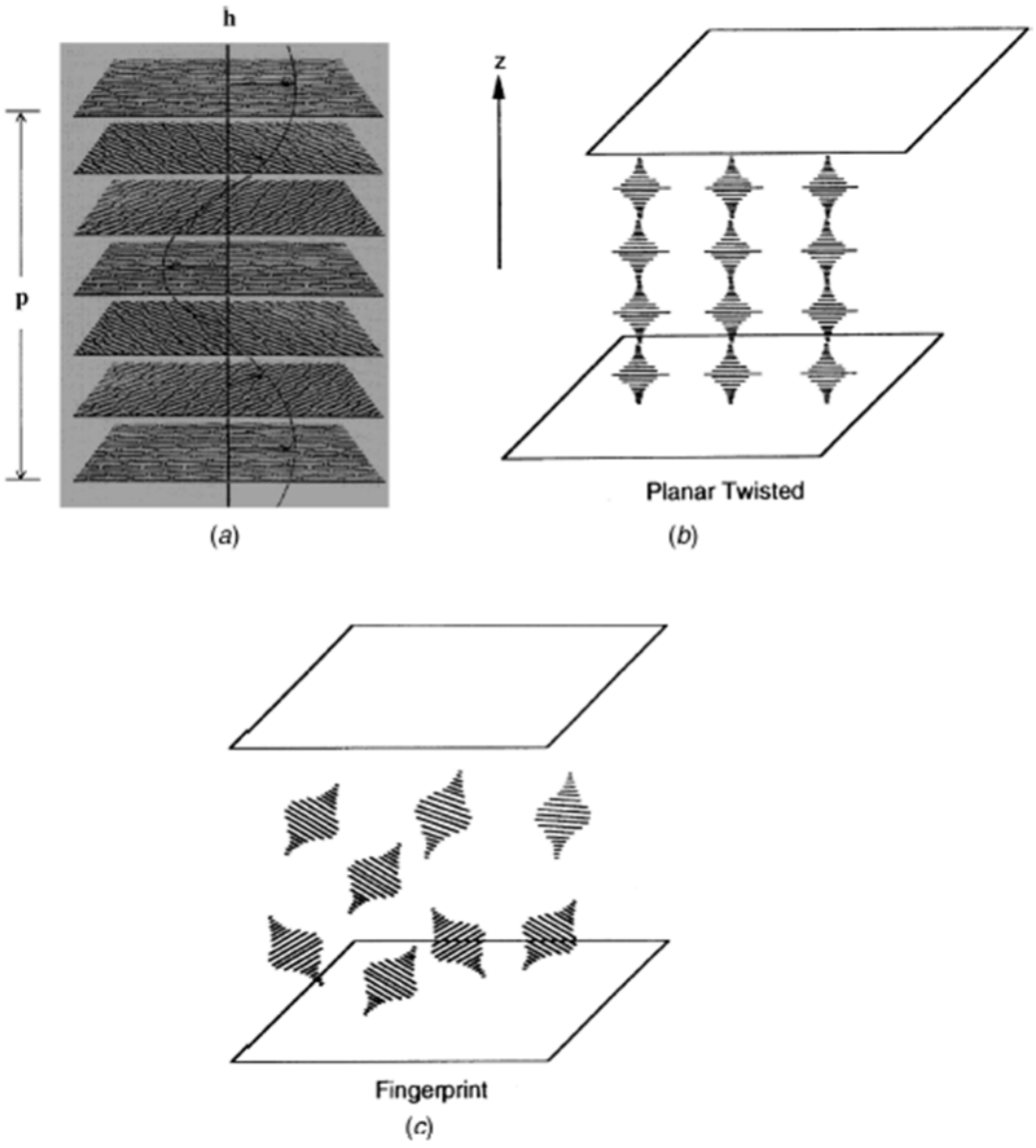

Fig. 1.4 (a) Helical arrangement of the director axis in a cholesteric liquid crystal; *p* is the pitch and h is the helix direction. Two typical cholesteric liquid crystal cell shown in (b) planar twisted and (c) fingerprint [28]

Nematic and smectic liquid crystals are mostly rod-shaped and are generally formed with similar chemical structures. The most stable series usually consist of a rigid body, formed by at least two aromatic groups, and are attached by one or more aliphatic chains. There are numerous possible combinations and we will not list all of them. Here

are just a few of the common combinations, illustrated as Fig. 1.5. Furthermore, in addition to these three main phases, there are many derivatives or newly emerged liquid crystals phases. Cholesteric blue phase has been identified as an effective one.

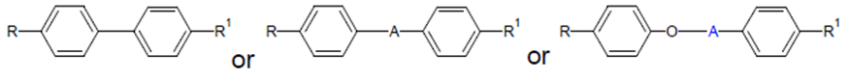

R	A	R'
C_nH_{2n+1}	- CH=N-	R
C_nH_{2n+1}-O	-COO-	-C≡N
C_nH_{2n+1}-COO	-C≡C-	-Cl
C_nH_{2n+1}-OCOO		-Br

Fig. 1.5 Some common liquid crystal structural combinations

1.4 Mixtures and Composites

About the liquid crystals we used in laboratory, there are still some disadvantages. For example, the temperature range is limited in a narrow range. It is difficult to apply the liquid crystals in practical industries within the temperature limitation. Therefore, there are many ways to modify the properties of liquid crystals. For example, 5CB (4-Cyano-4'-pentylbiphenyl) is produced by modifying biphenyl in a linear manner. Its molecular structure shows as below and was first synthesized by George William Gray, Ken Harrison, and J.A. Nash at the University of Hull in 1972. The size of 5CB is around 20Å and the temperature range of nematic phase is from 18°C (melting point) to 35°C (clearing point) [21, 22].

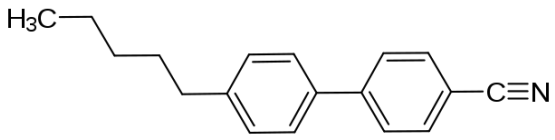

Fig. 1.6 Molecular structure of 5CB (4-Cyano-4'-pentylbiphenyl)

Also another liquid mixture E7 is the mixture of four liquid crystals [23], illustrated as Fig. 1.7. With appropriate concentration the temperature in crystal phase is lifted tremendously, we can explain the advantage of the mixture of liquid crystals with Fig. 1.8. Both of liquid crystals in Fig. 1.8 have small nematic ranges, $T_i - T_n$ and $T_i' - T_n'$, respectively. However, with 50% of each liquid crystal, the nematic range can raise several times, $T_i^m - T_n^m$.

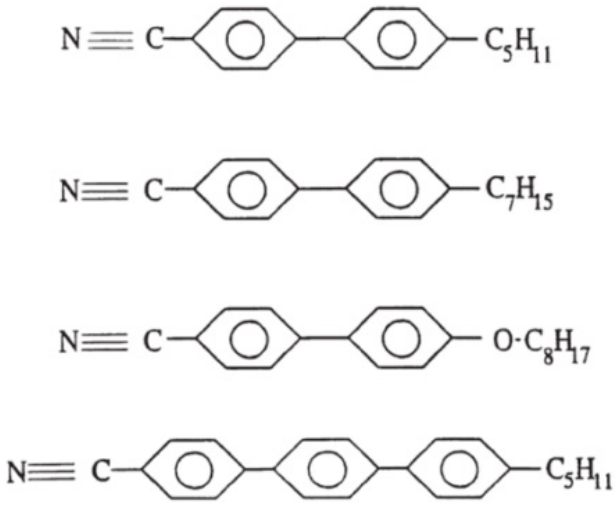

Fig. 1.7 Molecular structure of four constituents making up the liquid crystal E7

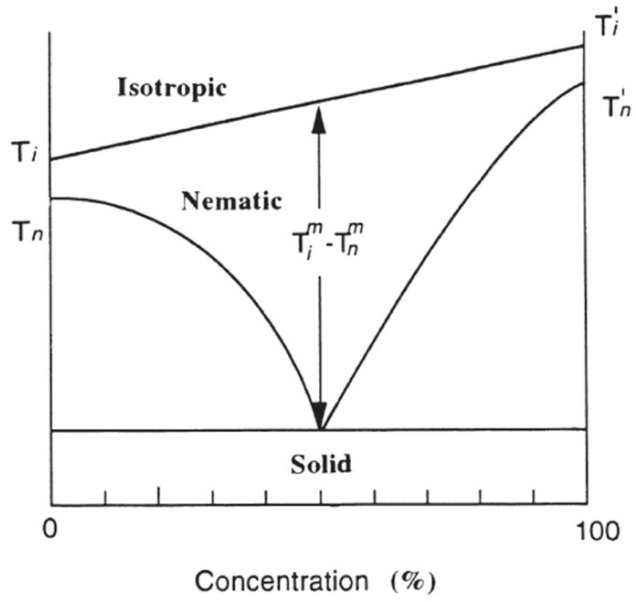

Fig. 1.8 Phase diagram of the mixture of two liquid crystals [28]

The absorption of pure liquid crystal is determined by the electronic properties of molecules in the liquid crystal. Since most liquid crystals are aromatic compounds, containing one or more aromatic rings, the energy levels of aromatic rings play a major role in the liquid crystal absorptions. The electronic orbital transitions of these rings give rise to UV absorptions, and rovibrational transitions of large molecules induce infrared absorption.

In addition, as a result of the high transparency in visible regime, doping dyes to increase the absorption and lift the nonlinearity in visible spectrum are very popular. Especially in my experiment, the laser wavelength is around visible (532nm or 632nm) and near infrared (1550nm), so appropriate dyes doped in the liquid crystals largely lift the nonlinear effect. In 1991, Janossy et al. [45] reported the huge thermal nonlinearity with dye-doped liquid crystals. The nonlinearity is two orders of magnitude higher than the pure liquid crystals with 1% - 2% dyes doped. Khoo [46], also reported the nonlinear coefficient as high as $6cm^2/W$. The other researches about polymer-doped liquid crystals or metal-doped liquid crystals also have advantages in different application [24-

27]. The Table 1.1 lists the character and the order of nonlinearity of nematic liquid crystals in different condition. From Fig. 1.9, we can even have a better understanding about the development of nonlinear liquid crystals, more than ten orders of magnitude increase in the n_2 observed since 1979.

Table 1.1 Nonlinear refractive index coefficients of nematic liquid crystals in different condition

Nematic Liquid Crystals	**Order of n_2 (cm^2/W)**
LC in isotropic phase	$\sim 10^{-12} - 10^{-11}$
Purely optically induced	$\sim 10^{-4} - 10^{-3}$
Thermal and order parameter change (Crystal phase)	$\sim 10^{-5} - 10^{-3}$
Photorefractive – C60 doped	$\sim 10^{-3} - 10^{-2}$
Methyl red doped	$\sim 1 - 10^{3}$

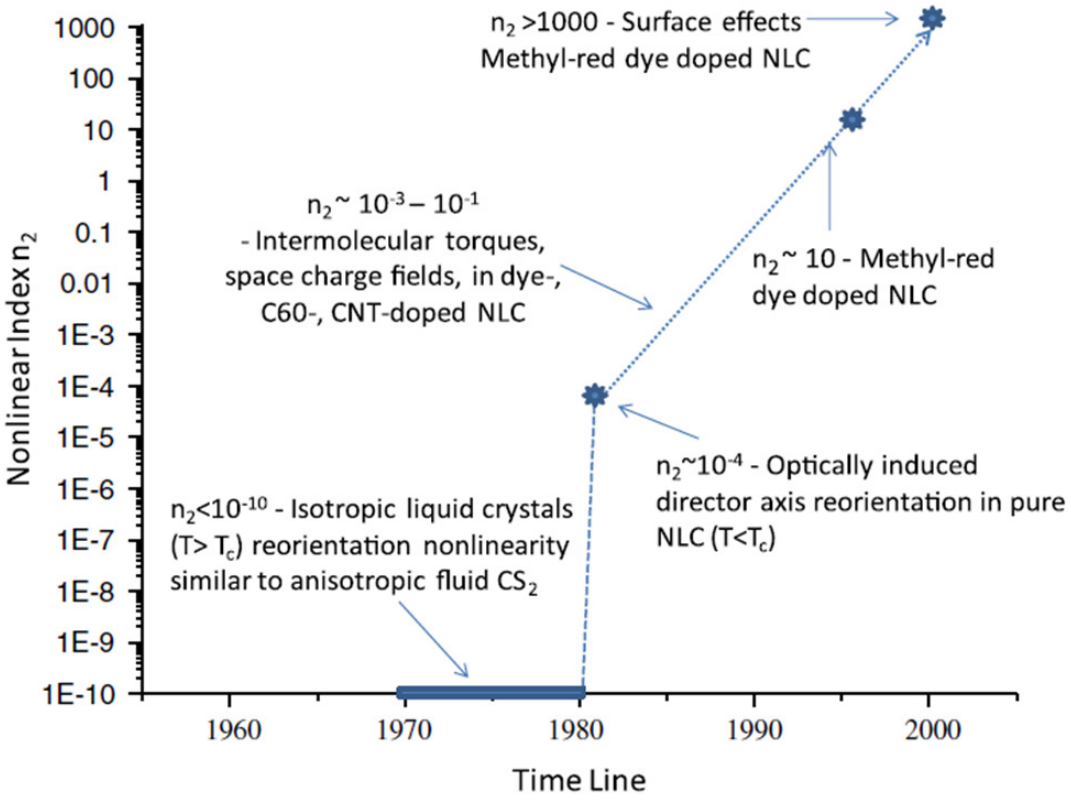

Fig. 1.9 A historical snapshot of some remarkable milestones for the nonlinear index coefficients n_2 associated with laser induced crystalline axis reorientation in NLCs for the time period paralleling nonlinear optics evolution [47]

CHAPTER 2 OPTICAL PROPERTIES OF LIQUID CRYSTALS

2.1 Nematic Liquid Crystals - Anisotropic

Compared to isotropic materials which have all identical properties in all directions, the properties of anisotropic materials depend on the direction. In nematic liquid crystals, when the light interacts with the nematic liquid crystals, different polarizations of light incident on the liquid crystals will see different refractive indices.

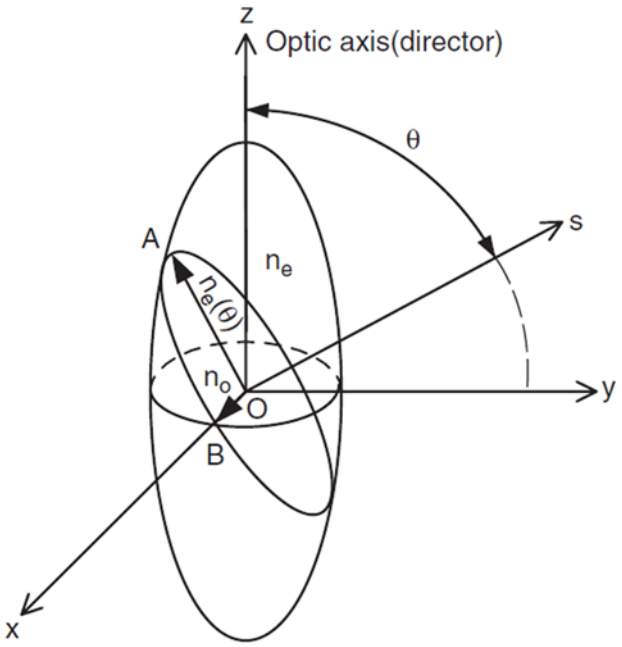

Fig. 2.1 The refractive index ellipsoid of a uniaxial liquid crystal phase with the optic axis parallel to the z axis

As shown as Fig. 2.1, an uniaxial index ellipsoid such as nematic liquid crystals the refractive index are the same in the x-axis and y axis, denoted as n_o and the z axis,

also named direct axis , the refractive index denoted as n_e, the index ellipsoid equation for uniaxial nematic liquid crystals shows as:

$$\frac{x^2}{n_o^2}+\frac{y^2}{n_o^2}+\frac{z^2}{n_e^2}=1 \tag{2.1}$$

Consider a polarized plane wave propagating in a direction making an angle θ with the z axis. Two orthogonal vectors can be defined as an ordinary wave and an extraordinary wave. The ordinary wave keeps the same refractive index in any propagation direction:

$$n_o(\theta)=n_o \tag{2.2}$$

From the Eq. (2.3), we can get the refractive index expression of extraordinary wave which is a function of θ.

$$n_e(\theta)=\frac{n_e n_o}{\left[n_e^2 cos^2(\theta)+n_o^2 sin^2(\theta)\right]^{1/2}} \tag{2.3}$$

Two special cases: if the light propagates in z direction, the refractive index of the ordinary wave and extraordinary wave are n_o. If the light propagates in x or y direction then the extraordinary wave is n_e whereas the ordinary wave is n_o. In the following three main structures of liquid crystals, homogeneous (planar), twisted, and homeotropic, we can have a better understanding.

The birefringence is generally defined as

$$\Delta n(\theta)=n_e(\theta)-n_o(\theta) \tag{2.4}$$

There are positive birefringence liquid crystals ($n_e > n_o$) and negative birefringence liquid crystals ($n_o > n_e$). Typically the value of n_e of 5CB we used most often is 1.75; that of n_o is 1.55 [28, 29]. Fig. 2.2 shows the measured birefringence of three nematic liquid crystals from the UV (400nm) to the far infrared (16μm). A large average birefringence 0.2 is observed in E7 and NP5. In addition, the birefringence is well defined in visible as well as the infrared regime.

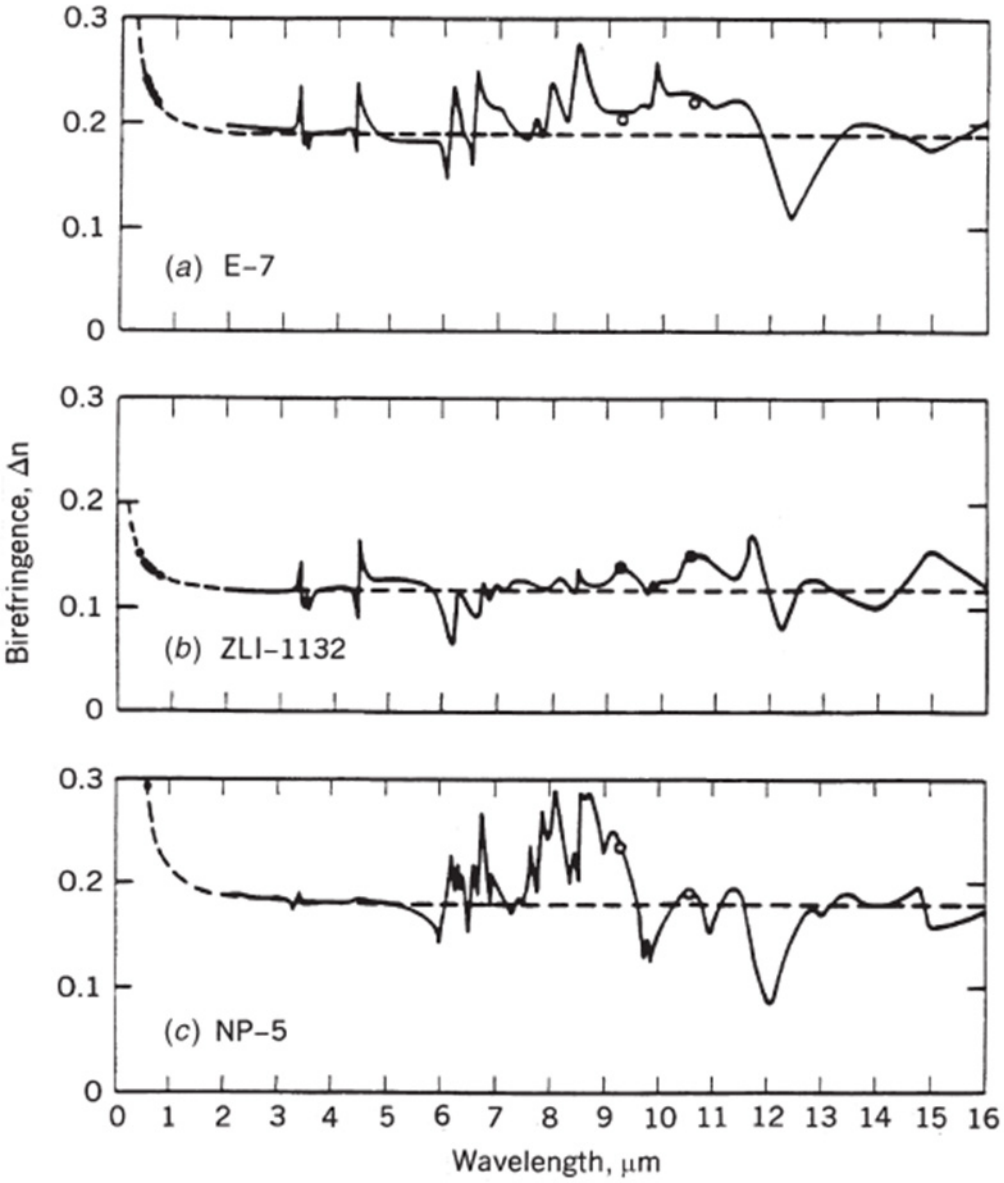

Fig. 2.2 Measured birefringence of three nematic liquid crystals [28]

2.2 Liquid Crystal Cells

Because of the anisotropic properties, the alignment of liquid crystals will decide the optical properties. For nematic liquid crystals two alignments are commonly used: One is homogeneous and the other is homeotropic, depicted as Fig. 2.3.

HTAB (hexadecyl-trimethy1~ammoniumbromide) is used on the surface of glasses to align the liquid crystals in a standing form [30]. On the other hand, PVA (polyvinyl alcohol) is commonly employed way to make a planar one. Rub and create strain on the polymer first, and then the liquid crystal molecules will automatically align along the rubbed direction.

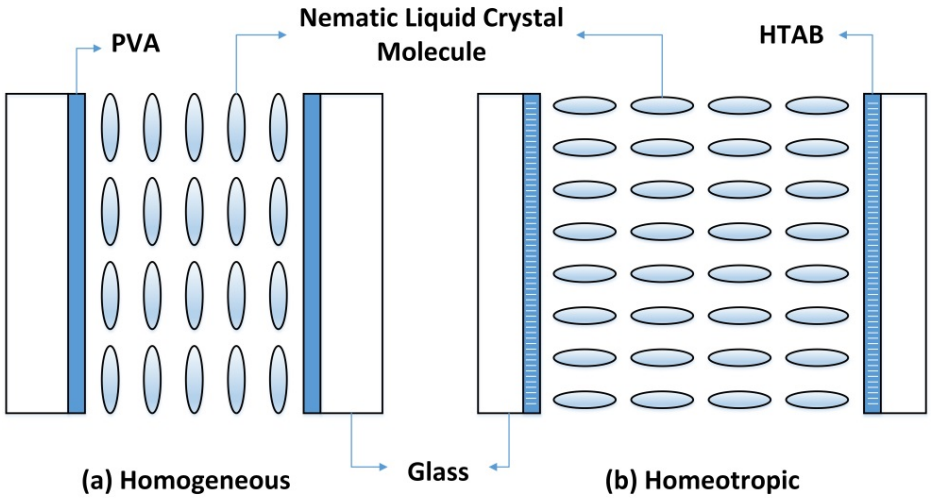

Fig. 2.3 Nematic liquid crystal cells (a) homogeneous or planar aligned and (b) homeotropic aligned

Based on these two alignments, many other alignments are derived such as hybrid, twisted, super-twisted etc. One special alignment is twisted alignment. The process is similar to the homogeneous but the difference is to place the two glasses with rubbed PVA layers in orthogonal direction instead of same direction. Because of the continue properties, the direct axis of liquid crystals will rotate once the thickness is large enough. This explains the Mauguin condition. For a TNLC cell, to rotate the light polarization effectively, $d\Delta n$ must be much larger than $\lambda/2$ [31]. With two parallel polarizers in front and back of the TNLC sample, the simulation results of optical transmission can be illustrated as Fig. 2.4.

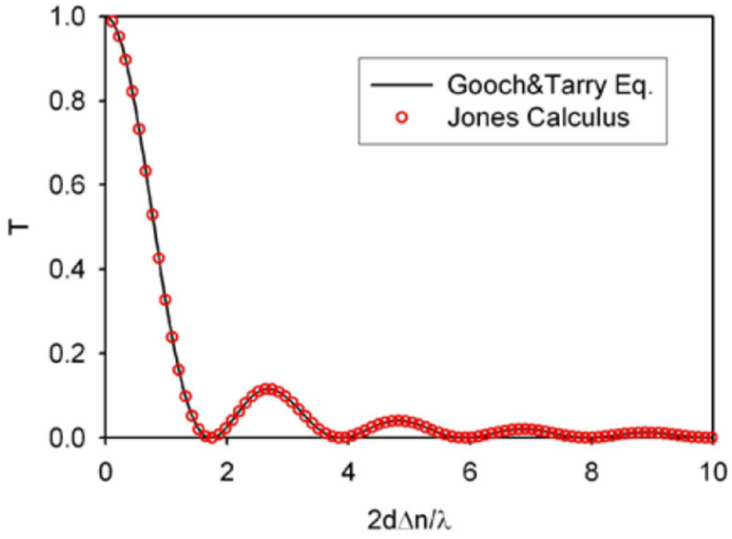

Fig. 2.4 Transmission curve of a TNLC sample as a function of thickness and anisotropy

2.3 Elastic Continuum Theory and Field Torque

After discussing about the anisotropic property, we may try to understand the interaction between the field and the liquid crystals, especially the optical field. When an external field interacts with liquid crystals, some deformation occurs. Not like the solids a huge stress is created; instead in liquid crystals the fluid properties appear and involve the change in the direct axis $\hat{n}(\vec{r})$. For nematic liquid crystals, twist, splay, and bend are three principal direct axis deformations, illustrated as Fig. 2.5. The theoretical formulas about the relationship between the deformation energies and spatial change in $\hat{n}(\vec{r})$ were first developed by Frank [32].

$$\text{splay}: \ f_1 = \frac{1}{2}K_1(\nabla \cdot \hat{n})^2 \tag{2.5}$$

$$\text{twist}: \ f_2 = \frac{1}{2}K_2(\hat{n} \cdot \nabla \times \hat{n})^2 \tag{2.6}$$

$$\text{bend}: \ f_3 = \frac{1}{2}K_3(\hat{n} \times \nabla \times \hat{n})^2 \tag{2.7}$$

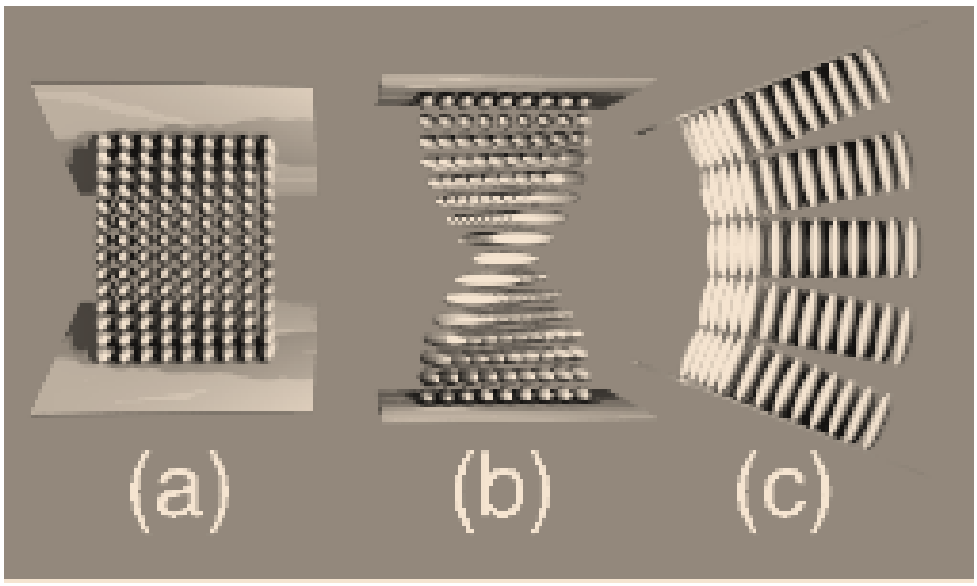

Fig. 2.5 Elastic distortions of a nematic liquid crystal: (a) splay (b) twist (c) bend [33]

where K_1, K_2, K_3 are the frank elastic constants for distortion of splay, twist, and bend, respectively. For most nematic liquid crystals, K_3 is larger than the others. The order of the frank elastic constants is around $10^{-11}N$.

Without the external fields, the total free energy of the liquid crystal system can be expressed as

$$F_{total} = \int F_d + F_{surface}\, dV \tag{2.8}$$

where $F_d = f_1 + f_2 + f_3$ is the total distortion energy, and $F_{surface}$ is the surface energy which depicts the treatment between the boundary and the liquid crystals. Generally there are two conditions describing the boundary. One is the hard boundary condition which is treated as a constant energy and do not count for the dynamical equation with fields induced effect. The other is soft boundary condition in which the surface energy will change when the fields are involved [34, 35]. The condition is more complex, and in this dissertation, we treat the boundary between the glass and liquid crystals as a hard boundary.

Meanwhile, when the field interacts with the liquid crystals, the system will realign itself to fulfill the minimum elastic free energy. We take twisted nematic liquid crystal as an example to understand the position dependent reorientation angle as shown in Fig. 2.6.

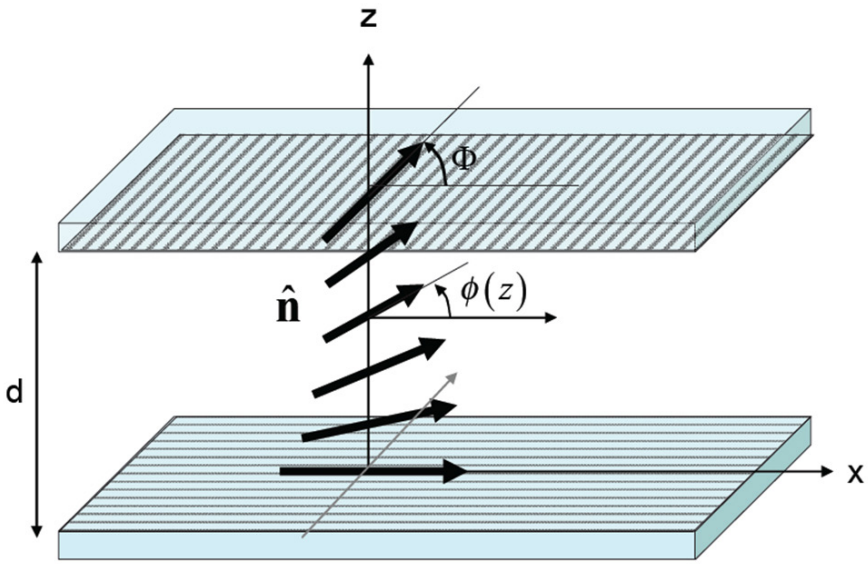

Fig. 2.6 The director orientation of a twist-nematic liquid crystal thin film sandwiched between two glass slides

At the top and bottom boundaries, the directors are set to parallel to the x-axis ($\emptyset(z=0)=0$) and a specific angle ($\emptyset(z=d)=\phi$). Assume the liquid crystal molecules will remain in the same plane and only twist along the z-axis. Hard boundary is considered. The refractive index n in the position z with an orientation $\emptyset$ can be expressed as:

$$n = (cos\emptyset, sin\emptyset, 0) \tag{2.9}$$

In addition, among three deformation, splay, twist, bend, only twist deformation (f_2) exists in this twist system, and the system in rectangular coordinate can be simplified as:

$$n \cdot \nabla \times n = (cos\emptyset, sin\emptyset, 0) \cdot \begin{vmatrix} \hat{\imath} & \hat{\jmath} & \hat{k} \\ \frac{\partial}{\partial x} & \frac{\partial}{\partial y} & \frac{\partial}{\partial z} \\ cos\emptyset & sin\emptyset & 0 \end{vmatrix} \tag{2.10}$$

$$= -cos^2\emptyset \cdot \frac{\partial \emptyset}{\partial z} - sin^2\emptyset \cdot \frac{\partial \emptyset}{\partial z}$$

$$= -\frac{\partial \emptyset}{\partial z}$$

Then the twist deformation (f_2) can be expressed as:

$$f_2 = \frac{1}{2} K_2 (\frac{\partial \emptyset}{\partial z})^2 \tag{2.11}$$

To minimize twist deformation, which is involved with $\frac{\partial \emptyset}{\partial z}$ and $\emptyset(z)$, we apply the Euler-Lagrange [10]. In this case, the Euler-Lagrange equation for $f(\emptyset, \emptyset', z)$ can be expressed as:

$$\frac{\partial f}{\partial \emptyset} - \frac{d}{dz}\left(\frac{\partial f}{\partial \emptyset'}\right) = 0 \tag{2.12}$$

If the Eq. (2.12) is fulfilled, the minimum f can be achieved, expressed as

$$0 - \frac{d}{dz}\left(K_2 \frac{\partial \emptyset}{\partial z}\right) = 0 \tag{2.13}$$

Thus

$$K_2 \frac{d^2\emptyset}{dz^2} = 0 \tag{2.14}$$

Therefore, we can get

$$\emptyset(z) = \frac{\phi}{d} z \tag{2.15}$$

Without outside fields, we prove the twisted nematic liquid crystals will realign themselves linearly. After understanding the natural property of liquid crystals, we investigate the field involved situation. From electrodynamics we first understand the expression of torque Γ when an electric field E is applied on a dipole:

$$\Gamma = \mathrm{P} \times \mathrm{E} \tag{2.16}$$

To simplify this equation, we can replace the electric dipole moments P with the electric displacement field D without influencing the calculation.

$$\Gamma = \mathrm{D} \times \mathrm{E} \tag{2.17}$$

In vector notation, we decompose D into the components parallel and perpendicular to the director n

$$\mathrm{D} = D_{\perp} + D_{\parallel} = \varepsilon_{\perp} E_{\perp} n_{\perp} + \varepsilon_{\parallel} E_{\parallel} n_{\parallel} \tag{2.18}$$

E = $(E_{\perp}, 0, E_{\parallel})$, then we have

$$E_{\perp} n_{\perp} = E - E_{\parallel} n_{\parallel} = E - (n \cdot E) n \tag{2.19}$$

$$\mathrm{D} = \varepsilon_{\perp} [E - (n \cdot E) n] + \varepsilon_{\parallel} (n \cdot E) n \tag{2.20}$$

$$= \varepsilon_{\perp} E + (\varepsilon_{\parallel} - \varepsilon_{\perp}) \, (n \cdot E) n$$

Then we get

$$\Gamma = \mathrm{D} \times \mathrm{E} = \Delta\varepsilon (n \cdot E)(n \times E) \tag{2.21}$$

This torque generated from the applied electric field E is exerting on the liquid crystal molecules and is positive if positive anisotropy $\Delta\varepsilon > 0$. Thus molecules have the tendency to align their director n with the applied electric field E. For the material with negative anisotropy $\Delta\varepsilon < 0$, the molecules tend to align the director normal to the field. It disturbs the original equilibrium state (the one defined by free elastic energy minimization and boundary conditions) and will reach a new equilibrium when the molecules reach the new energy minimum. This electric field can be a DC field, an AC field, or an optical field. The potential energy of the dipolar molecules caused by this applied electric field is

$$\mathrm{U} = \int dU = -\int P \cdot dE \tag{2.22}$$

$$= -\int (D - \varepsilon_0 E) \cdot dE$$

$$\mathrm{U} = -\int[\varepsilon_{\perp}E + (\varepsilon_{\parallel} - \varepsilon_{\perp})\,(n \cdot E)n] \cdot \mathrm{dE} + \int \varepsilon_0 E \cdot dE \qquad (2.23)$$

$$= -\frac{\varepsilon_{\perp} - \varepsilon_0}{2} E^2 - \frac{1}{2}\Delta\varepsilon\langle(n \cdot E)^2\rangle$$

where θ is the angle between n and E. The first term at the right-hand side is independent of orientation angle θ and is the constant electric energy stored in the space and is generally not considered in discussion. Therefore, the energy associated with the application of electric field can be written as

assume U = 0 at $\theta = 0$

$$\mathrm{U}(\theta) = \frac{1}{2}\Delta\varepsilon E^2 sin^2\theta \qquad (2.24)$$

$$\mathrm{W} = \int_0^{\theta} \Gamma \cdot \mathrm{d}\theta = \int_0^{\theta} \Delta\varepsilon(n \cdot E)(n \times E) \cdot \mathrm{d}\theta \qquad (2.25)$$

$$= \frac{1}{2}\Delta\varepsilon E^2 sin^2\theta$$

A 4π factor may be added in this equation since we will use the Gaussian unit in the following calculation. The torque can be expressed as:

$$\Gamma = \frac{\Delta\varepsilon}{4\pi}(n \cdot E)(n \times E) \qquad (2.26)$$

2.4 Laser Induced Reorientation

In the nematic liquid crystals, the reorientation of the direct axis of liquid crystals arises as a result of tendency to minimum free energy [36-39]. Laser-induced single molecular orientations in liquid crystals have been investigated widely [48-51]. Instead of the twisted nematic liquid crystals, we introduce another alignment to understand other elastic deformation. Consider, for example the interaction geometry depicted as Fig. 2.7, a linear polarized laser incident on a homeotropic nematic liquid crystals.

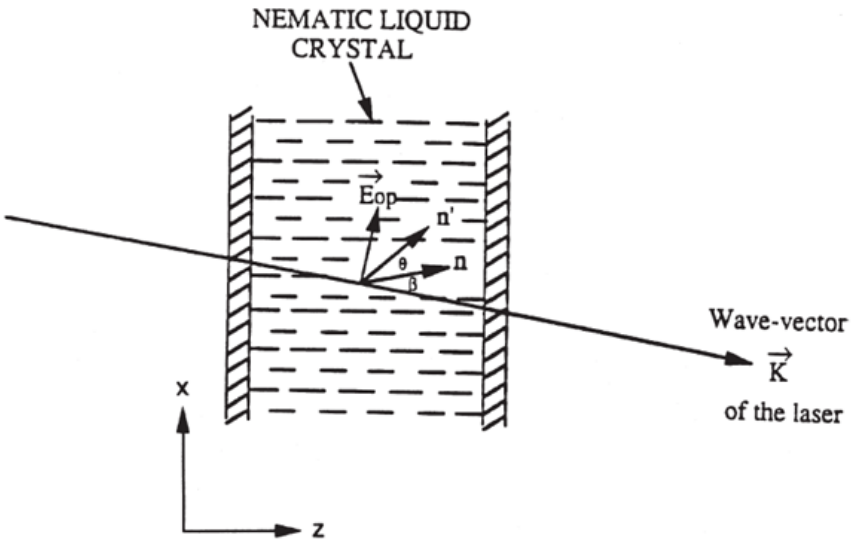

Fig. 2.7 Interaction of a linear polarized laser with a homeotropically aligned nematic liquid crystal film [28]

In this geometry, the total elastic free energy F_d is

$$F_d = F_1 + F_3 = \frac{1}{2}K_1(\nabla \cdot \hat{n})^2 + \frac{1}{2}K_3(\hat{n} \times \nabla \times \hat{n})^2 \tag{2.27}$$

From the Fig. above, we have

$$\vec{E}_{op} = E_x\hat{x} + E_z\hat{z} \tag{2.28}$$

$$\hat{n} = sin\theta"\hat{x} + cos\theta"\hat{z} \tag{2.29}$$

Where $\theta" = \theta + \beta$, then we have

$$(\nabla \cdot \hat{n})^2 = sin^2\theta" \left(\frac{\partial\theta}{\partial z}\right)^2 \tag{2.30}$$

$$(\hat{n} \times \nabla \times \hat{n})^2 = cos^2\theta" \left(\frac{\partial\theta}{\partial z}\right)^2 \tag{2.31}$$

and

$$(\hat{n} \cdot \vec{E}_{op})^2 = E_x^2 sin^2\theta + E_z^2 cos^2\theta" + 2E_xE_z sin\theta" cos\theta" \tag{2.32}$$

Then

$$F = F_d + F_{op} \tag{2.33}$$

$$= \frac{1}{2}\left(\frac{\partial\theta}{\partial z}\right)^2 (K_1 sin^2\theta" + K_3 cos^2\theta") - \frac{\varepsilon_\perp - \varepsilon_0}{8\pi}(E_x E_x^* + E_z E_z^*)$$

$$- \frac{1}{16\pi}\Delta\varepsilon(E_x^2 sin^2\theta + E_z^2 cos^2\theta" + 2E_x E_z sin\theta" cos\theta")$$

Where $\langle(\hat{n}\cdot\vec{E}_{op})^2\rangle = \frac{1}{2}(\hat{n}\cdot\vec{E}_{op})^2$, we get

$$(K_1 sin^2\theta" + K_3 cos^2\theta")\frac{d^2\theta}{dz^2} - (K_3 - K_1) sin\theta cos\theta \left(\frac{d\theta}{dz}\right)^2 \tag{2.34}$$

$$+ \frac{\Delta\varepsilon}{16\pi}\left[sin2\theta(|E_x|^2 - |E_y|^2) + cos2\theta(E_x E_z^* + E_x^* E_z)\right] = 0$$

Assume $\theta \ll 1$, which is usually the case. $sin2\theta \to 2\theta$, $cos2\theta \to 1$ $\left(\frac{d\theta}{dz}\right)^2 \to 0$, $sin^2\theta \to 0$, $cos^2\theta \to 1$

$$K_3\frac{d^2\theta}{dz^2} + \frac{\Delta\varepsilon}{16\pi}\left[2\theta(|E_x|^2 - |E_y|^2) + (E_x E_z^* + E_x^* E_z)\right] = 0 \tag{2.35}$$

From $\nabla\cdot\vec{D} = 0$, we get

$$E_z \cong -E_x(\frac{\Delta\varepsilon}{\varepsilon_\parallel})\theta \tag{2.36}$$

Eq. (2.35) Becomes

$$K_3\frac{d^2\theta}{dz^2} + \frac{\Delta\varepsilon}{8\pi}\frac{\varepsilon_\perp}{\varepsilon_\parallel}|E_x|^2\theta = 0 \tag{2.37}$$

The solution for this equation will be in the form of

$$\theta(z) = Asin\left[|E_x|\sqrt{\frac{\Delta\varepsilon}{2K_3}\frac{\varepsilon_\perp}{\varepsilon_\parallel}}z\right] + Bcos\left[|E_x|\sqrt{\frac{\Delta\varepsilon}{2K_3}\frac{\varepsilon_\perp}{\varepsilon_\parallel}}z\right] \tag{2.38}$$

Apply hard boundary condition $\theta(z=0) = 0$, we get B = 0; then for z = d, θ should come back to 0, which means that the following condition should be fulfilled to avoid the discontinuity.

$$|E_x|\sqrt{\frac{\Delta\varepsilon}{2K_3}\frac{\varepsilon_\perp}{\varepsilon_\parallel}}d \geq \pi \tag{2.39}$$

We also get the optical Freedericksz transition threshold field

$$|E_x| \geq \sqrt{\frac{2K_3}{\Delta\varepsilon}\frac{\varepsilon_\parallel}{\varepsilon_\perp}}\frac{\pi}{d} \tag{2.40}$$

To simplify the treatment of optical field-induced director axis reorientation and approximate the nonlinear coefficient, we can treat the equation as follows. The propagation vector incidents on the sample in a β angle with the direct axis of nematic liquid crystals. θ is the perturbed angle, also called reorientation angle. In this case only splay distortion is involved out of three elastic distortions of a nematic liquid crystal. A minimum free energy of the system can be expressed as:

$$K_1\frac{d^2\theta}{dz^2} + \frac{\Delta\varepsilon\langle E_{op}^2\rangle}{8\pi}sin2(\beta+\theta) = 0 \tag{2.41}$$

Assume θ is very small Eq. (2.41) can be rewritten as

$$2\xi^2\frac{d^2\theta}{dz^2} + (2\cos(2\beta))\theta + \sin(2\beta) = 0 \tag{2.42}$$

where $\xi^2 = 4\pi K_1/\Delta\varepsilon\langle E_{op}^2\rangle$

Although in Eq. (2.42) we have the assumption that the reorientation angle is very small, the small angle can give rise to sufficiently large refractive index change in this large birefringence of nematic liquid crystals. We apply the hard boundary condition and get the solution of Eq. (2.42)

$$\theta = \frac{1}{4\xi^2}sin2\beta(dz - z^2) \tag{2.43}$$

From the solved equation above, we can see when z = 0 or z = d, the θ is zero, which illustrates the hard boundary condition whereas θ reach the maximum when z = d/2. The reorientation profile can also be realized in Fig. 2.8.

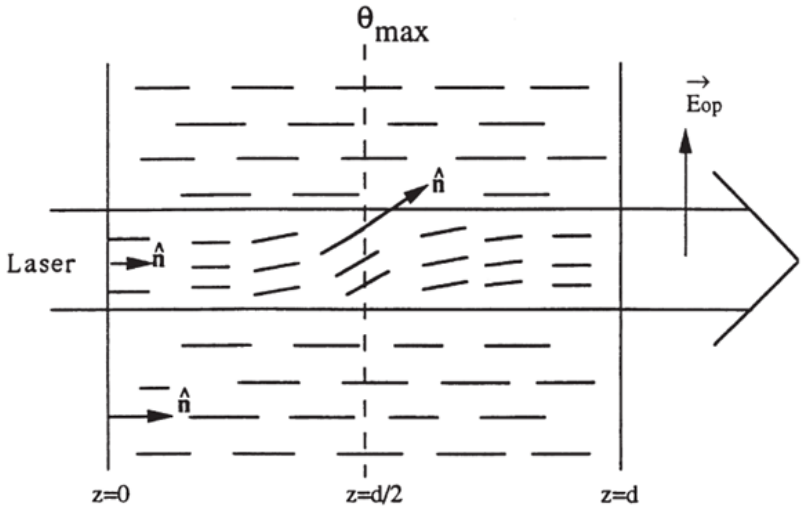

Fig. 2.8 Director axis reorientation profile with hard boundary condition in a nematic liquid crystal film

Thus we can express the refractive index change as a result of reorientation of direct axis as a function of z-direction.

$$\Delta n = n_e(\beta + \theta) - n_e(\beta) \tag{2.44}$$

Where the expression of $n_e(\beta + \theta)$ has been expressed in Eq. (2.3). Also, the refractive index change can be expressed as the multiple of nonlinear coefficient and intensity as bellows

$$\Delta n = \alpha_2(z)I \tag{2.45}$$

Therefore $\alpha_2(z)$ given by

$$\alpha_2(z) = \frac{(\Delta\varepsilon)^2 sin^2(2\beta)}{4K_1 c}(dz - z^2) \tag{2.46}$$

To have the average refractive index change over the sample thickness the factor $(dz - z^2)$ gives $d^2/6$. For a film, d = 100μm, $\Delta\varepsilon \sim 0.6$, $K_1 = 10^{-6}$, and $\beta = 45°$

$$\overline{\alpha_2} = 5 \times 10^{-3}\ cm^2/W \tag{2.47}$$

We know the nonlinear coefficient is related to the thickness, the birefringence, and the elastic constants of distortion according to the reorientation equation. For the case similar to single laser interaction, when a nematic liquid crystal thin film is crossed with two coherent laser beams, the sinusoidal intensity grating would form inside the liquid crystal layer. Molecules situated at the brighter intensity region will undergo reorientation while those in the darker region will stay relatively unperturbed. In addition, the space charge field will also occur and strengthen the modulation. This non-uniformly distributed liquid crystal molecule reorientation will incur the index grating and induce the beam diffraction as well.

The very early discovery and study of orientational photorefractivity in nematic liquid crystals was initiated by Rudenko and Sukhov [40], and later on Khoo [41] developed a more complete theory in 1994. After that, numerous studies on various aspects of orientational photorefractivity in liquid crystalline systems had been published, such as [42-44, 46].

CHAPTER 3 LASER INDUCED REFRACTIVE INDEX CHANGE

3.1 General Overview

Liquid Crystals whose physical properties such as temperature, density, molecular orientation, electronic structure etc., are easily perturbed by an applied optical field are defined as highly nonlinear materials. Most of these properties changes are followed by refractive index changes. Not only the physical properties but the properties of lasers can influence the amount of refractive index change such as polarization, intensity, beam size, and pulse width of the laser. Therefore, the interaction is quite complicated. Approximately, laser induced refractive index change mainly includes three effect, reorientation, thermal, density. Reorientation effect has been discussed in chapter 2. In this chapter I will explain thermal effect and density effect respectively. Most of the time, the effects are coupled when the laser interacts with the liquid crystals. For example, the thermal and density effects are coupled in electrostrictive equation. In the chapter, I will analyze the effects both in static and dynamic states since the response time is also a big issue in liquid crystal applications.

When the absorptance of liquid crystals or the intensity of laser increases, the induced thermal effect and density fluctuation through the temperature rise. Originally the transmission spectrum of nematic liquid crystal is shown as Fig. 3.1. Dips in curves describe the strong single photon absorption around 100-1000cm^{-1} while the absorption constant is quite low in spectrum except for dips areas. They are around 1-10cm^{-1}. Under intense laser illumination, two- or multi- photons absorption process will occur, as depicted as Fig. 3.2.

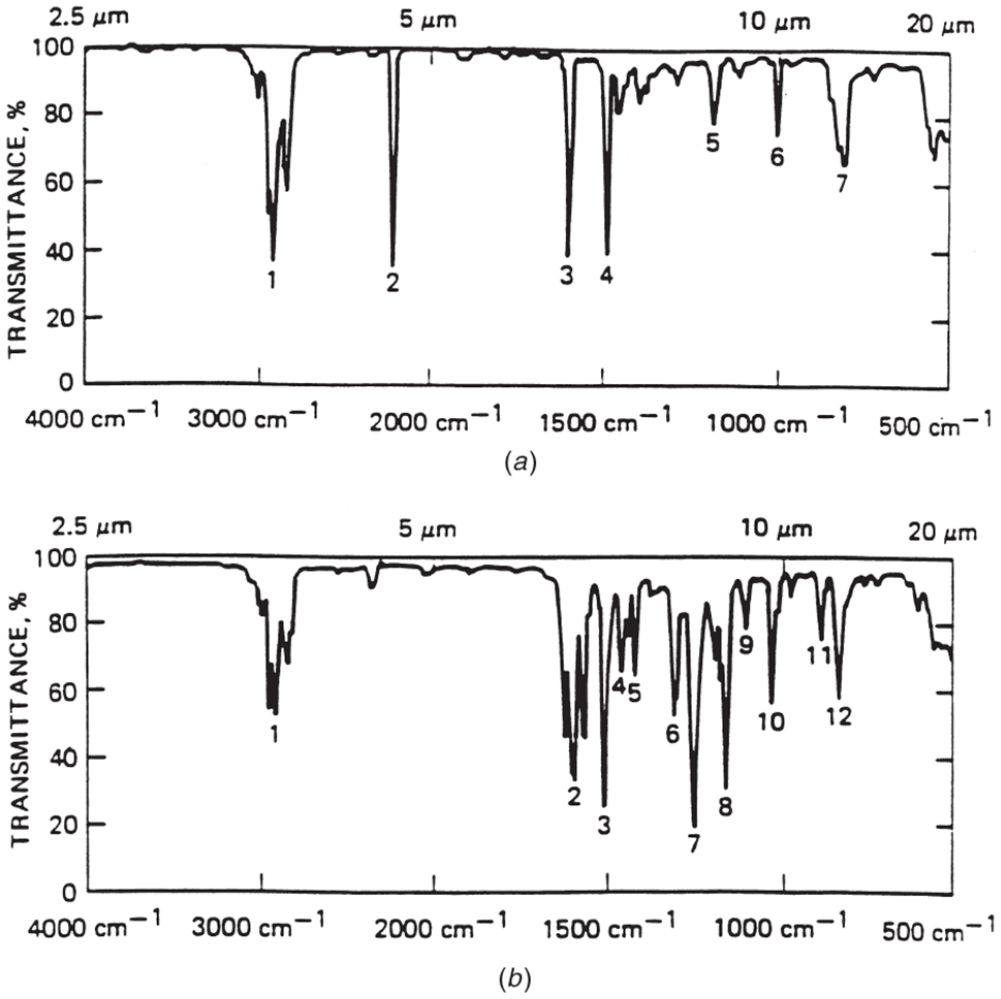

Fig. 3.1 Transmission Spectra of nematic liquid crystals: (a) 5CB and (b) MBBA [28]

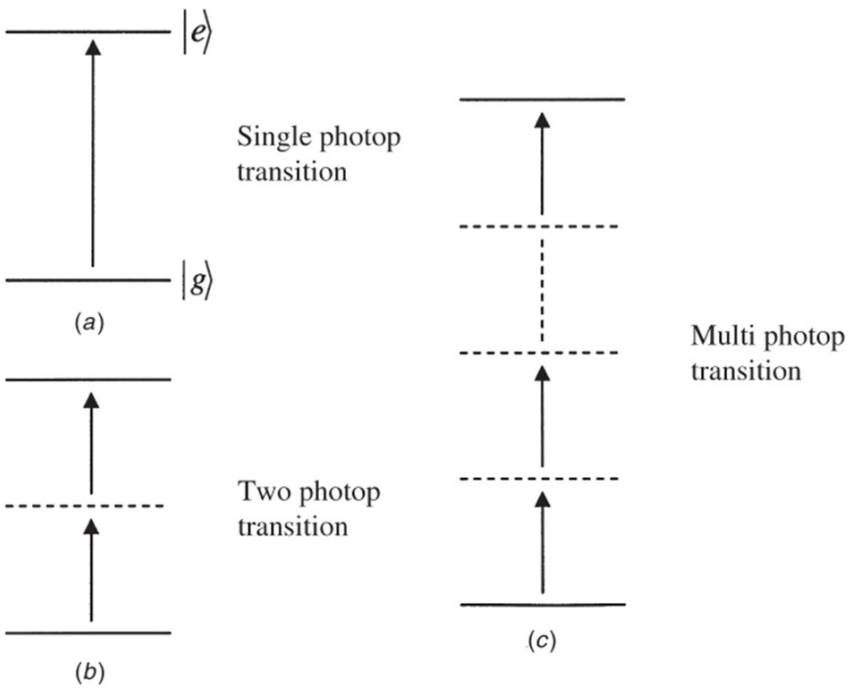

Fig. 3.2 (a) Single-photon absorption process (b) two-photon absorption process (c) multi-photon absorption process

3.2 Liquid-Cored Fiber Array Switching

Liquid-cored Fiber arrays are fabricated by the filling of the capillary arrays whose diameters are around 20μm with nonlinear liquid or liquid crystals. The refractive index of liquids (1.6) is usually larger than the capillary materials (1.5). This device is proven capable of high quality image transmission and self-action effects. The optical limiting action comes from the nonlinear cored liquids. Three main nonlinear mechanisms happen in this system, nonlinear guided-mode extinction, nonlinear absorption, and nonlinear scattering (density and thermal). In the lower incident laser energy regime, nonlinear absorptions predominate. At higher energies, nonlinear scattering, self-defocusing and bubble formation caused by thermal and density effects will play significant roles [52-55, 57].

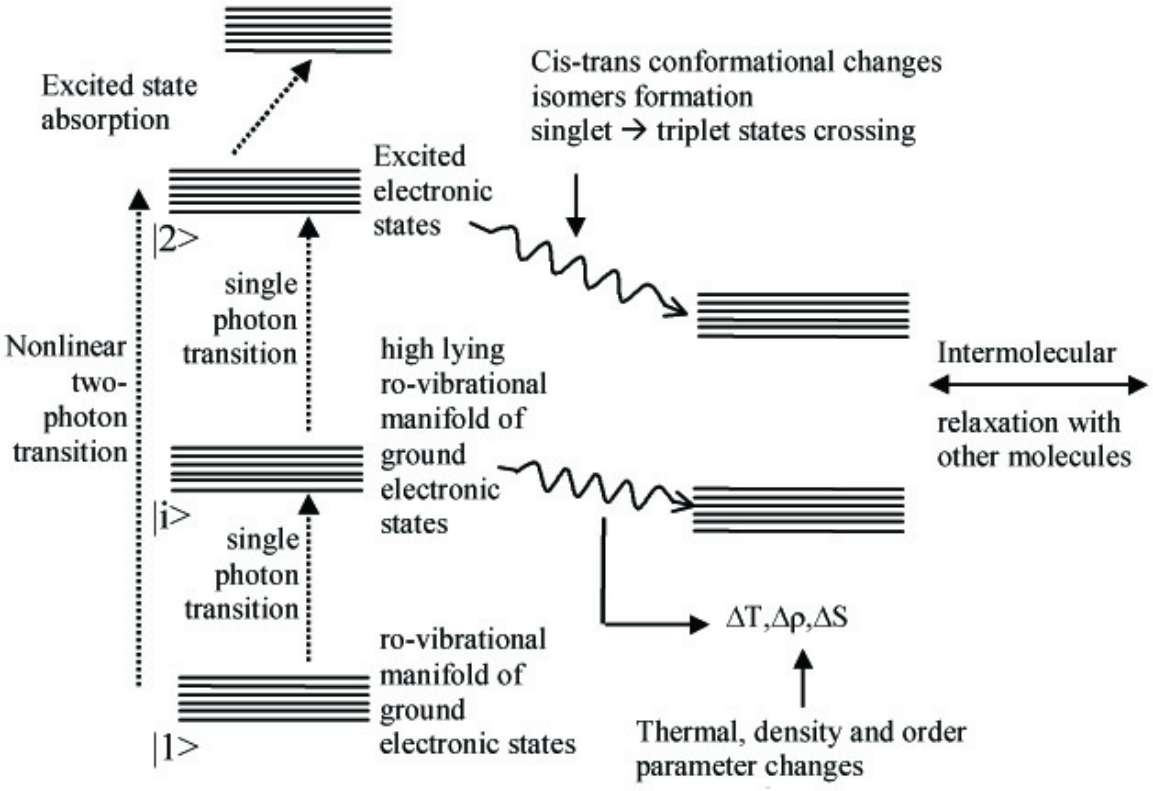

Fig. 3.3 Schematic depiction of two-photon, sequential intermediate state, and excited-state absorption processes, intersystem crossing, and other processes occurring in the core molecule [56]

The nonlinear liquid used in this fiber array system is L34, whose molecular structure and absorption spectrum are shown as Fig. 3.4. The experiment setup for optical limiting experiment is shown in the Fig. 3.5. Nanosecond and picosecond laser pulses used are expanded and spatially filtered to provide uniform-intensity 2-mm-diameter beams that are focused onto the fiber by a 10-mm focal-length lens. The input and output laser powers on the two ends of the fiber are simultaneously monitored.

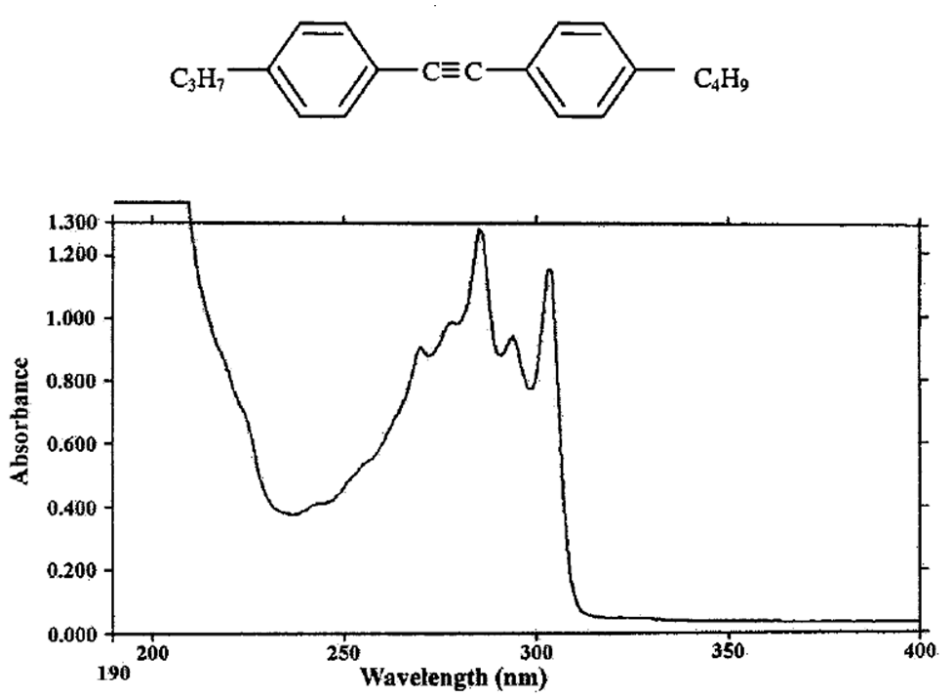

Fig. 3.4 Molecular structure and linear absorption spectrum of L34

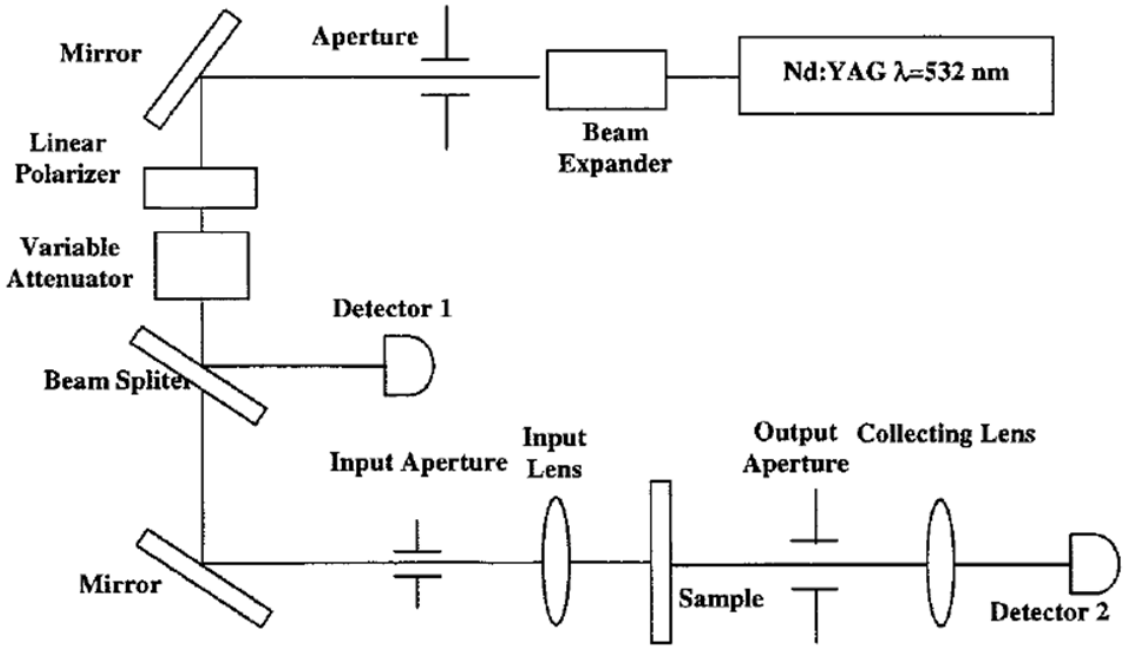

Fig. 3.5 The experimental setup for optical limiting measurement [56]

In the simulation from [56], only nonlinear absorption (TPA) is considered. In picosecond level, the experiment and the simulation match perfectly. However, in nanosecond level, for laser energy above 30μJ, the simulation and experiment curves diverge as Fig. 3.6. This disagreement arises because absorption-induced thermal and density effect is neglected. The effects can result in input coupling loss and propagation mode loss and wide angle scattering [57].

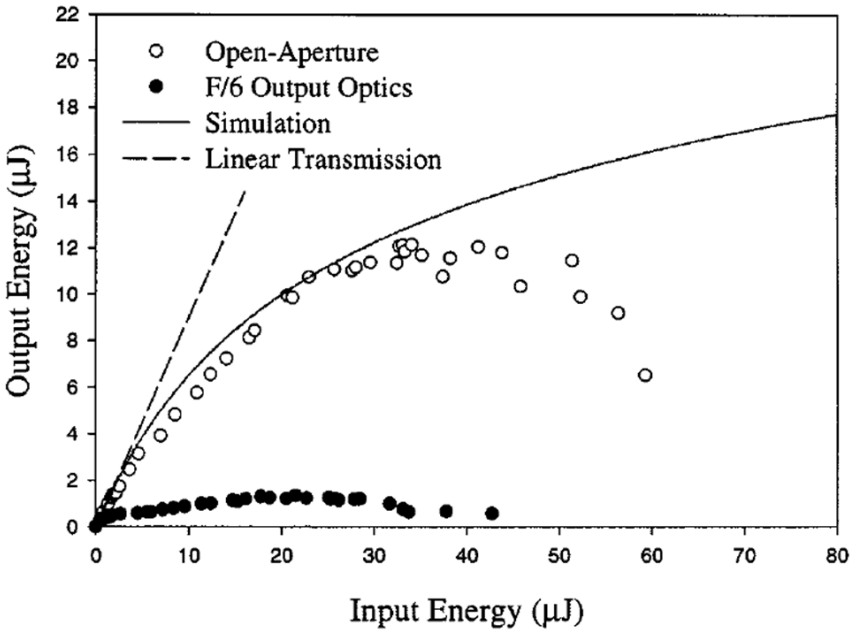

Fig. 3.6 Optical limiting results for nanosecond laser pulses (532nm; 20ns) using 5mm L34 cored clear-cladding fiber in F6 or open-aperture collection optics. Fiber core diameter: 20μm [56]

The liquid fiber array has been proven as a useful optical limiter against pulsed laser. In the nanosecond regime, laser induced thermal and density effects are major contributors to the optical limiting action. With these nonlinear mechanisms, and the light-blocking ability of the opaque cladding, the nonlinear liquid cored fiber array is found to be good protection device against picosecond–nanosecond and possibly microsecond laser pulses. In addition, the high induced thermal and density effects are our concerns. With longer laser pulses or even continuous wave, the thermal and density

effects dominate the nonlinear process, especially dye-doped enhanced thermal effect. In the next image processing topic, the refractive index change majorly comes from the laser induced thermal effect.

3.3 Laser Induced Temperature and Density Change

The inter- and intra- molecular relaxation processes following photon absorption are complicated. For the research about laser induced thermal and density changes in liquid crystals, the photon absorption plays a role transferring energy into liquid crystal molecules. The equation describing the rate of change of energy density is given by

$$\frac{\partial u}{\partial t} = \frac{nc\alpha E^2}{4\pi} + D\nabla^2 u - \frac{u}{\tau} \tag{3.1}$$

In this equation influencing the energy rate, the first term describes the absorption of the laser energy, while the second term describes the rate of energy diffusion also the third describes the thermalization relaxation process. In the thermal process, we assume that the diffusion process happens immediately which can be eliminated. Also, the energy transfers into a steady state very quickly so we can simplify Eq. (3.1) as

$$\frac{u}{\tau} = \frac{nc\alpha E^2}{4\pi} \tag{3.2}$$

From the hydrodynamic equation we can understand the whole process. Eq. (3.3) describes the photo-absorption and the following temperature rise and thermal relaxation process.

$$\rho_0 C_v \frac{\partial}{\partial t}(\Delta T) - \lambda_T \nabla^2(\Delta T) - \frac{(C_p - C_v)}{\beta_T}\frac{\partial}{\partial t}(\Delta\rho) = \frac{u}{\tau} = \frac{nc\alpha E^2}{4\pi} \tag{3.3}$$

Eq. (3.4) describes the thermal expansion and the electrostrictive effect on the density change

$$-\frac{\partial^2}{\partial t^2}(\Delta\rho) + v^2\nabla^2(\Delta\rho) + v^2\beta_T\rho_0\nabla^2(\Delta T) + \frac{\eta}{\rho_0}\frac{\partial}{\partial t}\nabla^2(\Delta\rho) = \frac{\gamma^e}{8\pi}\nabla^2(E^2) \tag{3.4}$$

Where ρ_0 is the unperturbed density of liquid crystal, C_p and C_v are the specific heats, λ_T is the thermal conductivity, η is the viscosity, v is the speed of sound, γ^e is the electrostrictive coefficient [$\gamma^e = \rho_0(\partial\varepsilon/\partial\rho)_T$], β_T is the coefficient of volume expansion [58, 59].

With these two coupled equations we understand the relationship between thermal and density effect and optical field. For these complicated couples differential equations, we introduce a diffraction system to realize the thermal and density effect. First, the total refractive index change majorly comes from two effect, thermal and density effect, as below

$$\Delta \mathrm{n} = \Delta n_T + \Delta n_\rho \tag{3.5}$$

Also these two effects can be represented as follows respectively

$$\Delta n_T = \frac{\partial n}{\partial T} T(t) \tag{3.6}$$

$$\Delta n_\rho = \frac{\partial n}{\partial \rho} \rho(t) = \frac{\partial n}{\partial \rho} (\rho^e + \rho^T) \tag{3.7}$$

We use a sinusoidal optical intensity to simplify the complicated coupled equations and to gain insight into the system. Fig. 3.7 shows the setup for probing the dynamics of laser induced transient refractive index change in liquid crystals. A spatially induced periodic refractive index change is expected, and we can realize the mechanism by measuring the diffraction efficiency, which is defined by the ratio of the diffraction intensity to the zero-order laser intensity as below.

$$\eta \approx J_1^2 \left(\frac{\pi \Delta n d}{\lambda}\right) \tag{3.8}$$

Assume $\frac{\pi \Delta n d}{\lambda} \ll 1$ when the refractive index change is small. Eq. (3.8) can be simplified as Eq. (3.9)

$$\eta = \left(\frac{\pi \Delta n d}{\lambda}\right)^2 \tag{3.9}$$

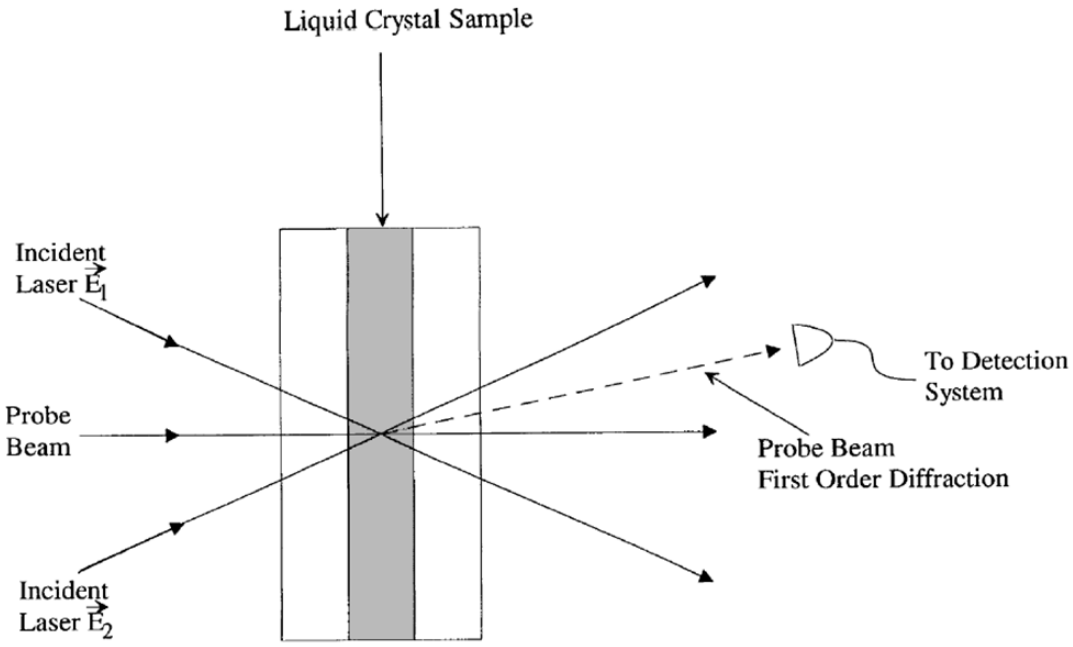

Fig. 3.7 Experimental setup for probing the dynamics of laser-induced transient refractive index changes in liquid crystals

The optical intensity profile inside the liquid crystals can be expressed as the interference form of two laser beams

$$E^2 = E_1^2 + E_2^2 + 2|E_1 E_2| cos[(k_1 - k_2) \cdot r] \tag{3.10}$$

The first two terms in the right side are DC part, which is not a function of spatial position. They do not contribute to the diffraction distribution. Therefore, we only consider the periodic term as the effect source. Assume $E_1 = E_2 = E_0$ and $k_1 - k_2 = q$. Then we get

$$E^2 = 2E_0^2(1 + \cos(q \cdot y)) \tag{3.11}$$

Corresponding, $\Delta\rho$ and ΔT are of the same form

$$\Delta\rho = \rho(t) cos(q \cdot y) \tag{3.12}$$

$$\Delta T = T(t) cos(q \cdot y) \tag{3.13}$$

Where $\rho(t)$ and $T(t)$ are the density and temperature grating amplitude. Substitute Eq. (3.12) and (3.13) into Eq. (3.3) and (3.4) and give the initial condition $\rho(0) = T(0) = 0$. Ignore the $\Delta\rho$ term in Eq. (3.3) we can solve $\rho(t)$ and $T(t)$ analytically.

For $0 < t < \tau_p$, where τ_p is the duration of the laser beam

$$T(t) = \left(\frac{\alpha c n E_0^2}{4\pi\rho_0 C_v \Gamma_R}\right)[1 - \exp(-\Gamma_R t)] \tag{3.14}$$

$$\rho(t) = \rho^e(t) + \rho^T(t) \tag{3.15}$$

$$= \left(\frac{\gamma^e E_0^2}{4\pi v^2}\right)[1 - \exp(-\Gamma_B t)\, cos\Omega t] - \left(\frac{\beta_T \alpha c n E_0^2}{4\pi C_v \Gamma_R}\right)[1 - \exp(-\Gamma_R t)]$$

Where the thermal decay constant Γ_R is given by

$$\Gamma_R = \tau_R^{-1} = \frac{\lambda_T q^2}{\rho C_v} \tag{3.16}$$

The Brillouin decay constant is given by

$$\Gamma_B = \Gamma_B^{-1} = \frac{\eta q^2}{2\rho_0} \tag{3.17}$$

The sound frequency Ω is given by

$$\Omega = \sqrt{q^2 v^2 - \Gamma_B^2} \tag{3.18}$$

Using the typical parameters, $n = 1.5$, $\eta = 7 \times 10^{-2} kg \cdot m^{-1} \cdot s^{-1}$, $v = 1540 m \cdot s^{-1}$, $\rho_0 = 10^3 kg \cdot m^{-3}$, and $\frac{\lambda_T}{\rho_0 C_v} = 0.79 \times 10^{-7} m^2 \cdot s^{-1}$. By assuming the grating constant Λ is 20μm, we have the estimated values $\tau_R \approx 100\mu s$ and $\tau_B \approx 200 ns$. From Eq. (3.15), the density grating amplitude comes majorly from two effects. One is electrostrictive effect $\rho^e(t)$, which is proportional to γ^e and characterized by the Γ_B and Ω. The other effect $\rho^T(t)$ comes from thermoelastic contribution, which is characterized by Γ_R. From the simple diffraction setup, we gain the insight about laser induced thermal

and density effects, including the time scales, the type of effects, propagation or nonpropagation, and the corresponding parameter.

3.4 Temperature and Order Parameter Dependence of Refractive Indices

The thermal index ∂n/∂T rises from two parts. One is the rising temperature of the molecule, resulting in spectrum shift. The other is the temperature dependent order parameters change. In ordered liquid crystals the second effect contributes most of the thermal induced refractive index change. So we can express the thermal gradient as

$$\frac{\partial n}{\partial T} = \frac{\partial n}{\partial S}\frac{\partial S}{\partial T} + \frac{\partial n}{\partial \rho}\frac{\partial \rho}{\partial T} \tag{3.19}$$

For different laser polarization, the thermal index gradient is different. The laser whose polarization is parallel to the nematic director axis induces the extraordinary thermal index gradient as Eq. (3.20). The one whose polarization is perpendicular to the nematic director axis induces the ordinary thermal index gradient as Eq. (3.21). Following the standard nematic theory, we can write optical dielectric constants $\varepsilon_{\parallel}$ and $\varepsilon_{\perp}$ as

$$\varepsilon_{\parallel} = \varepsilon_l + \frac{2}{3}\Delta\varepsilon \tag{3.20}$$

$$\varepsilon_{\perp} = \varepsilon_l - \frac{1}{3}\Delta\varepsilon \tag{3.21}$$

Where ε_l is the dielectric constant associated with the nematic when order parameter is zero and the dielectric anisotropy $\Delta\varepsilon = \varepsilon_{\parallel} - \varepsilon_{\perp}$

$$\Delta\varepsilon = \frac{N_A\rho}{\varepsilon_0 M}(\alpha_l K_l - \alpha_t K_t)S \tag{3.22}$$

$$\varepsilon_l = 1 + \frac{N_A\rho}{3\varepsilon_0 M}(\alpha_l K_l + 2\alpha_t K_t) \tag{3.23}$$

Where N_A is Avogadro's number, ρ is the density, S is the order parameter, M is the mass number, $\alpha_{l,t}$ are the longitudinal and transverse components of the electronic polarization tensor, and $K_{l,t}$ are the longitudinal and transverse components of the local field factor. Based on Eq. (3.11) and (3.12), we can simplify them as following [60, 61]:

$$\varepsilon_l \sim 1 + C_1\rho \tag{3.24}$$

$$\Delta\varepsilon \sim C_2\rho S \tag{3.25}$$

Where C_1 and C_2 are deducible constants. The order parameter in most nematic materials can be approximated by the expression.

$$S = (1 - 0.98\frac{TV^2}{T_{Ni}V_{Ni}^2})^{0.22} \tag{3.26}$$

Where T_{Ni} is the phase transition temperature from nematic to isotropic and V_{Ni} is the corresponding molar volumes in phase transition. We can obtain the thermal index gradients from [28. Ch3 13]as follows.

$$\frac{dn_{\parallel}}{dT} = \frac{1}{n_{\parallel}}\left(C_1\frac{d\rho}{dT} + \frac{2}{3}C_2 S\frac{d\rho}{dT} + \frac{2}{3}C_2\rho\frac{dS}{dT}\right) \tag{3.15}$$

$$\frac{dn_{\perp}}{dT} = \frac{1}{n_{\perp}}\left(C_1\frac{d\rho}{dT} - \frac{1}{3}C_2 S\frac{d\rho}{dT} - \frac{1}{3}C_2\rho\frac{dS}{dT}\right) \tag{3.16}$$

From known value of $\rho \sim 1\ gm\cdot cm^{-3}$, $C_1 \sim 1.33$, $C_2 \sim 1.12$, we get

$$\frac{dn_{\parallel}}{dT} = \frac{1}{n_{\parallel}}\left((1.33 + 0.74S)\frac{d\rho}{dT} + 0.74\frac{dS}{dT}\right) \tag{3.17}$$

$$\frac{dn_{\perp}}{dT} = \frac{1}{n_{\perp}}\left((1.33 - 0.37S)\frac{d\rho}{dT} - 0.37\frac{dS}{dT}\right) \tag{3.18}$$

Consider PCB (pentyl-cyano-biphenyl) at 20°C and 35°C, the measured $\frac{d\rho}{dT} \sim 6\times10^{-4} gm\cdot cm^{-3}\cdot K^{-1}$ [61]. The temperature dependent gradients become one order larger near the phase transition temperature, depicted as Fig. 3.8.

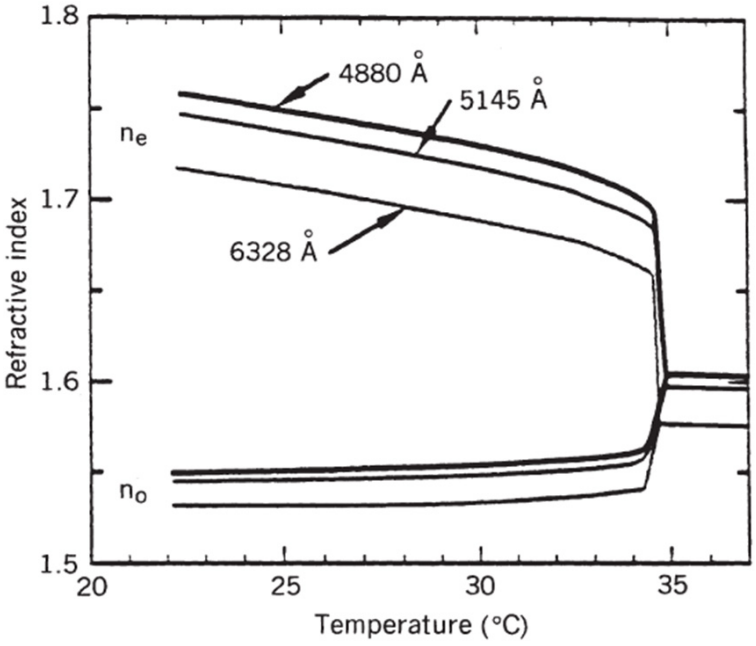

Fig. 3.8 Temperature dependence of refractive indices of 5CB
in the visible spectrum [28]

So far we just discuss the relationship between the refractive index change and the temperature. In our passive optical system, the overall relationship is between the laser intensity and the refractive index change. We will discuss the absorption of laser power and transfer the energy into heat but not consider about the density change. We have the simplified equation as follows.

$$T(t) = \left(\frac{\alpha c n E_0^2}{4\pi\rho_0 C_v \Gamma_R}\right)[1 - \exp(-\Gamma_R t)] \tag{3.19}$$

In the preceding equation the thermal decay constant Γ_R

$$\Gamma_R = \tau_R^{-1} = \frac{\lambda_T q^2}{\rho_0 C_v} \tag{3.20}$$

When $t \gg \tau_R$

We can have the steady state thermal nonlinearity of nematic liquid crystals

$$\Delta n_T = \alpha_2^{ss}(T) I_{op} = \left(\frac{\alpha c n E_0^2}{4\pi \rho_0 C_v \Gamma_R}\right) \frac{\partial n}{\partial T} \tag{3.21}$$

$$\alpha_2^{ss}(T) = \left(\frac{\alpha}{\rho_0 C_v \Gamma_R}\right) \frac{dn}{dT} \tag{3.22}$$

The temperature dependent nonlinearity coefficient is presented as above. The relationship between refractive index and temperature was discussed in Eq. (3.15) and Eq. (3.16). Therefore from this equation we know the absorption play a key role in this nonlinearity. In nematic liquid crystals (5CB), the transparency is good in visible and near infrared regime. When the laser power increases up to a very high level, we can see the nonlinear effect. However, if the laser power is small, we still can dope some dyes to increase the absorption. The dye-doped liquid crystals lift nonlinear effect obviously, and are widely investigated worldwide.

In pure liquid crystals, the absorption is related to the electronic properties of molecules in liquid crystals. The energy level of aromatic rings dominates where the wavelength is. The photon absorption gives rise to ultraviolet or infrared range. In order to increase the nonlinearity in the visible or near infrared, dyes are a good candidate.

The measured intensity of transmitted through a layer of material with thickness is related to the incident intensity according to the inverse exponential power law that is usually referred to as Beer–Lambert law:

$$I = I_0 e^{-\alpha l} \tag{3.23}$$

where l denotes the path length. α is the attenuation coefficient (or linear attenuation coefficient). The simple absorption equation can be referred in dye doped liquid crystals.

3.5 The Mechanism of Thermal Diffraction in Nematic Liquid Crystals

According to earlier experiment setup, reported by Khoo and Normandin [61], depicted as Fig. 3.9, the detailed analysis of thermal grating diffraction in nematic liquid crystals is presented, especially the transient response. In the degenerated four-wave

mixing configuration, two lasers intersecting on the nematic liquid crystal film at a wave mixing angle θ. The planar aligned sample is used here, and based on polarizations, the two incident lasers are divided into two cases: one is parallel to the director axis; the other is perpendicular to the director axis. The wave mixing angles is form 1° to 12° and the corresponding grating constant is from 34μm to 5μm. The wave vector $\vec{q}$ ($\vec{q} = \overrightarrow{k_1} - \overrightarrow{k_2}$) is not exactly normal or parallel to the director axis of liquid crystals. However, we can neglect the correction factor and assume in a perfect situation since the wave mixing angle is small. The static behavior works like the content discussed in chapter 3.2

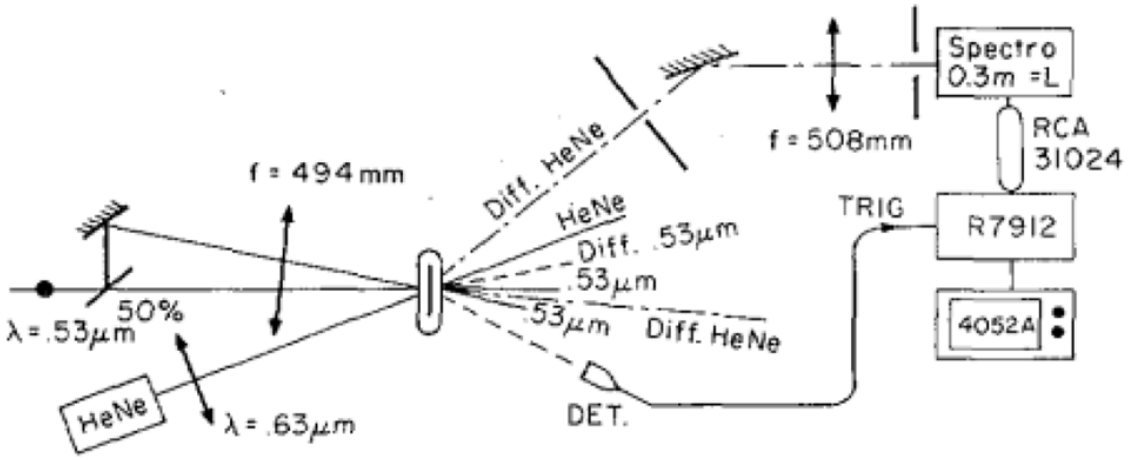

Fig. 3.9 Schematics of diffraction setup [61]

Fig. 3.10 show the experimental results of $dn_{\parallel}/dt$ and $dn_{\perp}/dt$. The value of $dn_{\parallel}/dt$ is generally 5-7 times larger than that of $dn_{\perp}/dt$ when the temperature is far away from the clearing point. Nevertheless, when the temperature increases, two thermal indices dramatically rise, not in a linear relationship. The detail of diffraction efficiency was also discussed in this paper [61]. Without consideration of the losses in the liquid crystals from scattering and reflection losses from the glass slides, and the laser pulse profile, the maximum diffraction efficiency of the experiment result is one order smaller than the theoretically estimated one. In addition, that the thicker sample has higher thermal index change and higher diffraction efficiency has been proven in this article.

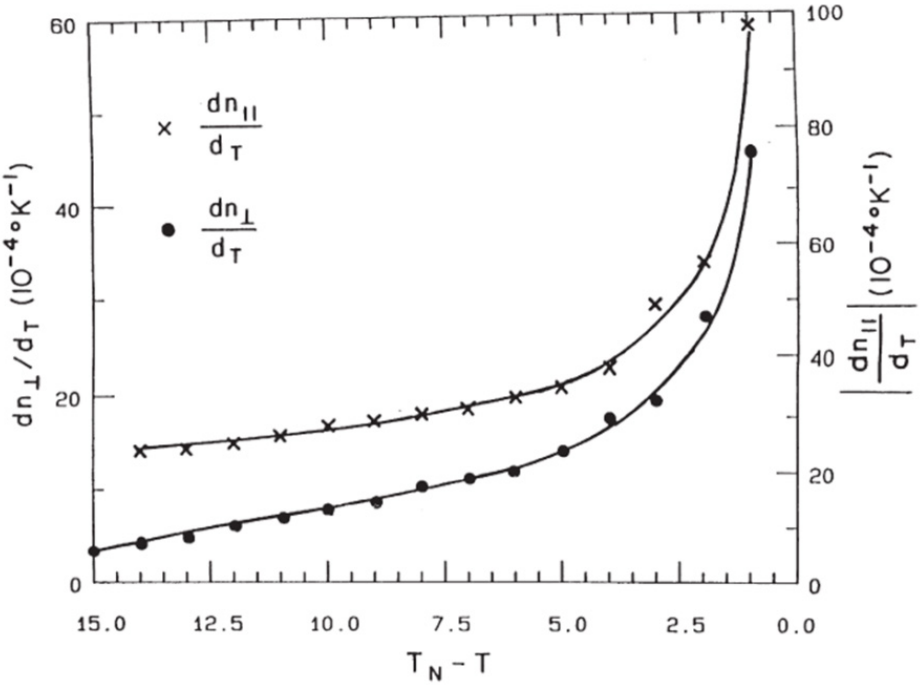

Fig. 3.10 Plot of $dn_{\parallel}/dt$ and $dn_{\perp}/dt$ for the liquid crystal for temperature near clearing point [61]

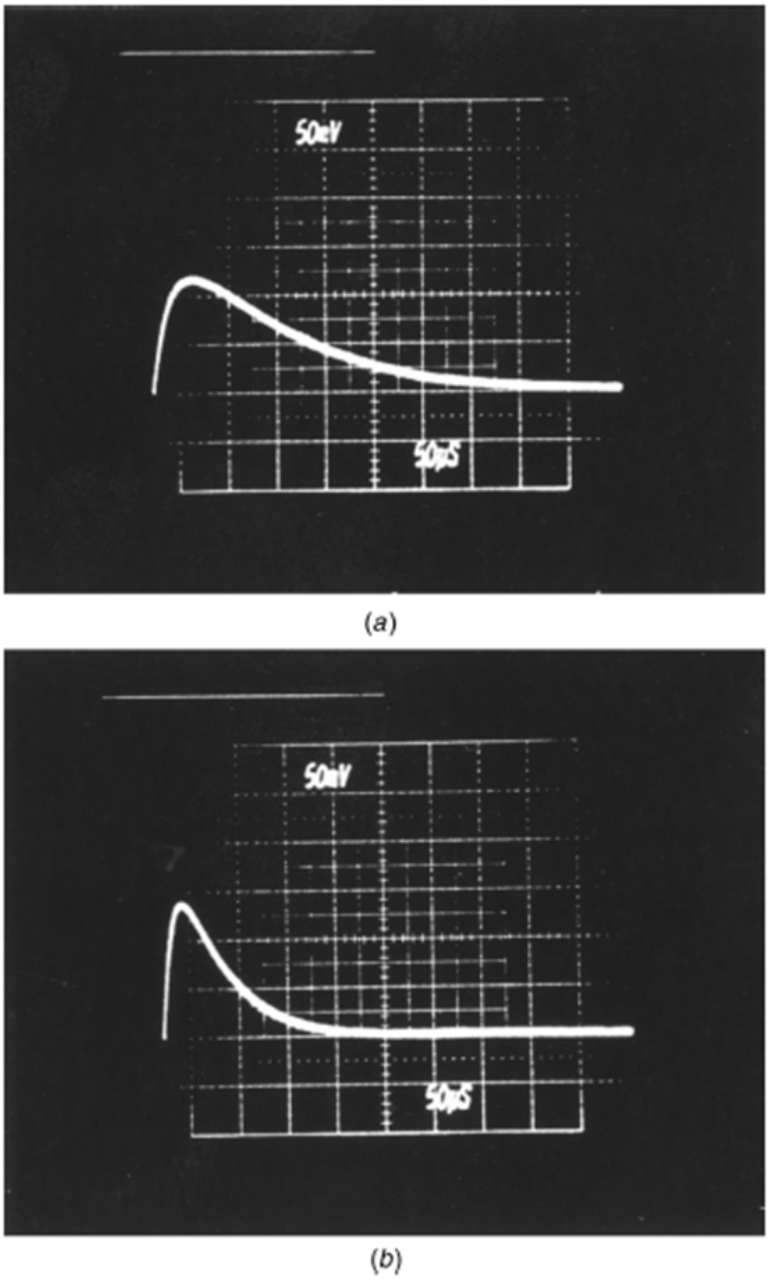

Fig. 3.11 Oscilloscope traces of the relaxation dynamics of the first order probe beam diffraction from the thermal gratings [61]

The most important part is to understand the dynamic response of thermal effect. The diffraction decay behavior is depicted as Fig. 3.11. There are two cases. In Fig. 3.11 (a), $\vec{q}$ is normal to the director axis, whereas in Fig. 3.11 (b), $\vec{q}$ is parallel to the director

axis. From the oscilloscope trace, $\tau_{\perp}$ is around 100μs whereas$\tau_{\parallel}$ is around 50μs. From the theoretic point of view, assume the wave mixing angle is 2°, the grating constant is 17μm, and the sample thickness is 40μm, so the thermal diffusion time constants along the $\vec{q}$ direction in 1-dimension case can be expressed as

$$\tau_{\parallel} = \frac{1}{D_{\parallel} q_{\parallel}^2} \tag{3.24}$$

$$\tau_{\perp} = \frac{1}{D_{\perp} q_{\perp}^2} \tag{3.25}$$

Where

$$q_{\parallel} = \frac{2\pi}{\Lambda_{\parallel}} \tag{3.26}$$

$$q_{\perp} = \frac{2\pi}{\Lambda_{\perp}} \tag{3.27}$$

Where the grating constants $\Lambda_{\perp}$ and $\Lambda_{\parallel}$ is 17μm and 15μm, respectively. Some parameters can be referred to Table 3.1. We can get the theoretic estimates of $\tau_{\perp}$ and $\tau_{\parallel}$, 55μs and 110μs respectively, showing a good agreement with the experiment results.

Table 3.1 Typical values for nematic liquid crystals [28]

Parameter	Value	Nematic
Absorption constant		
(α in cm^{-1})	<1, visible	E7
	23, near infrared	E7
	$40 \sim 100$, infrared	E7
	69, infrared	5CB
	44, infrared	E46 (EM Chemicals)
Diffusion constant		
$D = \lambda_T/\rho_0 C_v$	$D_{\parallel} = 1.95 \times 10^{-3}\,cm^2/s$	E7
	$D_{\perp} = 1.2 \times 10^{-3}\,cm^2/s$	E7
Thermal index gradients		
$dn_{\perp}/dT$	10^{-3} K	5CB at 25 °C
	10^{-2} K (visible-infrared)	5CB near T_C
$Dn_{\parallel}/d_T$	-2×10^{-3} K	5CB at 25 °C
	-10^{-2} K (visible-infrared)	5CB near T_C

Visible → 0.5 μm; near infrared → CO wavelength ≈ 5 μm; infrared → 10 μm.

This study also shows that there is almost no difference between the pure nematic liquid crystals and dye-doped ones concerning the rise and decay time constants of wave-mixing diffraction. We can conclude that the dye molecules used essentially act as absorbers and immediately transfer the excitation to the nematic via intermolecular relaxation processes.

3.6 Dynamic Simulation of Density Effect in Nematic Liquid Crystals

For the pure liquid crystals, under the laser duration of 300ns, the inter-molecule absorption with a response time of picoseconds to nanoseconds have reached a steady state, and the reorientational effects with response time of several milliseconds can be neglected. In this case, the involved effect in the limiting results mainly comes from density effect. The density change under short input pulse has been simulated. The

thermodynamic equations describing the coupled density and temperature change, $\Delta\rho$ and ΔT respectively, under electric field input are as Eq. (3.3) and Eq. (3.4) [58].

When the time period for temperature change is more than 100 times smaller than the duration of input electric field, the density related equation can be simplified to:

$$-\frac{\partial^2}{\partial t^2}(\Delta\rho) + v^2\nabla^2(\Delta\rho) + \frac{\eta}{\rho_0}\frac{\partial}{\partial t}\nabla^2(\Delta\rho) = \frac{\gamma^e}{8\pi}\nabla^2(E^2) \tag{3.28}$$

In which η is the viscosity, ρ_0 is the unperturbed density, and v is the sound velocity. The electric field amplitude of optic wave is set around 6000V/m. Gaussian distributions are used in both the temporal and spatial domain, in the form of

$$E^2 = E_0^2 e^{-\frac{(r-r_0)^2}{2w^2}} e^{-\frac{(t-t_0)^2}{2\tau_p^2}} \tag{3.29}$$

in the polar coordinate.

The equation can be understood as a wave equation with coupled feedback and an outside field. Therefore the form of the solution can be foreseen as a kind of propagating wave. The finite difference method seems to be the simplest approach for the numerical solution for PDEs since the analytic solution is hard to solve [69]. Finite element method was developed in the 1960s and 70s while it is difficult to quote the originality. At the beginning, engineers used the method to solve problems in complex elasticity and structure analysis, fluid flow, heat transfer, and other areas. Around 1970s, the finite element method was widely applied in various engineering problems.

The Fig. 3.12 demonstrates the computation procedure. Index r and t represent the step index in space and time.

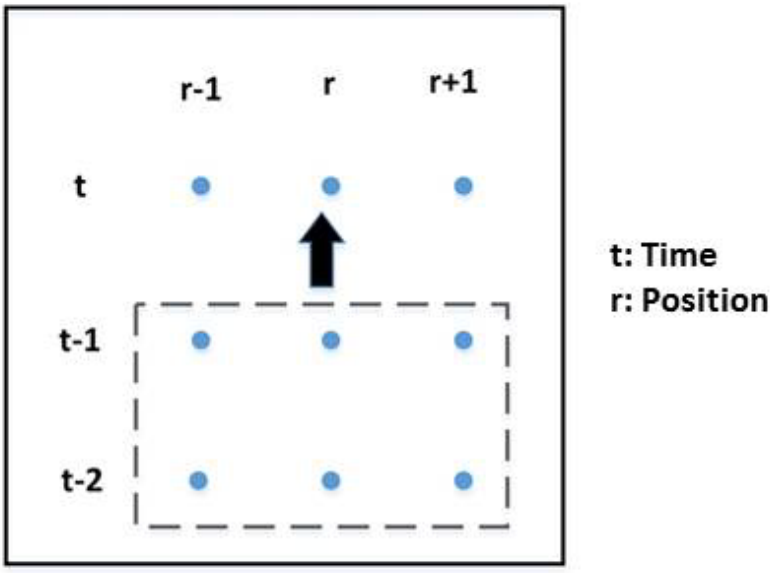

Fig. 3.12 Finite difference method stencils for 1-D implicit method

Based on Eq. (3.4), we study the density effect, ignoring the thermal effect here. The equation becomes second order partial differential equation. With the finite element method, we try to simplify the density change related to time and one-dimension position, ignoring the thickness and assuming the symmetric in the incident plane [70]. The three terms in Eq. (3.28) can be expressed as finite element method form as below:

$$\frac{\partial^2}{\partial t^2}(\Delta\rho) = \frac{\rho_r^{t+2} - 2\rho_r^{t+1} + \rho_r^t}{\Delta t^2} \tag{3.30}$$

$$\nabla^2(\Delta\rho) = \frac{\rho_{r+1}^{t+1} - 2\rho_r^{t+1} + \rho_{r-1}^{t+1}}{\Delta x^2} \tag{3.31}$$

$$\frac{\partial}{\partial t}\nabla^2(\Delta\rho) = \frac{\rho_{r+1}^{t+1} - 2\rho_r^{t+1} + \rho_{r-1}^{t+1} - \rho_{r+1}^{t} + 2\rho_r^{t} - \rho_{r-1}^{t}}{\Delta x^2 \Delta t} \tag{3.32}$$

In Fig. 3.12, we explain a point based on the six time-space related points. According to the equations, we set the generated Gaussian electric field far from edges in both time and space. Meanwhile assume the density change is zero at t = 0 and two spatial ends. It is reasonable to have the two assumptions because the perturbation cannot

propagate in a long distance since there is viscosity and electrostrictive coefficient in the equation. The parameters we used in the simulation is listed as:

Table 3.2 Parameters in simulation

$\eta = 7 \times 10^{-2}\ \mathrm{kg \cdot m^{-1} \cdot s^{-1}}$
$\nu = 1540\ \mathrm{m \cdot s^{-1}}$
$\rho_0 = 10^3\ \mathrm{kg \cdot m^{-3}}$
$\gamma^e = 0.02\ \mathrm{F \cdot m^{-1}}$
$E_0 = 6000\ \mathrm{V \cdot m^{-1}}$

The numerical solution is illustrated as Fig. 3.13. The laser beam size in this condition is 5μm, and pulse width is 2ns. The single cell in time domain is 0.02ns while the cell in space domain is 0.2μm. From Fig. 3.13, the density change effect comes following the laser field. The peak-peak span is defined as the response time of density fluctuation. When the pulse width is 2ns, the density change response time is around 3ns, which is reasonable with the theories. Meanwhile the density fluctuation can reach 0.015. In addition, we change the laser field in different levels, 2000$V \cdot m^{-1}$, 6000 $V \cdot m^{-1}$, 12000 $V \cdot m^{-1}$, and 20000 $V \cdot m^{-1}$. The response time keeps the same as intensity – independent around 3ns. In Fig. 3.14, we show the simulation result of response time of density fluctuation with different input pulse width which is 5ns, 20ns, and 100ns, respectively. The peak-to-peak time keeps the same around 3ns. Compared to Brillouin decay constant around 200ns, describing the propagation decay time after the interaction between the field and liquid crystals, the fluctuation response accounts for the immediate fluctuation time. The combination of these two constants can explain the real density reaction dynamically.

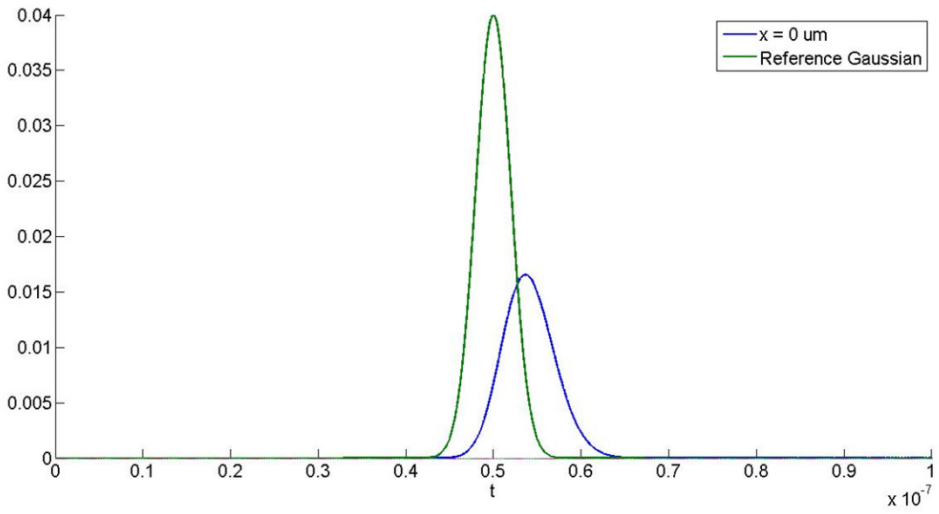

Fig. 3.13 Dynamic density fluctuation response

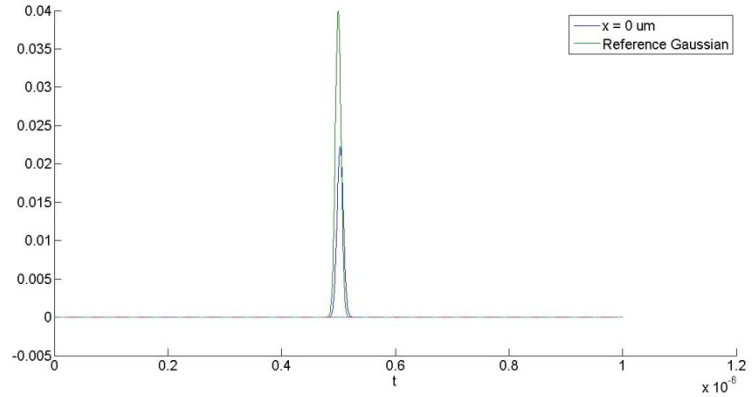

(a)

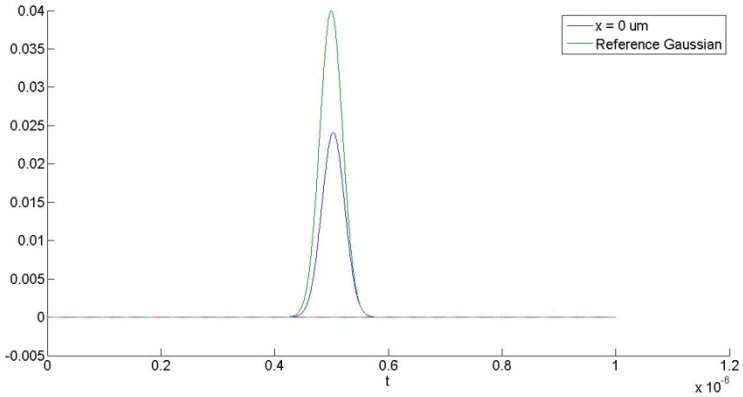

(b)

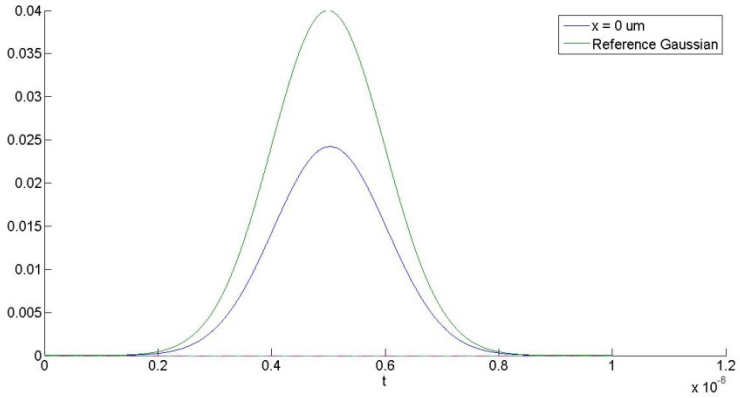

(c)

Fig. 3.14 Dynamic response time in three different pulse widths : (a) 5ns (b) 20ns (c) 100ns

Besides the simulation, the experiment results about the dynamic response of the TNLC sample experiencing a 300ns laser pulse are shown in Fig. 3.15. It is observed that the limiting threshold is 2.08mJ. The limiting curves under different input energies are also plotted. The starting points of the limiting action keep almost same for three different input energies, which is different from the doped situations.

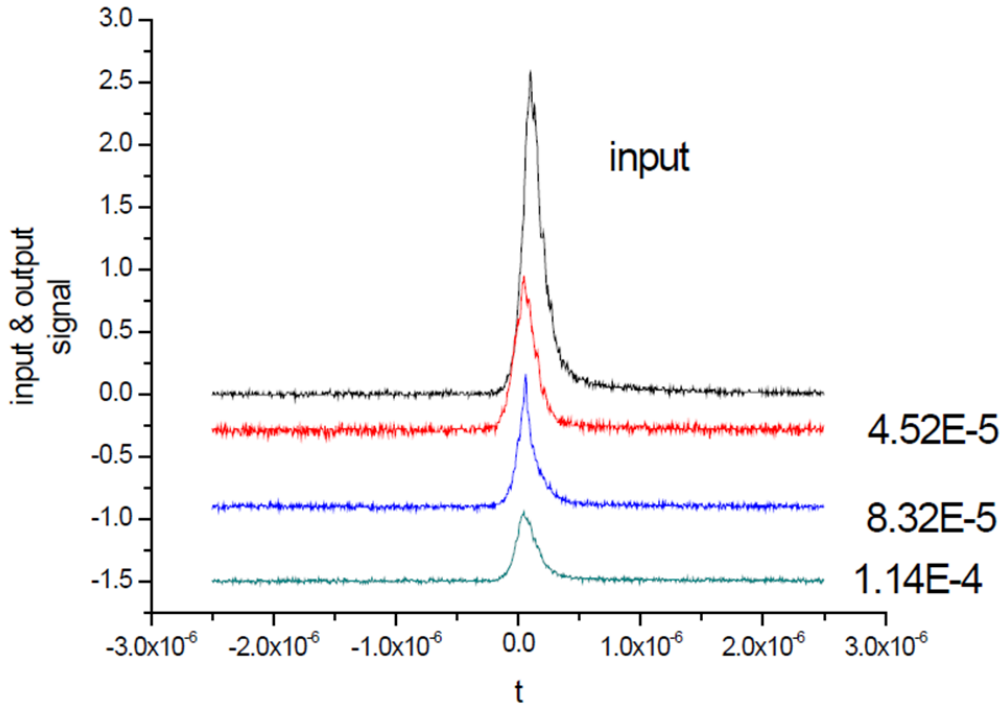

Fig. 3.15 Oscilloscope plots of undoped TNLC optical limiting
input and output signal : multiple inputs with different powers

We use a large pulse width (20ns) to observe the density fluctuation propagation from 0μm (center point) to 200μm. Due to the viscosity, the density fluctuation profile is similar to the Gaussian beam in the center point where the laser impinges on. In the surrounding area, the fluctuation is not so high, and the profile is different. Because of the conservation in the volume, when the density changes positively in some area, the density changes negatively in somewhere else. The curve, 30μm from the center in Fig. 3.16 gives a good illustration. The profile of density fluctuation first decreases and increases

again, proven as a propagation wave. However, when the density fluctuation travels to a long distance, the fluctuation profile will decay to zero finally.

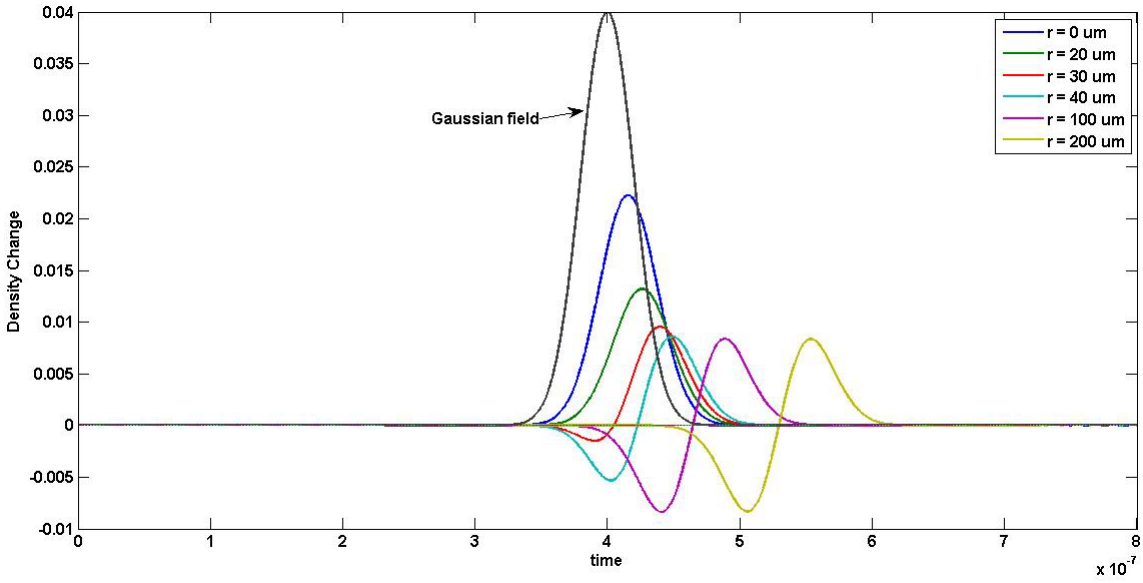

Fig. 3.16 Density fluctuation in different position

There are many parameters influencing the density fluctuation, such as laser intensity and viscosity. We especially simulate the density change in different viscosity since different liquid crystals have different viscosities. In Fig. 3.17, with the same parameters as previous simulation (ω = 5μm; τ = 2ns). The observed points, 0, 20μm, and 100μm from the center of the input beam are added. In Fig. 3.17(a), the viscosity is the same (0.07 $kg \cdot m^{-1} \cdot s^{-1}$). In Fig. 3.17(b), the viscosity increase ten times of original value while Fig. 3.17(c) shows the twenty times. The viscosity does change the fluctuation profile. When the viscosity increases, the density fluctuation decays faster. Some of the energy is absorbed in the viscous liquid crystals while the effect response timing is still the same in Fig. 3.17 (a) (b) (c). After understand the relationship between the laser intensity and the density change, the one between the density change and refractive index change waits to examine.

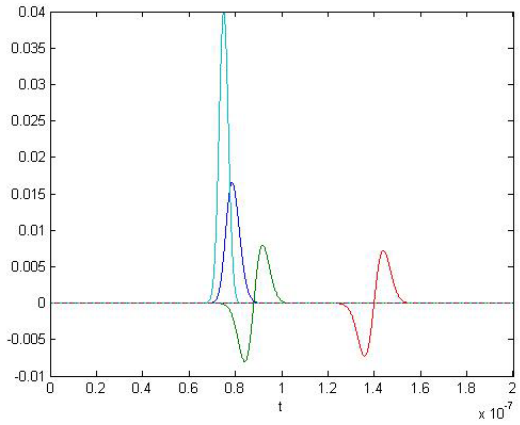

(a)

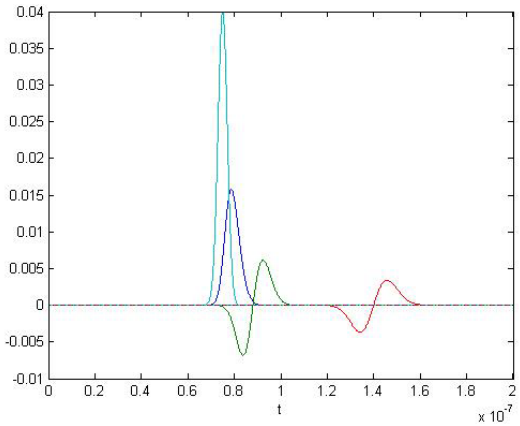

(b)

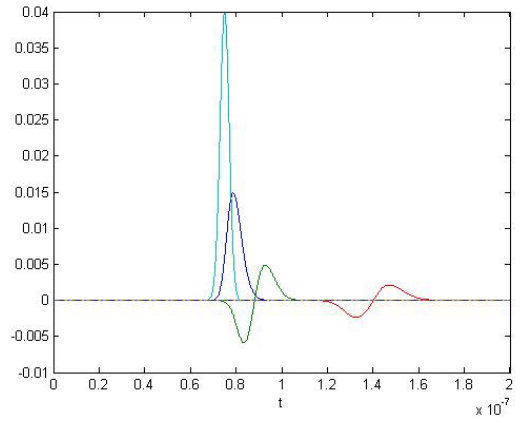

(c)

Fig. 3.17 Density fluctuation with different viscosities

(a) 1X (b) 10X (c) 20X

CHAPTER 4 IMAGE PROCESSING WITH NONLINEAR LIQUID CRYSTALS

4.1 Brief Introduction

Based on various laser induced nonlinear effects discussed above, we can apply the nonlinear liquid crystals in different areas. Traditionally, liquid crystals are used in displays by applying electro-optical effect. However, liquid crystals characterized as fast response nonlinear materials are also suitable for image processing. The previous experiment [80] proposed by Khoo and Shih caused the attention toward image application. Then, Yelleswarapu et al. [62, 63] also used this technology in medical purpose. Spatial filters and hologram with nonlinear liquid crystals are also investigated by several groups [64-67]. In this chapter, we proposed two image processing setups, intensity inversion and wavelength conversion. Complete theories and simulation will also be discussed in this part. In addition, that reading the invisible signal in a visible way with nonlinear liquid crystals is firstly proposed. The detail will be introduced later.

4.2 Phase Modulation with Nematic Liquid Crystals

4.2.1 4-F System

Image processing has been widely investigated and applied in different areas [71-73]. Different nonlinear photorefractive materials are used as significant elements in the image system [74]. Among them, nematic liquid crystals play a significant role possessing high induced refractive index change coefficient and high transmittance in broad visible range [28, 75-78]. Dye-doped liquid crystals also are proven as a promising candidate lowering the threshold power in application [43, 79].

Based on M. Y. Shih's demonstration [80], we proposed a simple 4-F optical system, shown as Fig. 4.1. In this system, we present the planar nonlinear liquid crystal film at the Fourier plane. With the phase modulated by different intensities, different image patterns will appear at the output plane.

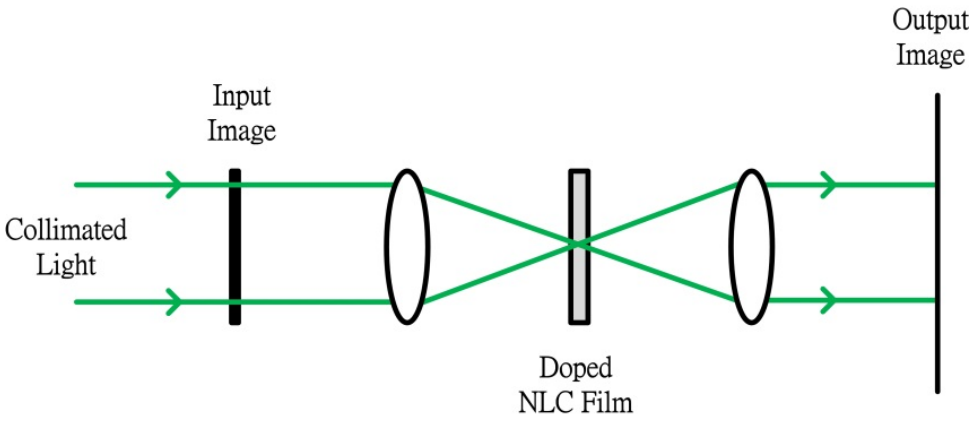

Fig. 4.1 Setup for self-phase modulation

$$F(\alpha) = \frac{1}{\sqrt{2\pi}} \int_{-\infty}^{\infty} f(x) e^{i2\pi\alpha x} dx \tag{4.1}$$

$$G(\alpha) = F(\alpha) e^{i\phi} \tag{4.2}$$

$$\phi = \frac{2\pi L}{\lambda} n_2 I(\alpha) \tag{4.3}$$

$$f'(x') = \frac{1}{\sqrt{2\pi}} \int_{-\infty}^{\infty} G(\alpha) e^{-i2\pi\alpha x'} d\,\alpha \tag{4.4}$$

Fig. 4.1 shows the optical demonstration for self-phase modulation image intensity inversion. A 50-μm-thick planar-aligned 0.5% MR-5CB (Pentyl-Cyano-Biphenyl) film is placed at the focal plane to perform the amplitude modulation of output signal by varying the input signal. The absorption spectrum of methyl red doped 5CB is illustrated as Fig. 4.2. The pattern in time domain transforms into frequency domain when the laser is focused on the focal point after the first lens; after the second lens, the pattern in frequency domain transforms back to time domain. In the system, we do some image processing by modulating the phase in frequency domain with a liquid crystal cell.

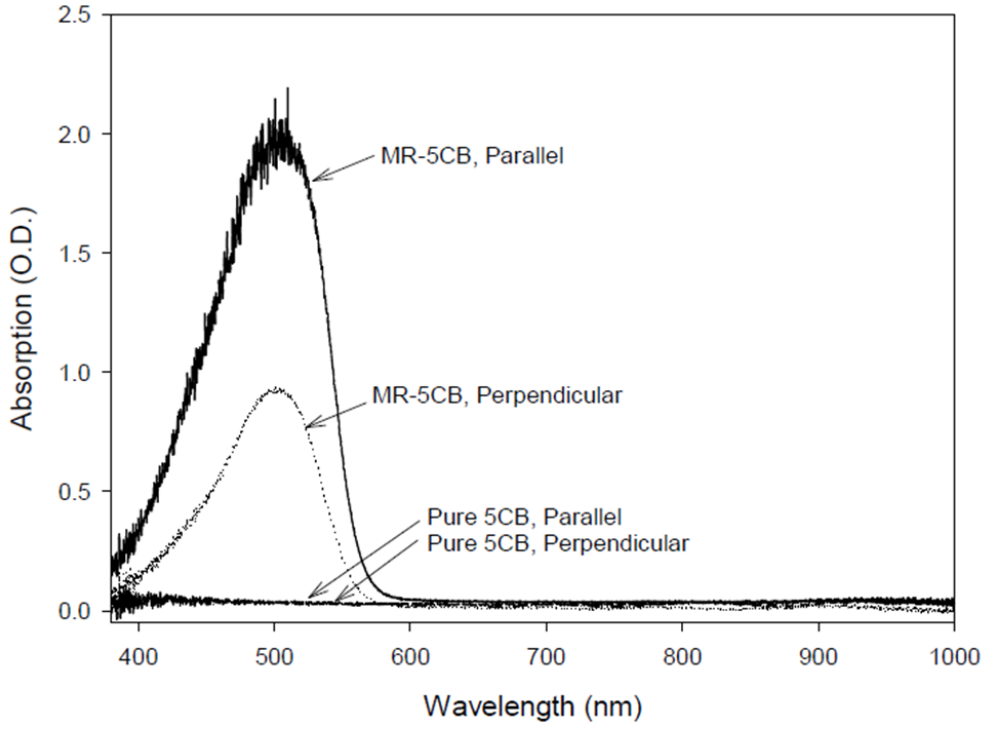

Fig. 4.2 Absorption spectrum of methyl red doped in 5CB with two different light polarization with respect to liquid crystal alignment

4.2.2 Experiment and Simulation Results

Fig. 4.3 shows the digital and experimental results of self-modulation. A 532nm ND:YAG laser is used as the input source. When the power increases around 0.5mW, the image intensity starts to invert. Because of the MR-NLC with lower absorption at 532nm, the larger threshold power around 0.5mW is needed to invert the image pattern.

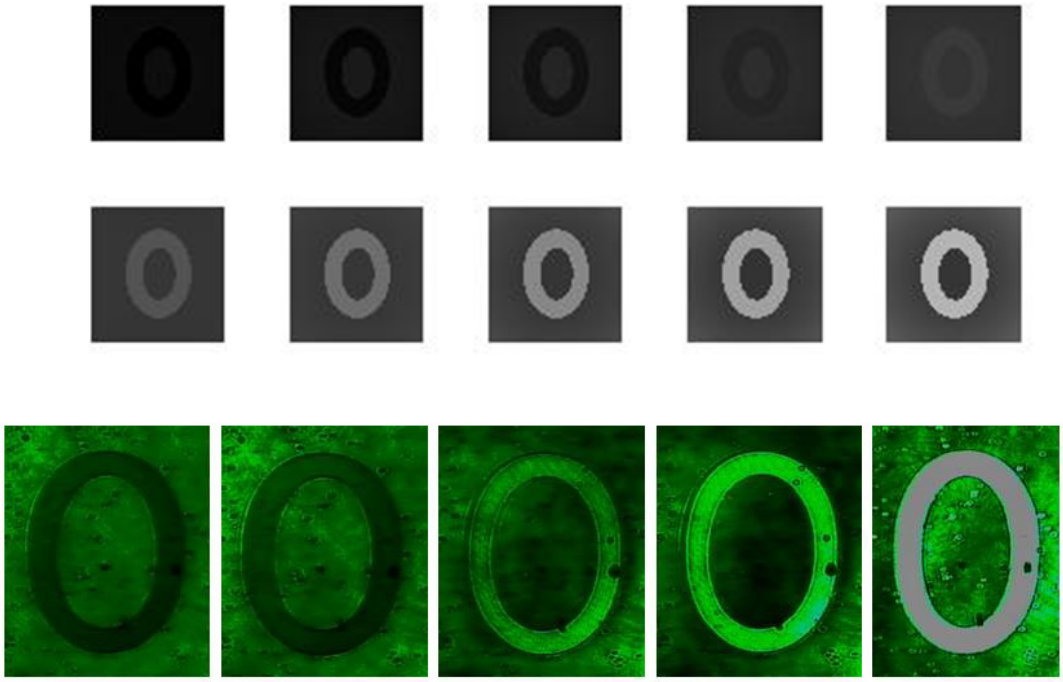

Fig. 4.3 Simulation and experiment results for self-phase modulation

According to the simulated patterns in Fig. 4.3, I digitalized the results and plotted the relation between the input and output intensity in two curves. While the blue curve represents the unblocked center part, the red curve represents the blocked ring part. In addition, one more circle, from bright to dark in the ring part was added. The whole circle of intensity inversion is illustrated as Fig. 4.4. The input intensity in the horizontal axis means the linear increasing, not an absolute value. Contrast ratio is used in Fig. 4.5 to better define the level of intensity inversion. The best contrast ratio as high as 3.5 happens in intensity inversion in our simulation.

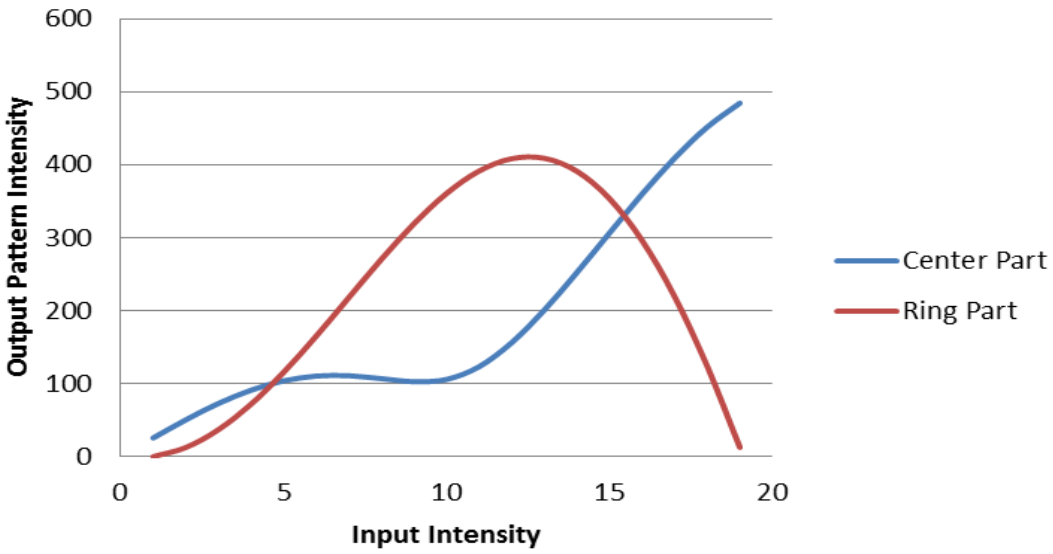

Fig. 4.4 Relation between the input and output pattern intensity in both blocked and unblocked parts in self-phase modulation setup

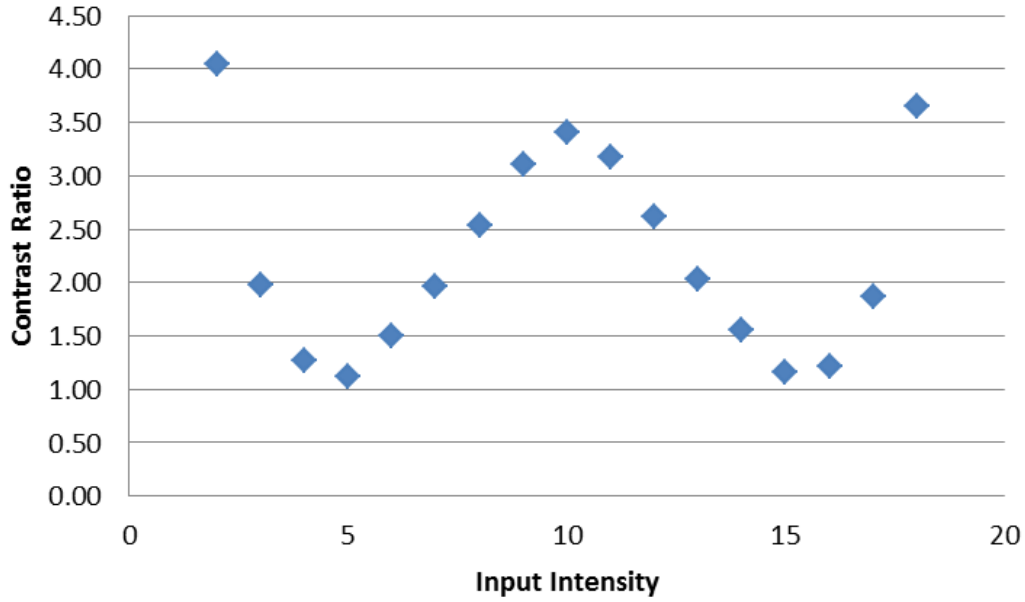

Fig. 4.5 Relation between input intensity and contrast ratio in self-phase modulation setup

Based on the theories and the simulation, the intensity dependent inversion is periodical. In Fig. 4.6, we used different profiles of patterns to illustrate the multi cycles of intensity inversion. In addition, cross-sectional views from the middles of the patterns are shown to provide clear illustration. With the increasing of intensity, the dark part will become bright and then dark again until the liquid crystal phase turns to liquid phase.

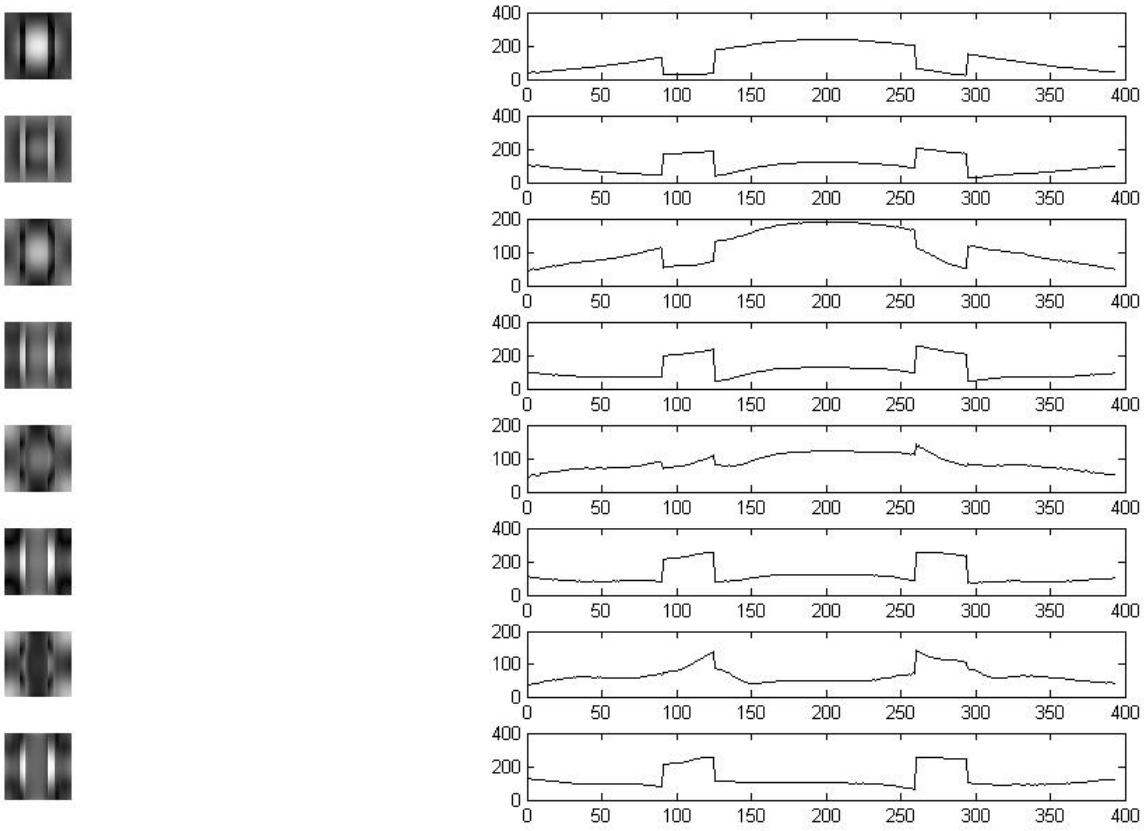

Fig. 4.6 Multi-cycles of periodical image intensity inversion

4.2.3 Control-Beam Phase Modulation

On the other hand, another demonstration shown as Fig. 4.7, control-beam phase modulation, is proposed for different wavelengths applied. We use green light (532nm) as a control beam and red light (671nm) as an imaging source. The transmission rate through the sample versus different wavelengths is illustrated as Fig. 4.8.

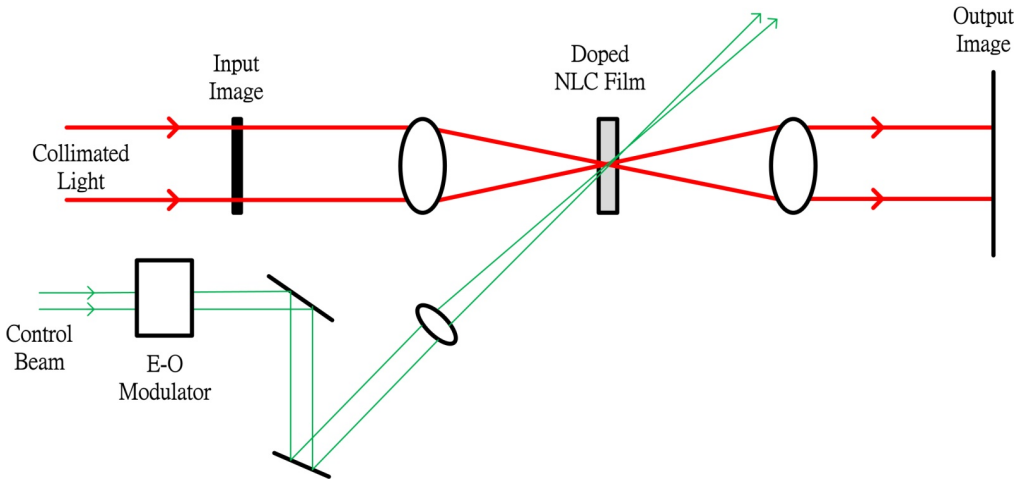

Fig. 4.7 Setup for Control-beam phase modulation

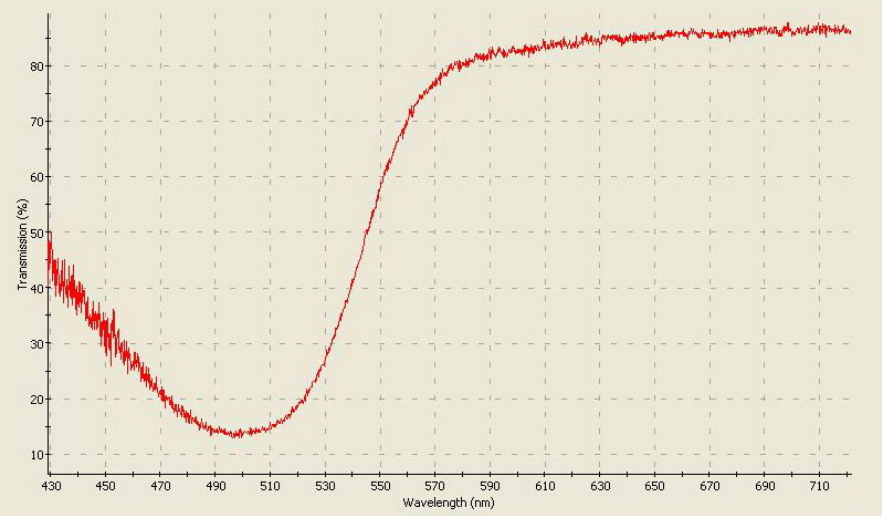

Fig. 4.8 Transmission through the sample (MR-5CB 0.5% 50μm homeotropical)

We choose solid-state laser (671nm; 21mW) as the image source in consideration of the detector limitation and the CCD resolution. As for the control beam, with the E-O modulator, the on-off time can be reached under several hundred nanoseconds compared to traditional mechanical shutter whose on-off time is around several milliseconds. In addition, we work to optimize the contrast ratio and lower the noise. Fig. 4.9 (a) (b) (c) represent the images with no control beam, low control beam power around 8uW and high control beam power around 60mW, respectively. Power as low as 60uW is enough to

invert the image, compared to previous several hundred micro watts.

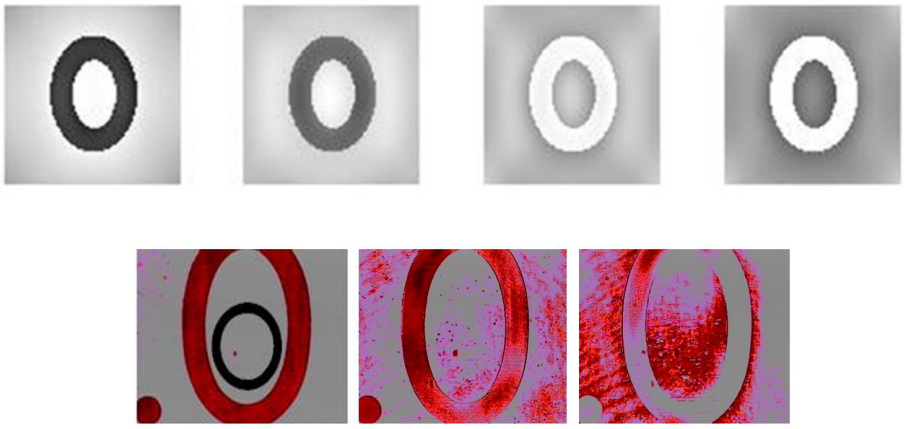

Fig. 4.9 Simulation and experiment results of the control beam image inversion

We also give further analysis in controlled beam intensity inversion experiments. The difference is that the profile in Fig. 4.10 seems symmetric with controlled beam applied while the probe beam does not account for interaction. The output intensity measured here is for probe beam 671nm. The contrast ratio is almost identical to the result in self-phase modulation setup, illustrated as Fig. 4.11.

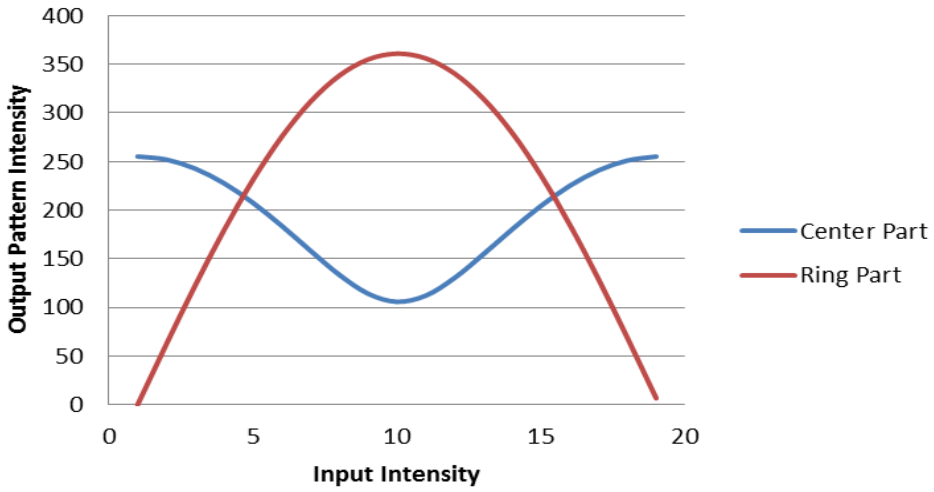

Fig. 4.10 Relation between the input and output pattern intensity in both blocked and unblocked parts in control-beam phase modulation setup

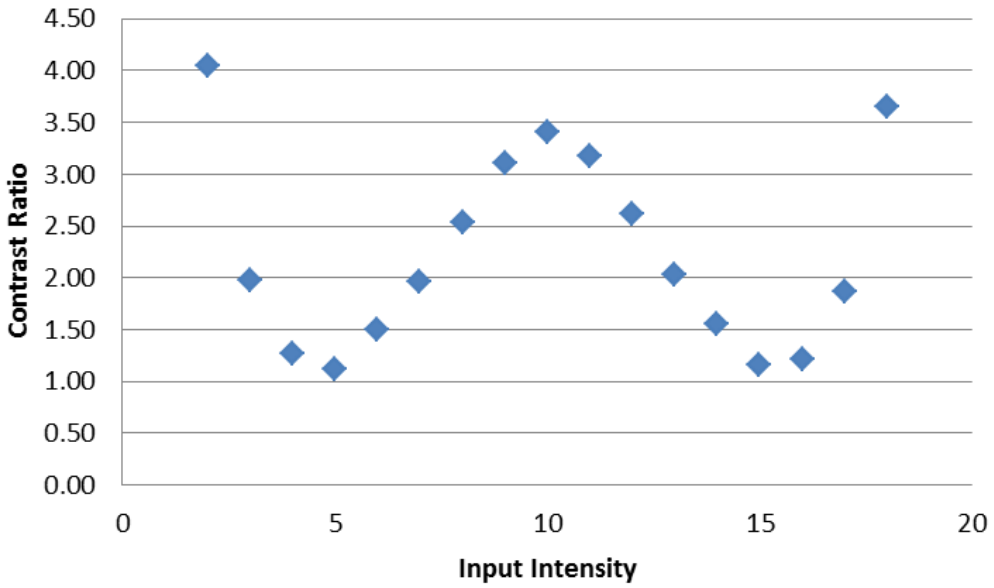

Fig. 4.11 Relation between input intensity and contrast ratio
in control-beam phase modulation setup

Here, we sample the central part of the ring (the black ring) to measure the response time. At low power, the central part of the ring is bright; when the power increases, it turns dark. The response time can drop down below 50μs as Fig. 4.12. It is almost 40 times faster compared former results around 2ms. This result proves MR-NLC can be a good candidate in imaging processing not only with the high nonlinear efficiency but the fast real-time response, avoiding the electro-optical or optical-electro conversion.

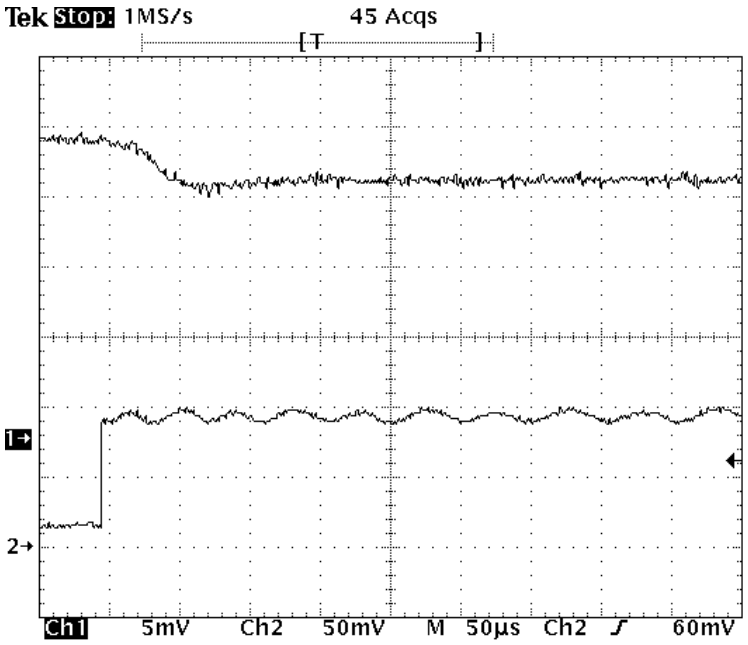

Fig. 4.12 The response time of image inversion with MR-NLC

4.2.4 Twisted Nematic Liquid Crystals Self-Phase Modulation

Consider another experimental setup shown as Fig. 4.13; twisted liquid crystals accompanied with two polarizers are presented in this system [81-82]. In this experiment, the twisted liquid crystal we used is 0.035% MR-5CB whose thickness is 50μm. The diameter of laser beam size focusing on the sample is around 45μm.

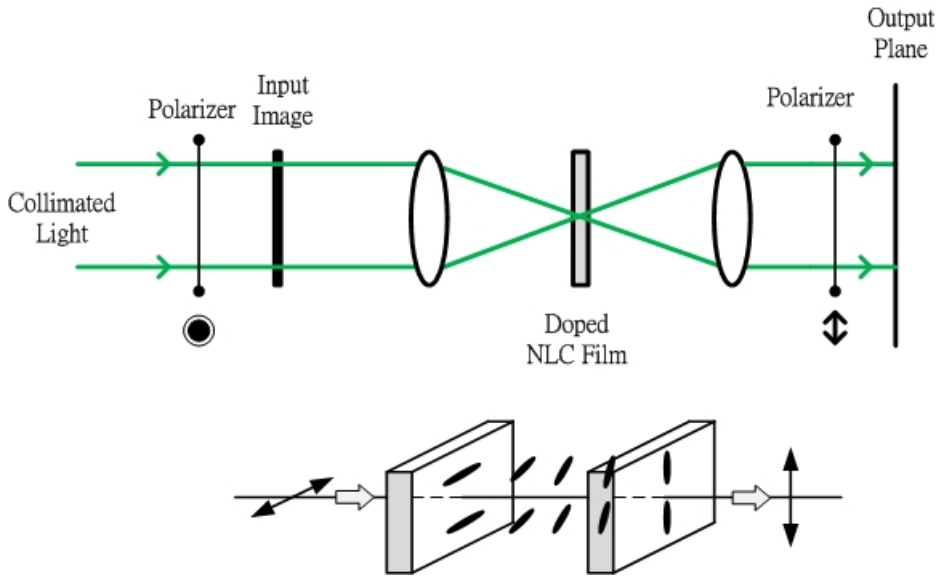

Fig. 4.13 Experimental setup with twisted nematic liquid crystals

The complete cycle with increasing powers in sequential order is illustrated as Fig. 4.14. The initial power is 0.24μW; the output image Fig. 4.15 (a) appears similar to the input image when the phase modulation is small. When the intensity of laser is increased, the intensity-inverted image is shown as Fig. 4.15(b). The reason is the same as above. We can state that the polarization of a polarized light will follow the liquid crystal orientation when the Mauguin condition ($d\Delta n/\lambda \gg 1$) is satisfied. However, while the intensity is large enough, that is $d\Delta n/\lambda \gg 1$ is not fulfilled anymore, the polarization of the beam is not oriented and blocked by the following polarizer. Here, lower-order component in the central part of the frequency domain is blocked. Hence, this lower-order component is attenuated while the higher-order component is not. The system behaves as a high-pass filter. Fig. 4.15(c) shows the edge enhanced image.

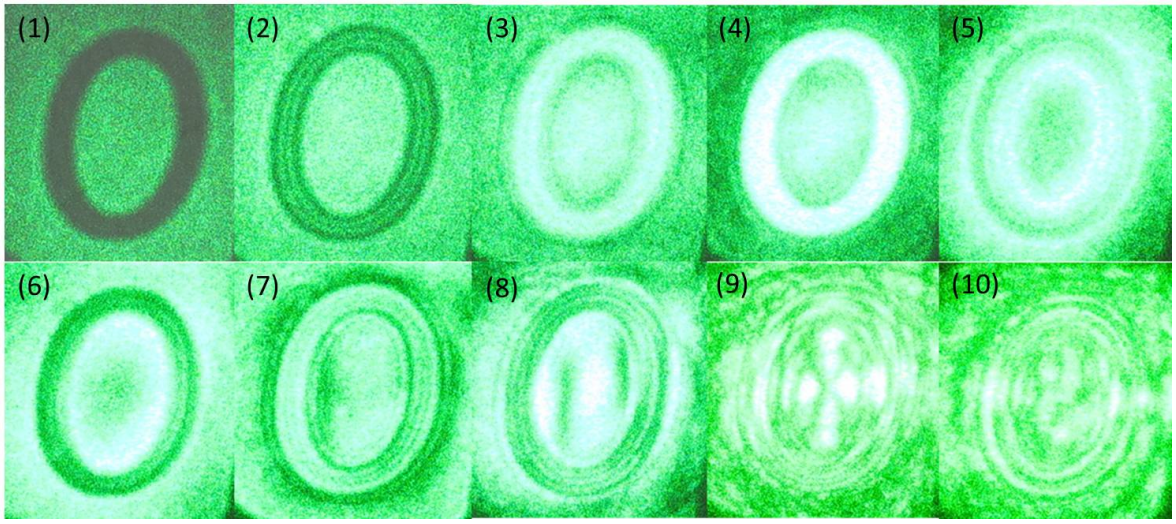

Fig. 4.14 Output images with increasing input powers

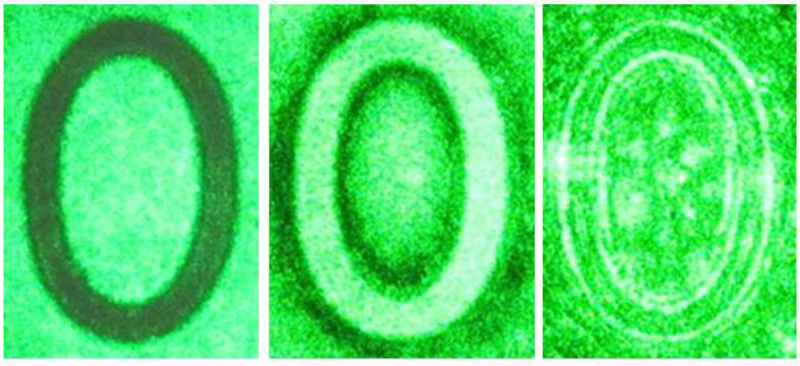

Fig. 4.15 Output images with different input powers impinging on the liquid crystal sample (a) 80μW (b) 2.5mW (c) 75mW

The effect of edge enhancement occurs when the laser induced bubble formation blocks the transmission in the frequency domain (the focal point after the first lens). We can have a better understanding in Fig. 4.16, in which (a) depicts the Fourier transform pattern in frequency domain without blocking and (b) illustrates the high power laser blocked in the center part. The numerical output image as a result of the situation in Fig. 4.16 (b) is shown as Fig. 4.17 (b) and Fig. 4.17 (a) is the numerical input image.

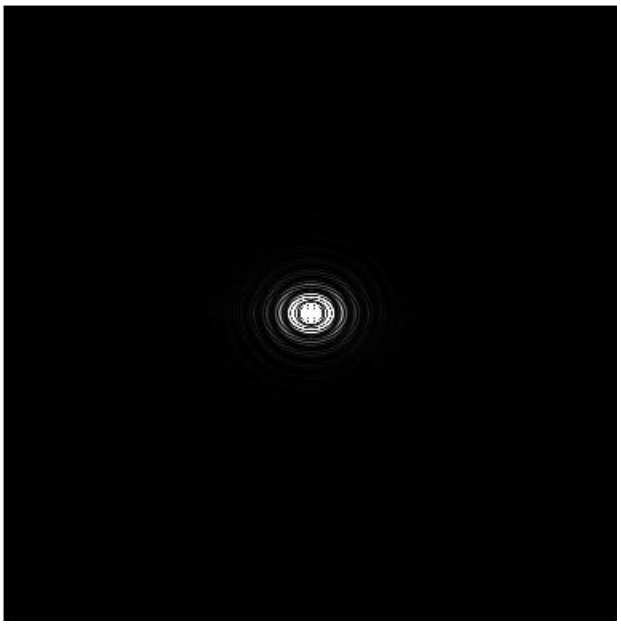

(a)

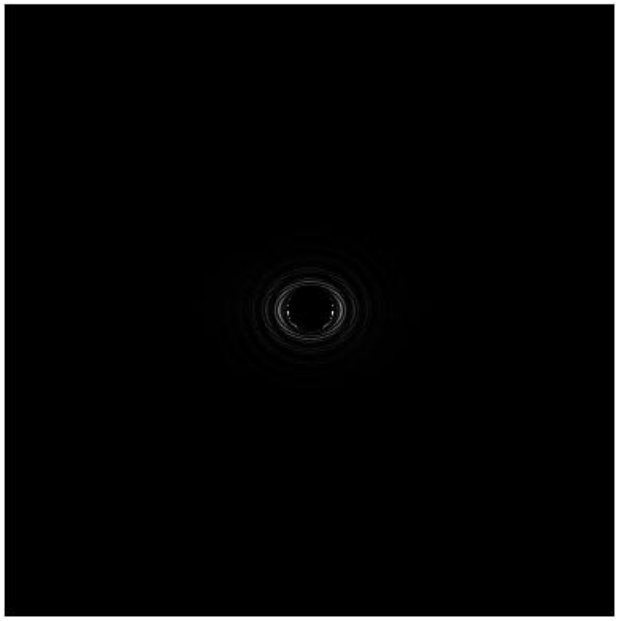

(b)

Fig. 4.16 Fourier transform patterns in frequency domain with
(a) low power input and (b) high power input

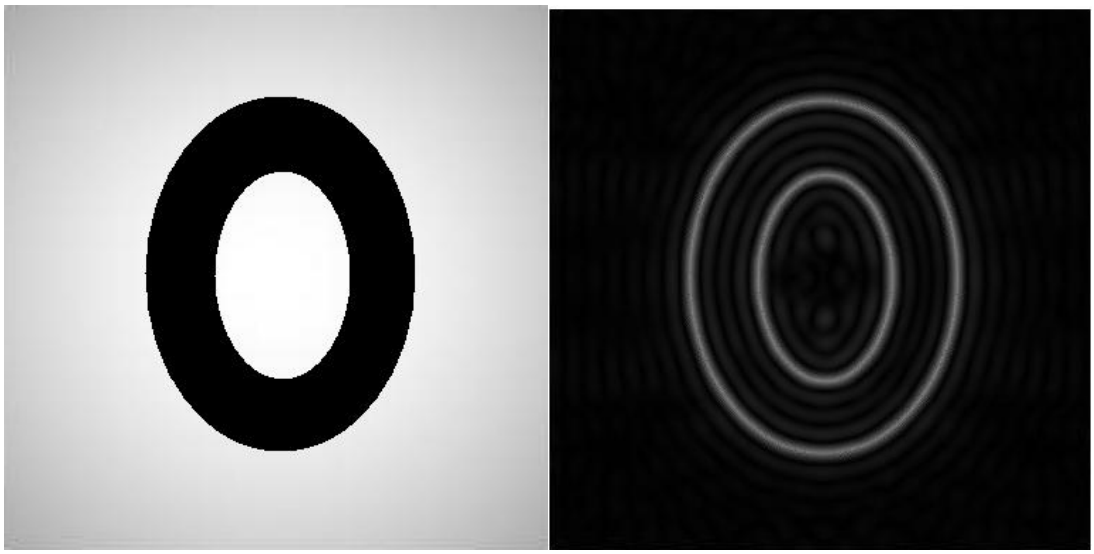

Fig. 4.17 Simulation of (a) input image and (b) output image when the input power is high enough to block the transmission and result in the effect of edge enhancement

In this part, we present a simple but efficient demonstration with dye-doped liquid crystals. Without other inputs or trigger sources, the dynamic process is only around 50μs. In addition, with the supra nonlinear liquid crystal, the input power needed to process is below 50μW and the contrast ratio reaches 3.5 when the patterns are inverted.

4.3 Near Infrared to Visible Conversion with Nonlinear Liquid Crystal

4.3.1 Huygens-Fresnel Diffraction

Nematic liquid crystals have been studied as promising nonlinear materials for decades, and applied in many fields such as displays, protectors, and sensors [8, 28, 83-86]. Because of the transparent character, liquid crystals are also perfect candidates for image processing [80, 87]. In addition to researches for visible light, some nonlinear properties of liquid crystals are investigated in near infrared [88]. In this section, we proposed a setup to detect an invisible signal and probe visibly with dye-doped liquid

crystals. Infrared signals with only few mini-watts can be read. Real time image processing is also realized in this passive system.

While the laser beam propagates through the dye-doped LCs, there are several laser-induced effects introduced, reorientation, density change, and thermal change. All of them account for the change of refractive index. Among them, the laser with high power is required for density change. However, in this demonstration, we use continuous-wave laser which is only several mini-watts to interact with the LC sample. Therefore, this density effect can be eliminated in this experiment. Also, the infrared laser (1550nm) in this setup is a random-polarized laser, and the doped LC sample is polarization independent to this infrared laser. The reorientation effect will be ignored. The major effect we discuss with here focuses on the thermal effect. The thermal induced order parameter change and density change and thermal index gradients in liquid crystals are elaborately illustrated by Khoo [28].

In this wavelength conversion setup, the main image theory is based on Huygens-Fresnel diffraction [71, 89]. Generally, diffraction means that a wave encounters an obstacle and we can divide the wave into several small waves. However, diffraction in optical field also occurs when the light travels through media with a varying refractive index, shown as Fig. 4.18. The Huydens-Fresnel approximation can be stated under the assumption that observation distance is much larger than the wavelength.

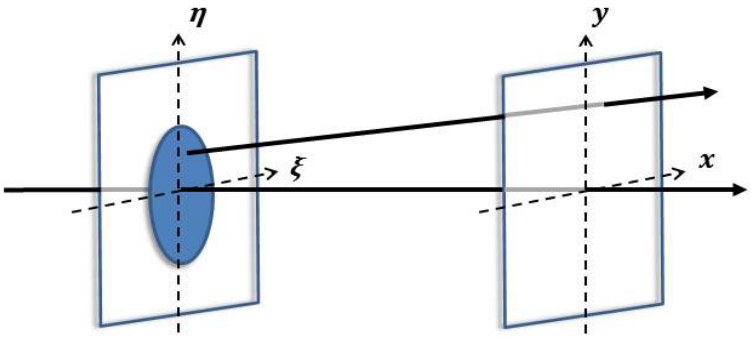

Fig. 4.18 Diffraction geometry

4.3.2 Epolight 1125 and Wavelength Converter Setup

The sample we used here is 50μm planar 1% Epolight1125-doped 5CB. The spectrum of absorption illustrates as Fig. 4.19. The Epolight1125-doped LC used highly absorbs near infrared around 80% and has low absorption 5% in 532nm, a perfect candidate in our infrared to green wavelength conversion. In addition, the absorptance for 1550nm through the dye-doped LC keeps the same in different input power levels before the phase transition as Fig. 4.20.

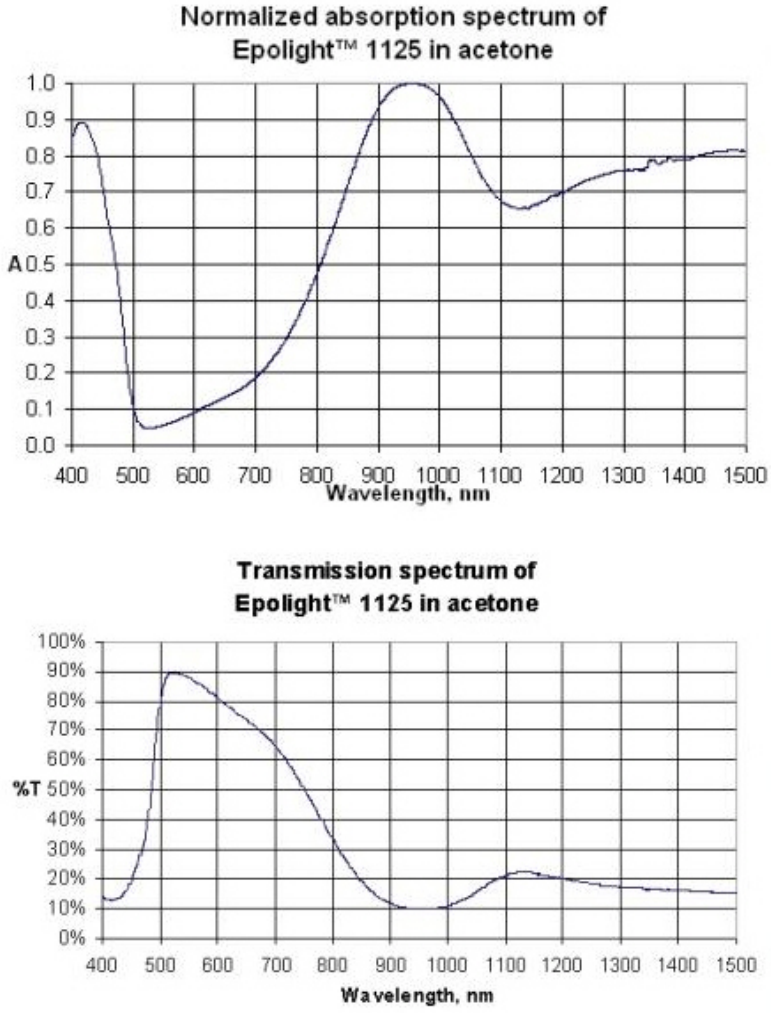

Fig. 4.19 Absorption and transmission spectra of Epolight1125 in acetone [90]

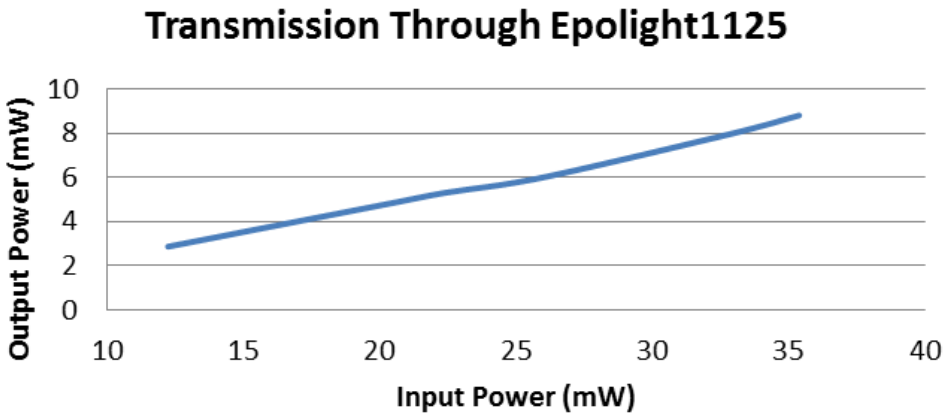

Fig. 4.20 Experimental transmittance of Epolight1125-doped 5CB

In this experiment, the image processing is divided into two parts. One is that the writing beam (infrared) impinges on the LC sample and writes the signal information on the sample. At the same time, another green beam is coupled to overlap in the same area of the sample to read the signal. The setup is illustrated as Fig. 4.21.

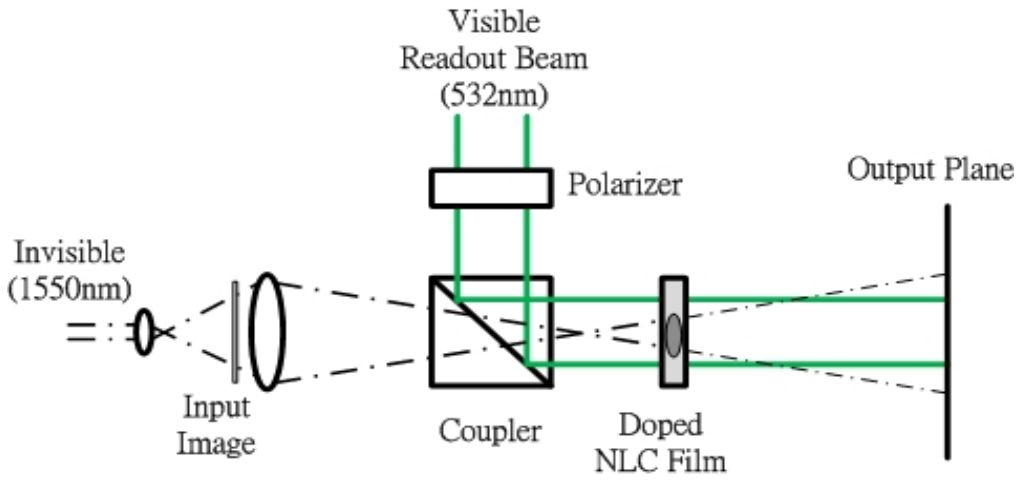

Fig. 4.21 The wavelength conversion setup

The infrared laser we used here is randomly polarized continuous-wave laser and the Gaussian intensity through the mask pattern can be represented as Eq. (4.5).

$$I = I_0 e^{\frac{-2r^2}{w^2}} \cdot mask\ pattern \tag{4.5}$$

The infrared laser will map the same image pattern on the liquid crystal sample. Some parts block the laser while some allows the laser to propagate. When the infrared laser propagates through the Epolight1125-doped liquid crystal sample, the dyes absorb highly this invisible beam and transfer into heat. The optical field induced refractive index change rises with the increasing of the temperature, especially in the vicinity of the clearing temperature Tc. The steady-state thermal nonlinear coefficient $n_2(T)$ can be expressed as follows:

$$n_2(T) = \frac{\alpha}{\rho_0 C_v \Gamma_R}\left(\frac{dn}{dT}\right) \tag{4.6}$$

Where α is absorption constant, ρ_0 is the unperturbed density of the liquid crystal, Γ_R the inversed relaxation time, and C_v is the specific heat. From this equation, the thermal change originated from optical intensity is related to how the media absorbs light and transfers into heat and how the heat diffuses. In steady state (t=$\Gamma_R{}^{-1}$), we can estimate the nonlinear thermal coefficient according to liquid crystalline parameters.

The writing beam results in the refractive index change. The probe beam with different polarization will see the change of the refractive index. Two special cases are discussed here. One is that the polarization of the probe beam is parallel to the direct axis of liquid crystals. The other is perpendicular. The equations for the effective index seen from the probe beam can be approximated as follows.

$$\text{Parallel} \quad n_{eff} = n_e - n_{2e} \cdot I \tag{4.7}$$

$$\text{Perpendicular} \quad n_{eff} = n_o + n_{2o} \cdot I$$

With the reading beam overlapping in the same area where the writing beam impinges, there is different phase shift applied to the optical field because of change of refractive index as Eq. (4.8).

$$U(\xi, \eta) = U(\xi', \eta') e^{j\frac{2\pi n_{eff}}{\lambda} d} \tag{4.8}$$

In Eq. (4.8), the effective index should be modified because the index is fixed at two boundaries. Therefore, the index is not a constant through the whole LC sample. Here, we assume that Δn is positive and index change is approximated by a sinusoidal form as Fig. 4.22. As a result the effective index can be modified as Eq. (4.9). A factor π/2 is introduced to fulfill the hard boundary condition.

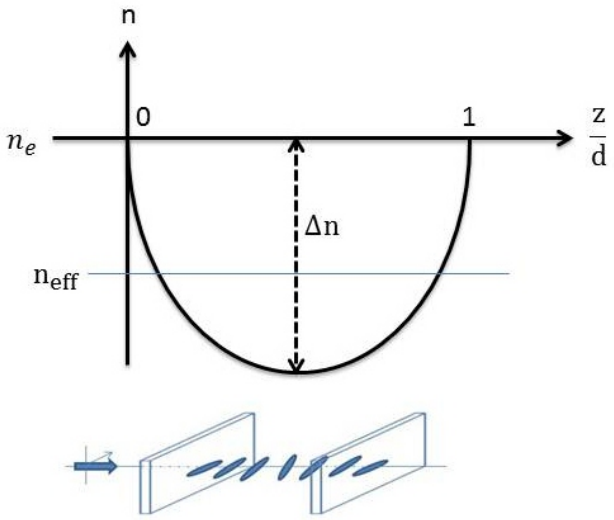

Fig. 4.22 The modified effective index with two boundaries fixed

$$\phi = \int_0^d \frac{2\pi}{\lambda}\left[n_e - \Delta n \cdot \sin\left(\frac{\pi z}{d}\right)\right] dz = \frac{2\pi}{\lambda}(n_e - \Delta n \cdot \frac{2}{\pi})d \qquad (4.9)$$

$$n_{eff} = n_e - \Delta n \cdot \frac{2}{\pi}$$

$$n_{eff} = n_o + \Delta n \cdot \frac{2}{\pi}$$

We achieve a visible diffraction pattern from an invisible signal with a simple nonlinear LC film as follows.

$$U(x,y) = \frac{e^{jkz}}{j\lambda z} e^{j\frac{k}{2z}(x^2+y^2)} \iint_{-\infty}^{\infty} \{U(\xi,\eta)\, e^{j\frac{k}{2z}(\xi^2+\eta^2)}\} e^{-j\frac{2\pi}{\lambda z}(x\xi+y\eta)} d\xi d\eta \qquad (4.10)$$

$$I(x,y) = U(x,y) \cdot U^*(x,y) \qquad (4.11)$$

In this setup as Fig. 4.21, the first lens is used to expand the beam size and the second one is used to slightly focus the infrared laser on the LC sample. The diameter of the writing beam on the sample is 2mm. The induced change of refractive index within the LC sample results in the phase difference in different areas seen by the green laser.

4.3.3 Experiment and Simulation Results

From Fig. 4.23, temperature dependence of the refractive indices of 5CB in the visible spectrum, we can see the effective refractive index in isotropic phase is 1.597 while n_e is 1.740 and n_o is 1.545 in crystal phase for 532nm. In this experiment, probe beams with two different polarization parallel or perpendicular to the direct axis of LC will result in the difference of diffraction patterns, shown as Fig. 4.24. With the parallel polarization, the refractive index seen from this beam is dropped from 1.740 when 1550nm laser is applied. On the other hand, with the perpendicular polarization, that is increased from 1.545. Using the reading beams with different polarization, we can get two totally inverted patterns as Fig. 4.24. In addition, according to Fig. 4.23, the slope of n_e around 25°C is around 0.005/°C; that of n_o is 0.001/°C. The decreasing rate of refractive index is larger than the increasing ones under the same applied field almost five times. Therefore, this reflects on both of the experiment and simulation results. From Fig. 4.24, the parallel polarization has better image in contrast ratio than the perpendicular one. The near infrared laser is only 35mW, whose diameter of the beam is 2mm, and 1.2mW green laser is applied here to read the signal.

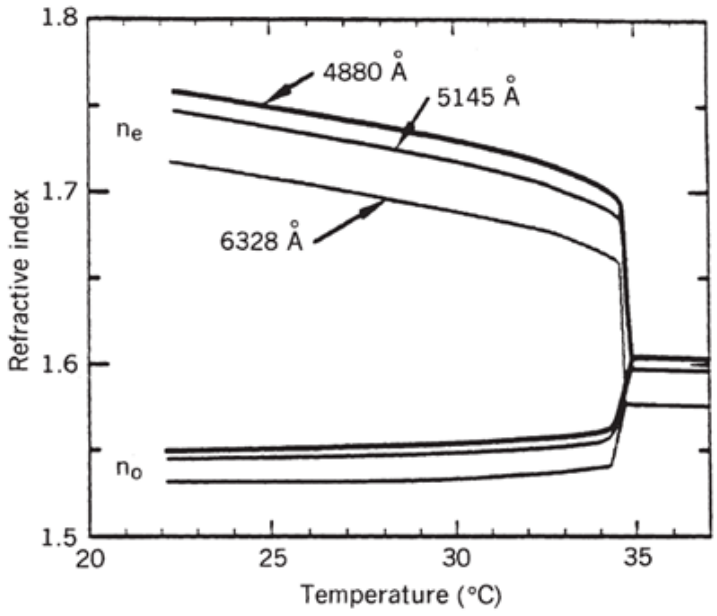

Fig. 4.23 Temperature dependence of the refractive indices of 5CB [28]

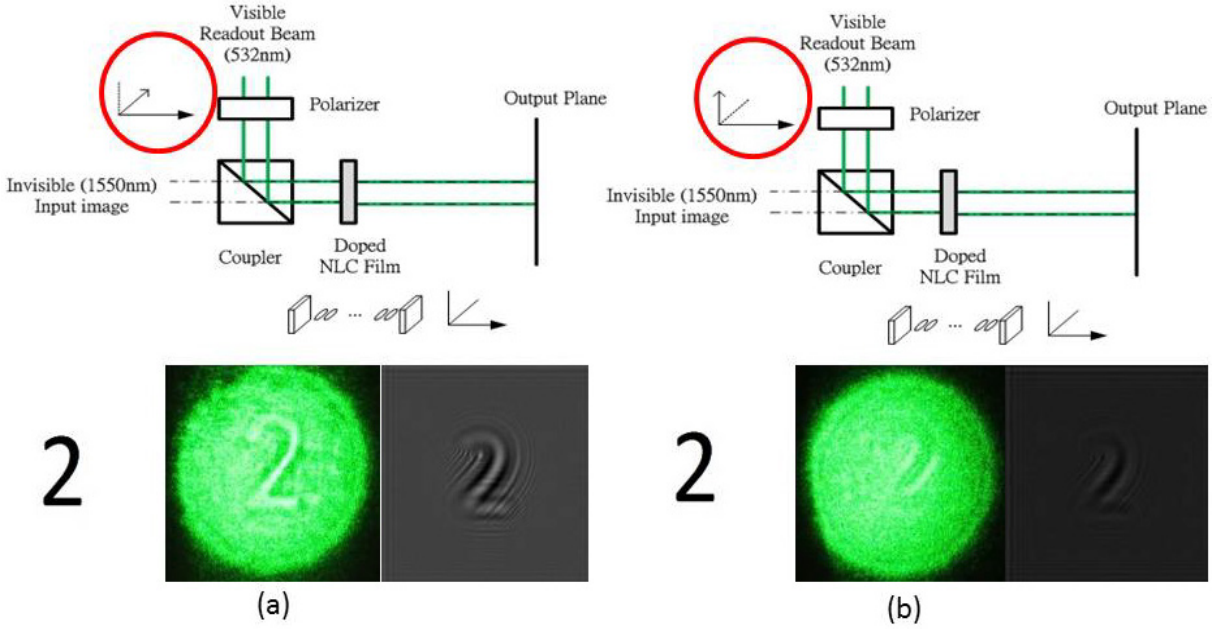

Fig. 4.24 Diffraction patterns with the probe beam whose polarization is (a) parallel (b) perpendicular to the director axis of liquid crystals

Furthermore, when the intensity of laser increases, the temperature dependent refractive index change rises, resulting in sharper diffraction patterns. Using Mach-Zehnder interference, we achieve the phase shift 2/3π, which is 0.004 in refractive index change under the 35mW input. The typical values of dn_e/dt and dn_o/dt are 0.005/°C and 0.001/°C, respectively. Here, the n_{2e} is estimated approximately 1.8×10^{-3} cm^2/W whereas n_{2o} is 0.36×10^{-3} cm^2/W. Away from the clearing temperature, the total n_2 value is approximately 2.16×10^{-3} cm^2/W.

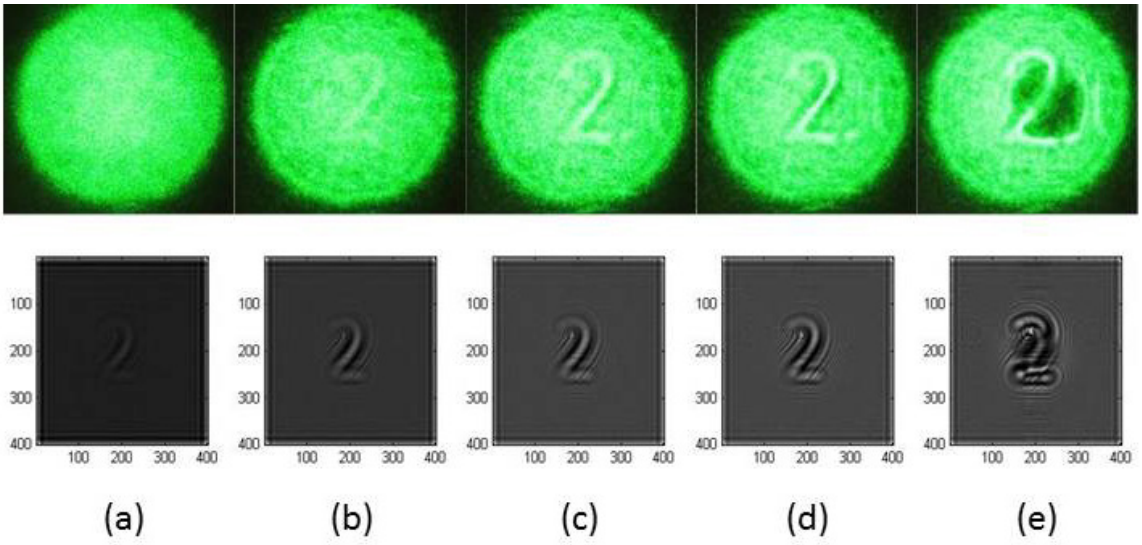

Fig. 4.25 Diffraction patterns from both experiment and simulation under different intensity levels of near IR lasers (a) 5mW (b) 20mW (c) 35mW (d) 55mW (e) 60mW

Fig. 4.25 is the diffraction results in different power levels. We use the probe beam with parallel polarization. At 55mW with beam diameter of 2mm, the intensity is around $1.75W/cm^2$, reaching the maximum threshold of phase transition. With higher powers, dyes keep absorbing infrared and turning into heat. The heat transfers from the center and the dark spot appears due to the rapid change of the refractive index which is near the phase transition. Overall, the heat generation rate is linearly proportional to the input intensity. At moderate intensity level, the simulation is well fitted to the experiment results as Fig. 4.25 (b) (c) (d). However, in lower or higher intensity level, the relation

between index change and intensity is not linear. Especially in higher intensity level, the energy is high enough to heat the sample into liquid state. The thermal index gradients are not linear anymore. The n_{2e} is approximately 3 times larger at input power of 60mW.

We also digitalize the performance of the diffraction pattern in different power level as Fig. 4.26. From this curve, we can get better contrast ratio with higher input power.

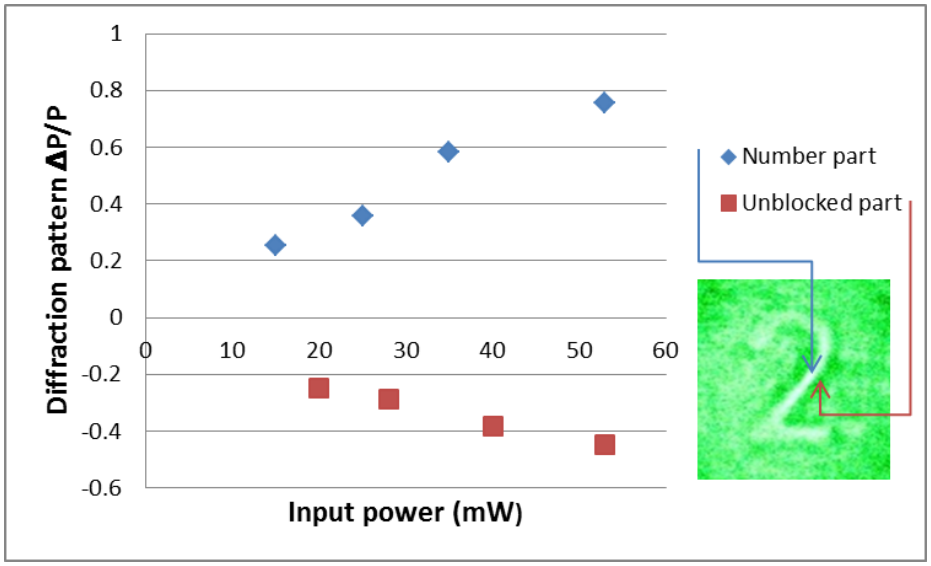

Fig. 4.26 Digitalized diffraction pattern in different input powers

Instead of 50μm, we used the 100μm sample with 1% epolight1125 and try to lower the input power. The 1550nm signal as low as 1.5mW is achieved with the beam diameter of 0.75mm to be probed with the green light.

On the other hand, the diffraction images are independent on the power of probe beams. From Fig. 4.27 different power levels, 0.15mW, 1.2mW, and 22mW are applied in the experiments with the same 1550nm power of 35mW. The output patterns are almost identical.

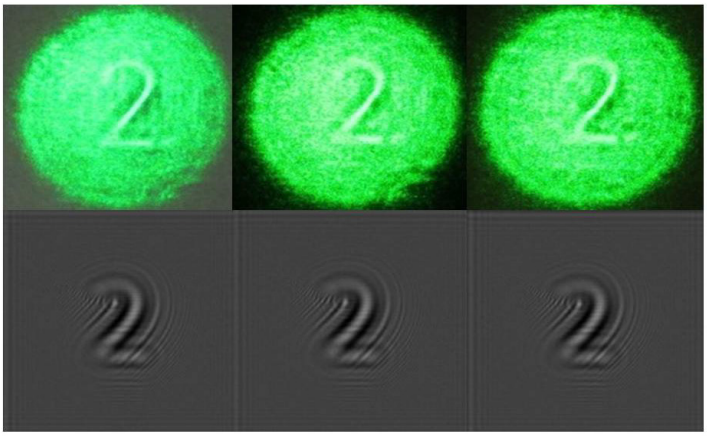

Fig. 4.27 Diffraction patterns under different powers of the probe beam
(a) 0.15mW (b) 1.2mW (c) 22mW

An alternative substrate is introduced. We compare the normal glasses and ITO glasses. Here, the sample we used is 50μm pure 5CB. The absorption at 1550nm is increased 10% with ITO glasses. In Fig. 4.28, with the same intensity, the pure sample with ITO shows some effect. However, no signal appears with normal glasses.

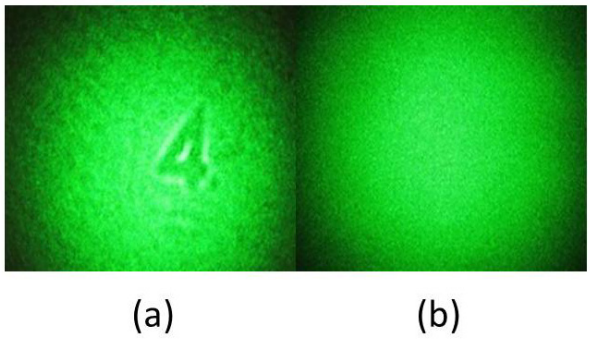

Fig. 4.28 Diffraction patterns under different substrates
(a) ITO glasses (b) Normal glasses

Dynamic analysis in this setup shows as Fig. 4.29. The response time is around 70m*s*. With higher input power which causes the thermal effect, the response time is shorter, ranging from 80ms down to 60ms.

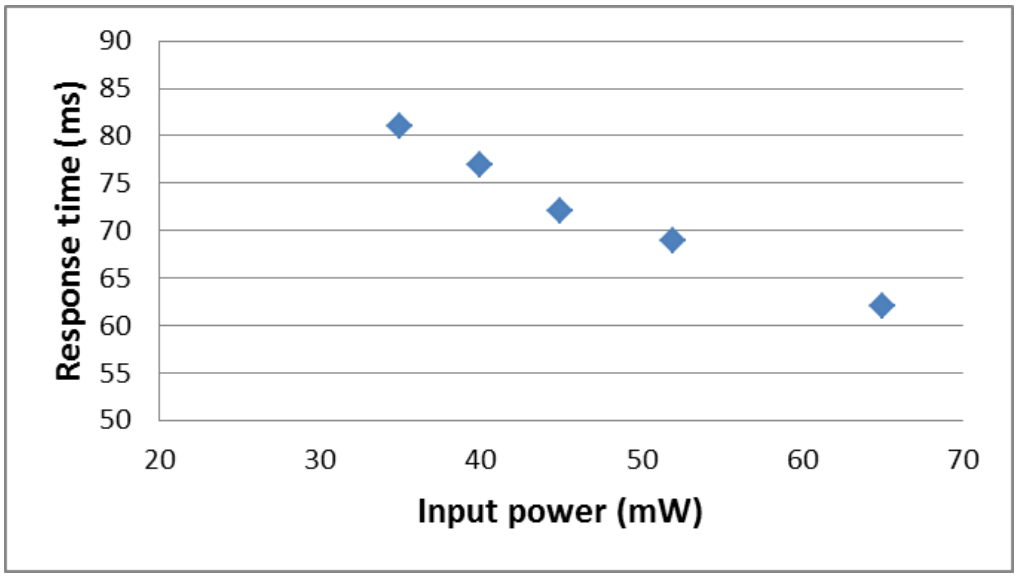

Fig. 4.29 Dynamic response of image processing with LCs in different power levels

4.4 Summary

In this chapter, we demonstrate a real-time all-optical image system with a nonlinear liquid crystal film. In this demonstration, two image processing are achieved: intensity inversion and edge enhancement. With input optical power as low as 60μW, the brightness of the pattern illustrated inverted because of self-phase modulation. We further work to achieve the more explicit response time whose resolution could be down to several hundred nanoseconds, 40 times faster than the previous measurement. On the other hand, with twisted nematic liquid crystals and two polarizers, the film behaves as a high pass filter in an optical system, enhancing the effect of the edges in an easy way.

Second, we proposed a simple real-time IR detector. With planar Epolight1125-doped LC, we successfully read the invisible signal in a visible way. Also, two different reading modes are provided. The IR power as low as 1.5mW can be read in this experiment. In addition, different parameters, such as thickness, substrates, input intensity, and polarization are reported in this article. The response time in this passive image system is measured down to 60ms.

CHAPTER 5 BLUE PHASE LIQUID CRYSTALS

5.1 Properties of Blue Phase Liquid Crystals

In many cholesteric liquid crystals, one or more intermediate phases occurs in the transition between helical cholesteric liquid crystals phase and isotropic phase, called cholesteric blue phases. This subtle effect however remains unexplored for more than eighty years until experimental results published by Reinitzer in 1888 [1]. Because of the spontaneously self-assemble helical structure, blue phase liquid crystals attract huge attention. The properties are totally different from the nematic liquid crystals though the formation of blue phase liquid crystals is to apply chiral agents in nematic liquid crystal host [91-99]. The blue phase exhibits selective Bragg reflections of visible light because of its spontaneously self-assembled three dimensional cubic structures with lattice periods of several hundred nanometers [100-105].

Since then, blue phases attracted high academic interest but were not expected to be very useful, because the temperature range of their existence is rather small. During the past few years, systems have been developed which exhibit blue phases stable within temperature intervals as large as 60°C [16, 106-107]. Even a promising prototype of a blue phase display was presented in 2008.

.

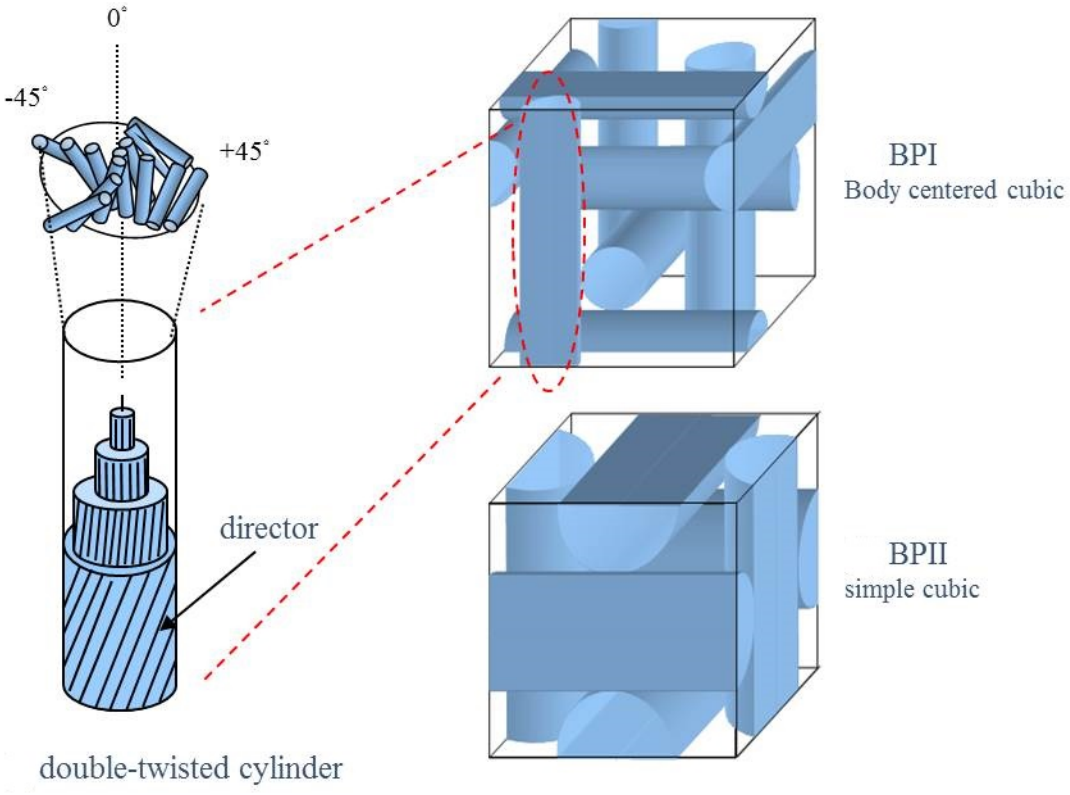

Fig. 5.1 Double helix arrangement of the BPLC director axis and the crystal lattice structures corresponding to the BPI and BPII phases [108]

Blue phases I and II are 3-dimension regular lattices of disclination of the helical director axis arrangement with typical lattice spacing on the order of several-hundred nanometers, depicted as Fig. 5.1 and thus they exhibit selective Bragg reflections of visible light, around 400nm. Although the nonlinear coefficient of BPLC is smaller than that of nematic liquid crystals, there are advantageous optical properties of BPLC such as their bandgap from 3-D photonic crystal lattices, polarization independence, and no surface alignment needed [110-115].

Because of the lattices and the existing phase (BPI or BPII) are closely related to the temperature. Therefore, we examine the properties of BPLC by controlling the temperature. Thermal hysteresis has been observed during the phase transition between the cholesteric liquid crystal phase and the blue phase, depicted as Fig. 5.2 [106].

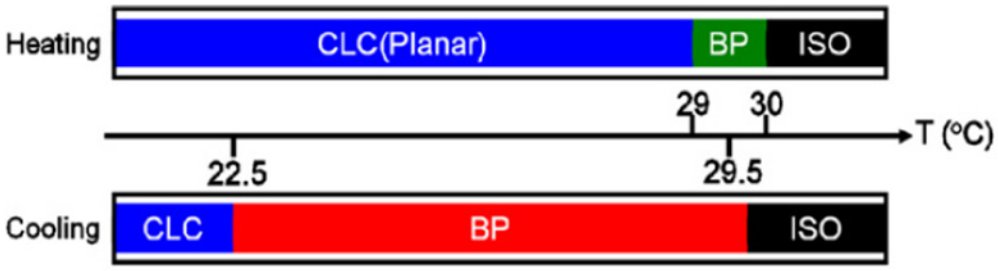

Fig. 5.2 Sequence of blue phase during heating and cooling [106]

Fig. 5.2 presents the sequence of phases of sample upon heating up. The blue phase existed over a temperature range of 7°C, which is wider than that (1°C) over which a typical blue phase exists. Fig. 5.3 is the homemade BPLC sample. In the transient photo, three phases, isotropic, BPI, and BPII, exist at the same time. The cool air comes from the right side and diffuses into the left side gradually.

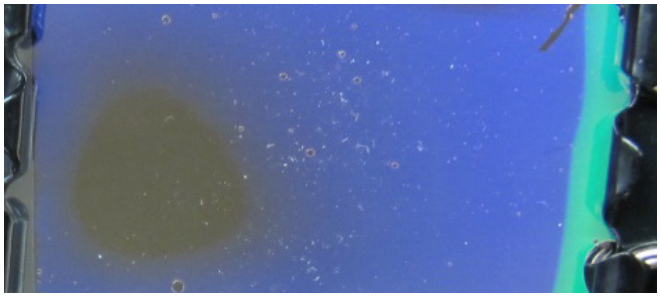

Fig. 5.3 The existence of three phases, isotropic, BPI, and BPII

In addition, we measure the spectrum of BPLC sample from 450nm to 750nm under different temperatures. Because of the blue phase range is narrow in heating process. We heat the BPLC into an isotropic phase and then cool down and record the spectrum at specific temperature. Form Fig. 5.4 the transmittance in isotropic phase is around 80%. When the temperature cools down, the spectrum shifts to the long wavelength side. At 29°C the sample reflects blue color, and the green and red transmit well, called BPII. At 28°C the partial green light starts to be reflected while the red keep

transmitted. The curves in Fig. 5.4 exist between BPII and BPI when the color turns from blue to very green.

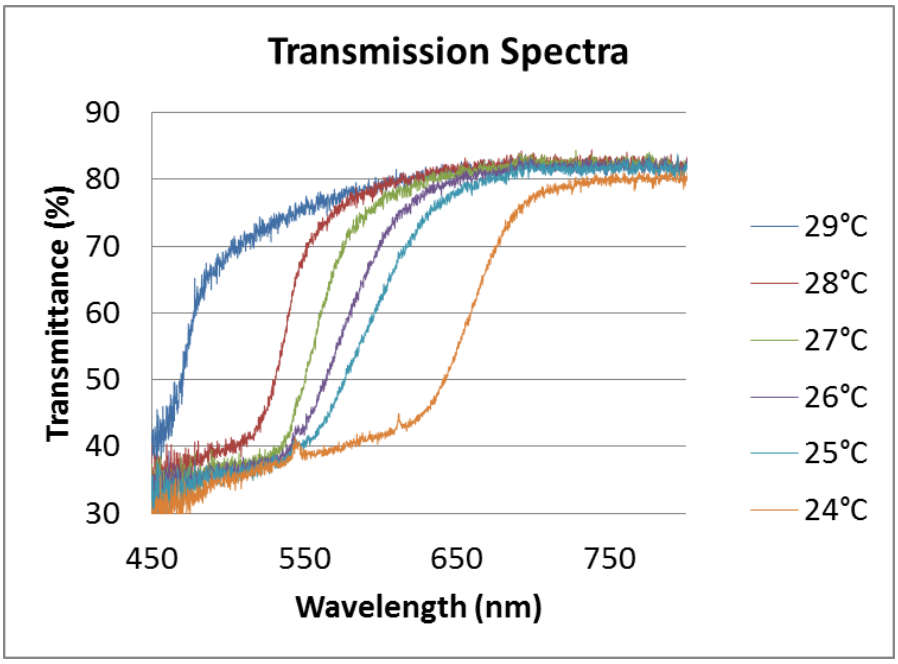

Fig. 5.4 Transmission Spectra of BPLC under different temperatures

5.2 Thermal Refractive Index Gradient in BPLCs

We use Mach-Zehnder interference setup to understand the refractive index change. Here, we use HeNe laser (632nm) as a source and insert the BPLC sample, which is placed inside a good thermal controlled container into one of the path. After heating up the temperature to 50°C, we drop the temperature down in a very slow rate. With the change of temperature, the refractive index will change, resulting in the path difference. The interference patterns also shift in some specific direction. Using a slit to sample some specific point to understand the shift situation, and the result is illustrated as Fig. 5.6

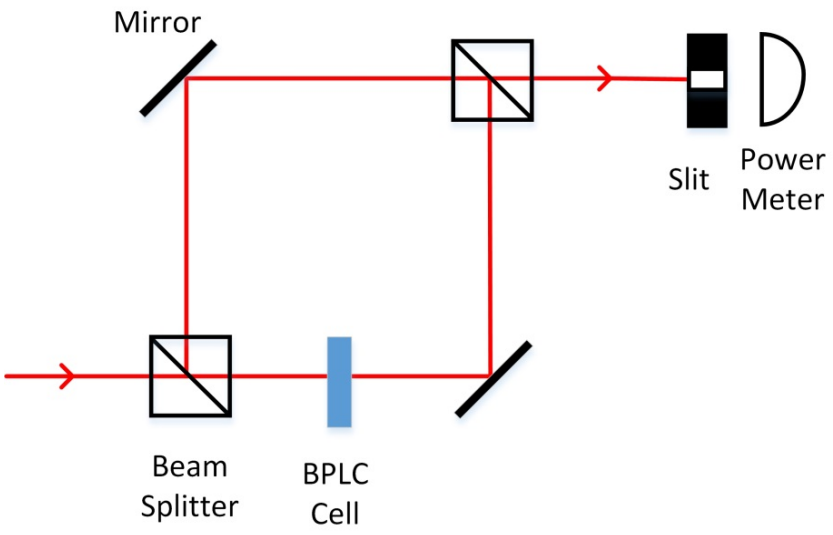

Fig. 5.5 Mach-Zehnder interference setup whith
blue phase liquid crystal on one path

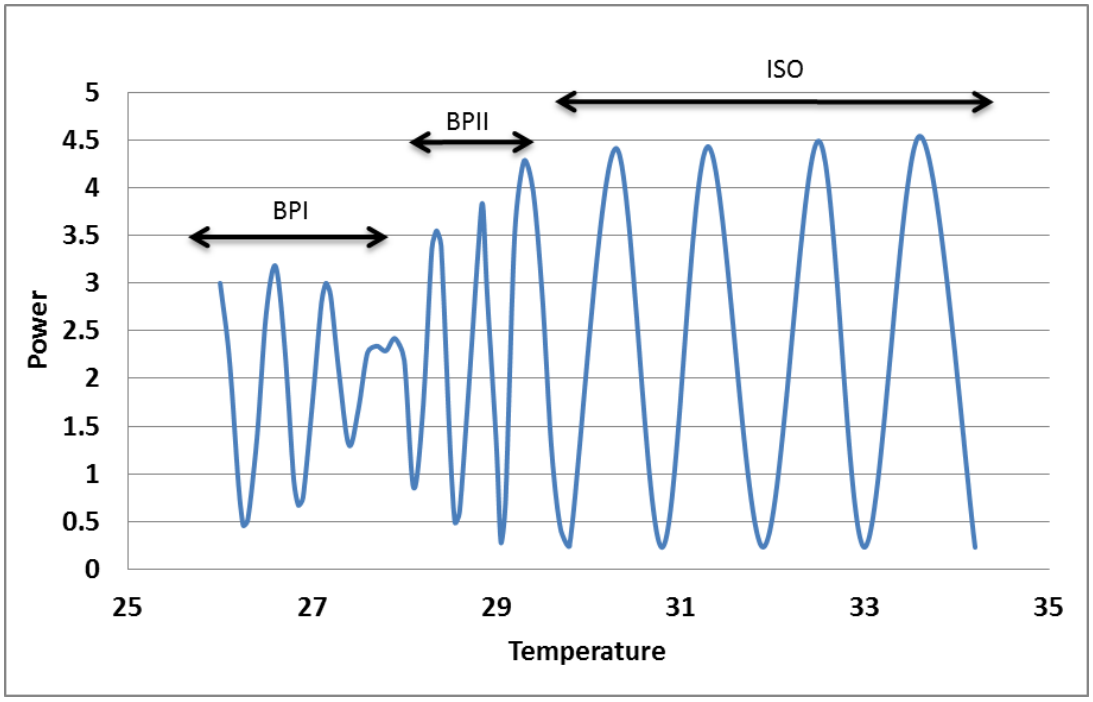

Fig. 5.6 Interference bulk cell give rise to moving fringe pattern
detected by the slit-detector.

From Fig. 5.6 the curves above 30˚C are almost identical. The shapes, the slope of curves, illustrate the same rate of refractive index change. Therefore, above 30˚C, we define the BPLC is in isotropic phase. When the temperature keeps going down, the peak power detected is decreased, which means the BPLC enters another phase, BPII. In addition, the slope is sharper than the curves in isotropic phase. It depicts that the different refractive index change rate occurs in different phases. Around 28˚C the slope appears not so shaper as BPII and meanwhile the peak power level decreases continuously. We understand that the BPLC enter BPI. From the experiment data mentioned above, the overall rate of refractive index change in BPLC in different temperature can be realized in Fig. 5.7.

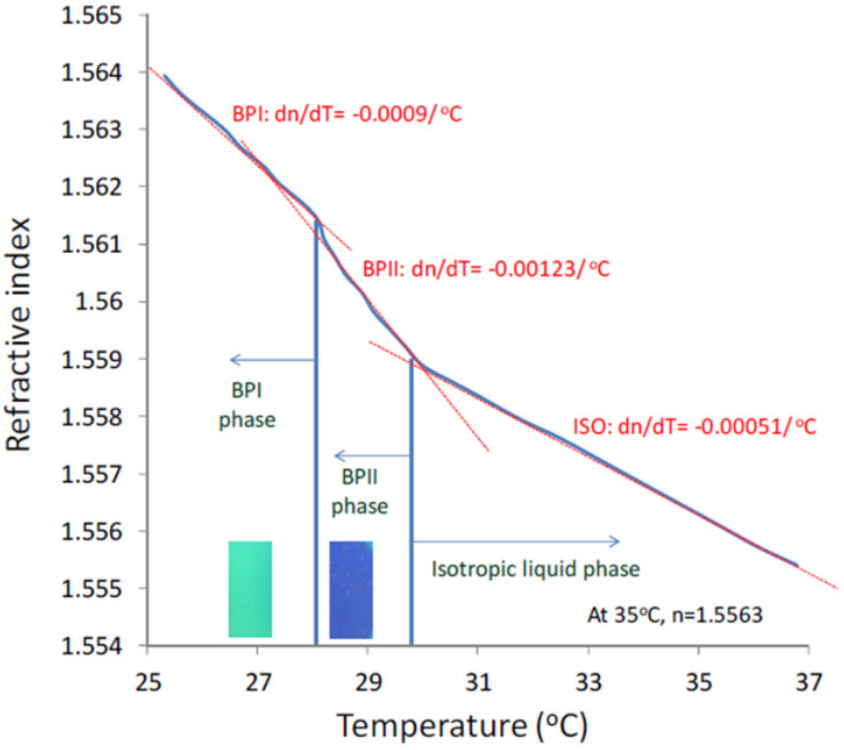

Fig. 5.7 Temperature dependent refractive index of 1-mm thick BPLC cell [108]

From Fig. 5.7, it shows the BPLC has the larger thermal index gradient in BPII, -

0.00123/°C, which is smaller than the nematic liquid crystals. In addition, generally in nematic liquid crystal, there are two different polarization dependent index changes. Among them, $dn_{\parallel}/dt$ is negative while $dn_{\perp}/dt$ is positive. When the nematic liquid crystals turn isotropic, the index gradient is negative, owing $dn_{\parallel}/dt$ is negative. In BPLC, without polarization dependent properties, the index gradient is negative in three phases. At 35°C, the refractive index is 1.556 whereas 1.564 at 25°C. We can calculate the refractive index in all temperature range with the thermal index gradient curve. Since we have the refractive index information of BPLC, we can apply them in some application. I will discuss the application in image pixels and limiting effect inside fiber array later.

5.3 Grating Diffraction with Dye-Doped BPLCs

The doped BPLC mixture used in our studies consists of three ingredients: E48 (32%), 5CB (32%) and S811 (36%) as reported previously [109]. The MR-dye concentration used is < 0.1%. The transmission of a 100μm sample at 532nm is around 80% in the isotropic phase, corresponding to an absorption constant around $20cm^{-1}$.

In our diffraction experiment, a cw polarized 532nm laser is used. Two coherent lasers overlap on the BPLC sample at a mixing angle $\theta = 0.012$. First, there is no wave mixing diffraction with the undoped BPLC in the low power of cw laser. However, with MR-doped BPLC, diffraction signal builds up in a slow rate in the low level of laser power (22mW), depicted as Fig. 5.8. Around 2.5 minutes, the diffraction signal reaches the maximum. With good thermal control, the diffraction signal will be maintained for a long term. When the sample is heated up to isotropic phase or cooled down to crystal phase, the diffraction signal vanishes since the grating is broken.

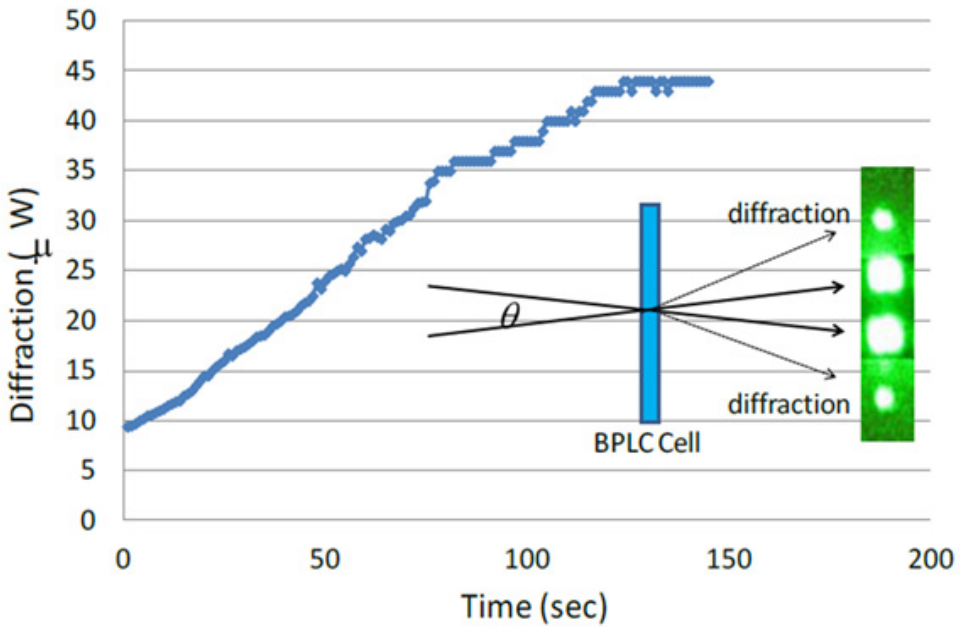

Fig. 5.8 Dynamic evolution of the first order diffraction signal from a 100-μm thick BPLC cell [109]

With 100μm dye doped BPLC, the power of ND:YAG laser is as low as 34mW, we measure the 1st order diffraction signal whose power is 193uW. The efficiency is around 0.57%. In addition, the 5th order diffraction also appears in this setup, shown as Fig. 5.9. Instead of reading the signal from the source, we also used the probe beam (632nm) to read the formation of grating inside the sample. As illustrated in Fig. 5.10, the 2nd order diffraction patterns can be read with the probe beam.

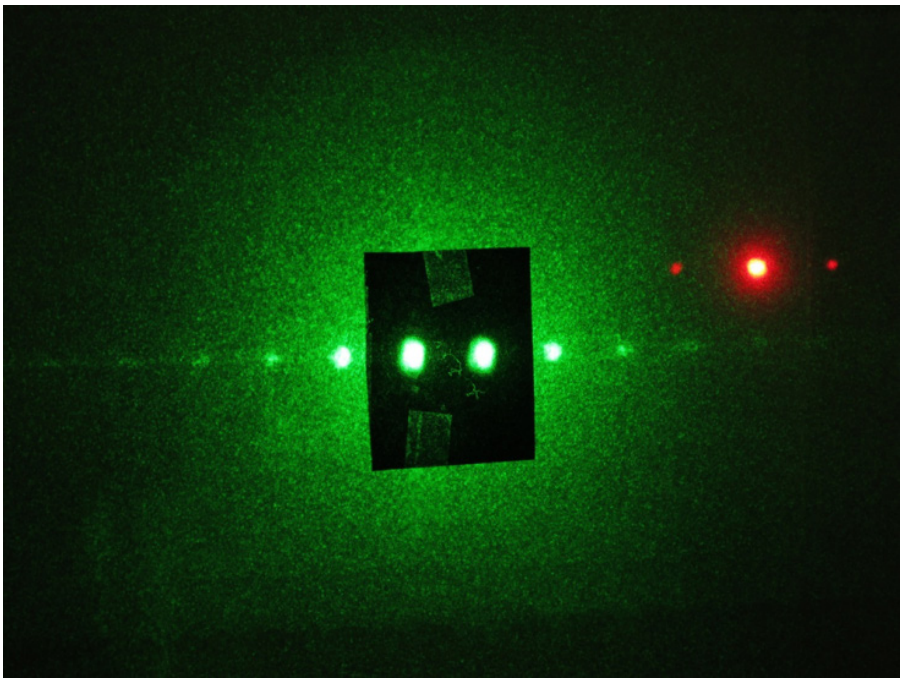

Fig. 5.9 A photograph of the observed transmitted pump and higher-order diffracted beam

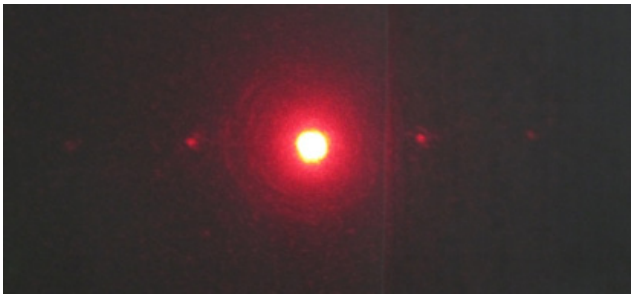

Fig. 5.10 A photograph of the observed diffracted probe beam

The transient and persistent contributions to the diffraction signals may come from mechanisms such as order parameter change and intermolecular torque from photo-excited trans-cis isomorphism. The real mechanism needs to be further examined. However, the thermal effect can be eliminated in this grating formation, since the thermal index relax is quite fast. In this setup, we try to block one path of two interference beams. The diffraction signal remains for more than ten seconds and then gradually disappears.

In addition, there are two things we make sure about this diffraction experiment. One is the photo absorption with the existence of dye molecules. The other is the dependence on the pump beam power. From Fig. 5.11, data in solid squares are obtained after pump illumination of a few seconds; those in crosses are for longer illumination when the signals become significantly stronger. Both types of diffraction signals exhibit rather nonlinear dependence on the pump beam power.

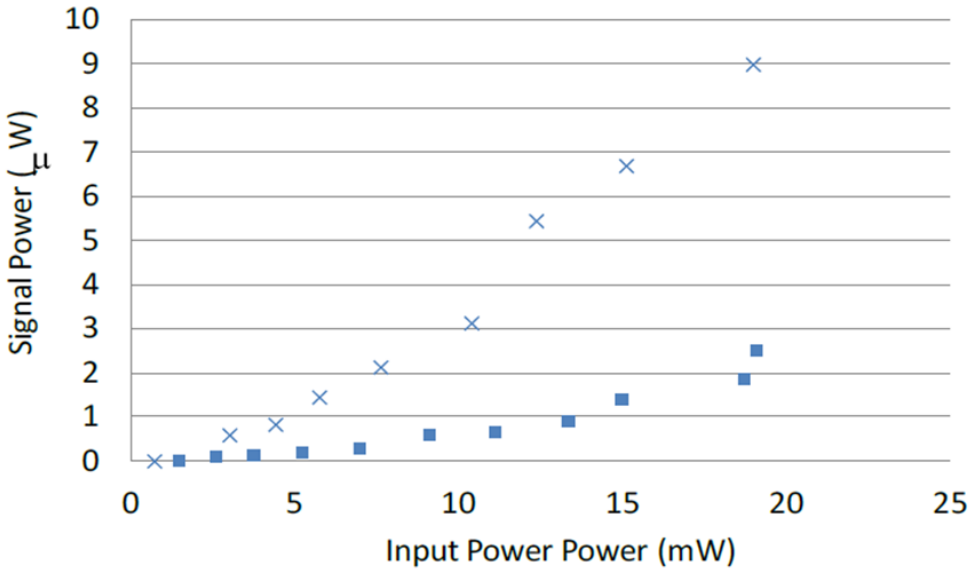

Fig. 5.11 Dependence of the transient diffraction signal on the pump power [109]

Furthermore, we discuss the relationship between the wave mixing angle and diffraction signal, the signal is quadratic dependent on the grating constant Λ^2. While $\Lambda \sim \lambda/\theta$ for a small angle $\theta \ll 1$, the experimental results from Fig. 5.12 are in a good agreement with this formula. Meanwhile, the blue phase liquid crystal is polarization independent so the diffraction signal is insensitive to the rotation of the BPLC sample.

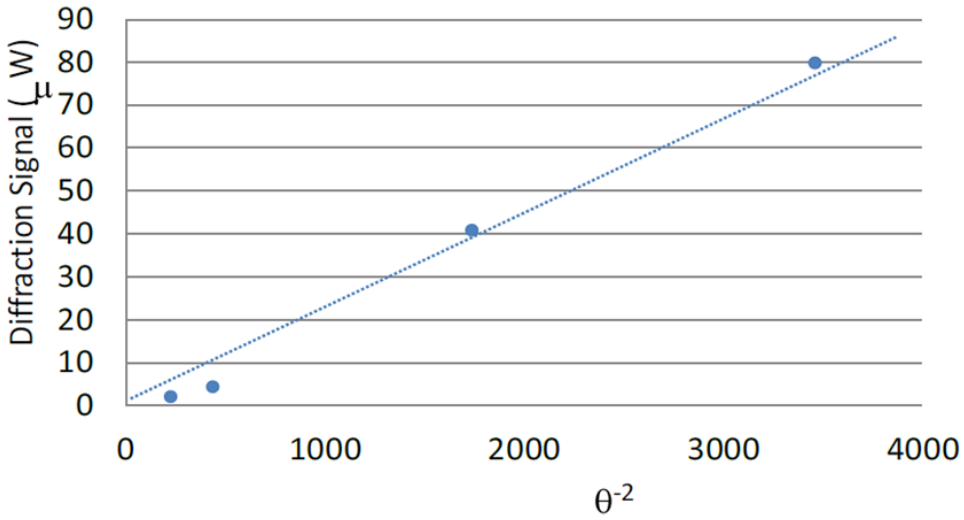

Fig. 5.12 Diffraction signal plotted as a function of θ^{-2} [109]

5.4 Fiber Array Image with BPLCs

A fiber array [core diameter: 10μm; fiber length: 3mm] functions as image transmitting faceplate. From Fig. 5.13, we observe the reflection from the fiber ends through the microscope. Because the temperature is around 25˚C, the phase of BPLC is in BPI regime, strongly reflecting the green color. For a fiber array, the pixel size determines the resolution of an image. The cladding of fiber array we used is 5μm. Therefore, the resolution of fiber array is up to 60 lines/mm. From Fig. 5.14 (b) upper part, the BPLC fiber array is in isotropic phase. Except for the defect in the fiber array, we can see the light perfectly transmit in all visible wavelength range, red, green, and blue. However, we can see the difference in the lower one. We estimate the temperature is between BPII and BPI. The white part turns yellow, a combination of green and red, whereas the white is constitue of RGB. Look into the blue part. Originally the perfectly transmitted hole turns dark. The same condition happens in some parts of green while the red part keeps unchanged in two different temperatures. With BPLC fiber array, we can apply it on some color filter or thermal sensor.

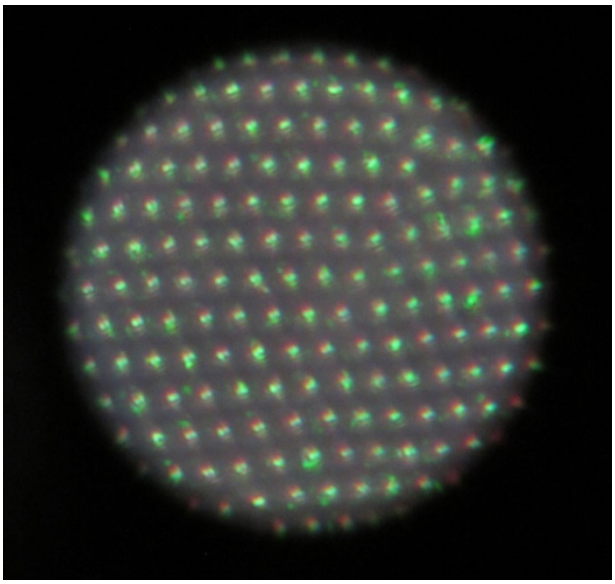

Fig. 5.13 Microscope photograph of one endface of the BPLC fiber array illuminated by obliquely incident white light showing green reflections from the fiber ends; ambient temperature is 25°C (BPI phase)

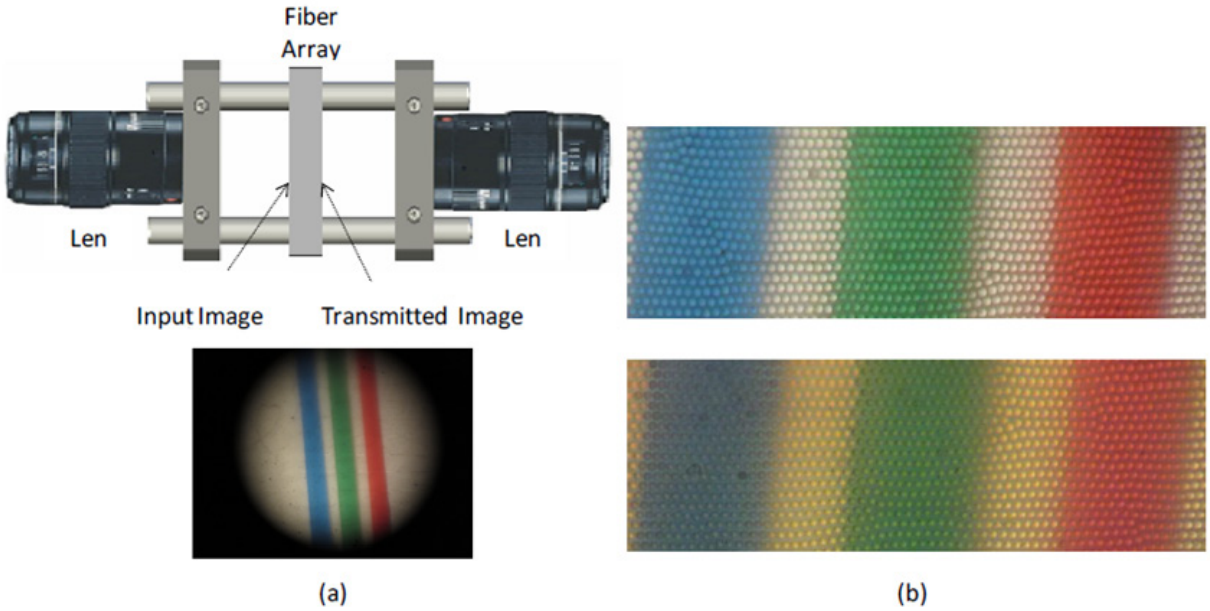

Fig. 5.14 (a) Experimental set up where a fiber array is inserted in the image plane inside a 1x telescope (b) Transmitted images under different phases [108]

5.5 Fiber Array Switching with BPLCs

BPLC fiber array can also be used as an intensity dependent switcher. The dimension of the fiber core is 30μm, allowing multi-modes laser to propagate through. The refractive index of the fiber core is around 1.47 while the refractive index of BPLC at 25°C is 1.564. After the laser couples into the fiber core, light propagates inside the fiber core, obeying the total internal reflection. If we put the BPLC inside the fiber array, the absorption induced thermal effect will decrease the refractive index in the core. Therefore, it will reduce the core guiding modes as some modes leakage into the cladding. As a result, the transmitted light through the center core decreases and leakages into surrounding fibers. The phenomenon can be treated as self-defocusing. The prerequisite is that the power of input laser should be large enough while the BPLC absorbs little in the visible and near infrared.

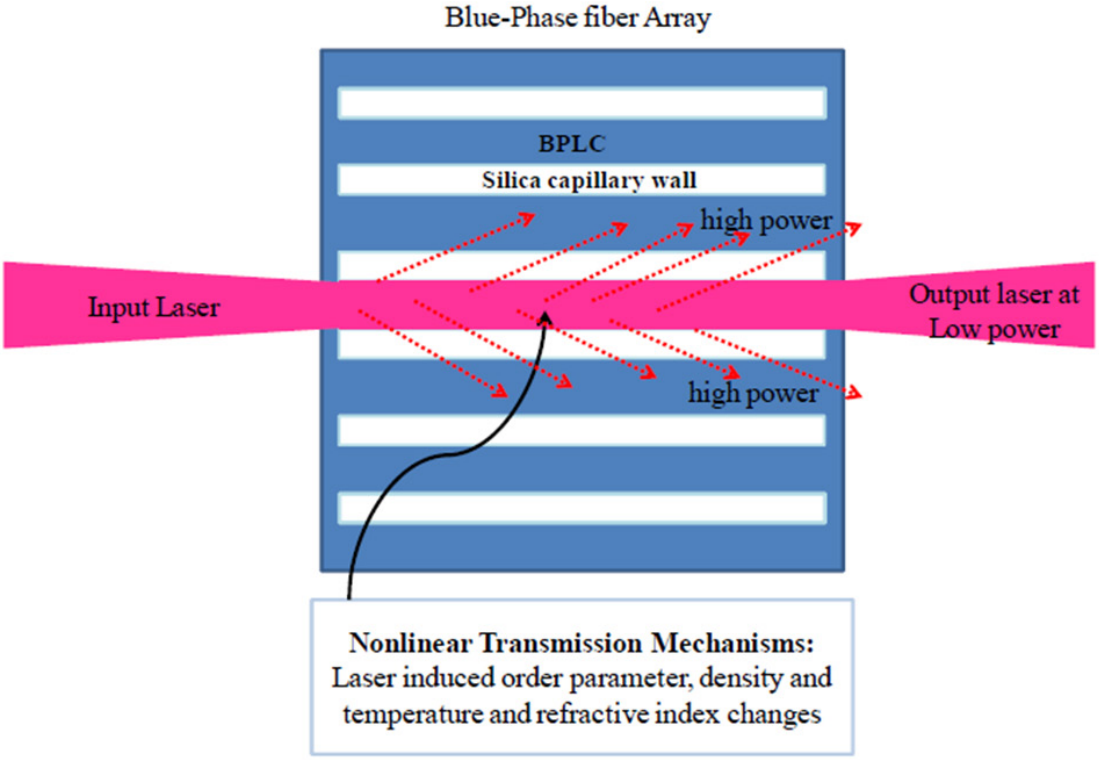

Fig. 5.15 Schematic depiction of some nonlinear optical absorption and scattering processes[108]

From Fig. 5.16, there are two results to explain the fiber array limiting behavior further. First, the case 1, the fiber array is kept above clearing point (35°C). The curve 1 starts at a relatively high transmission around 16%. When the input power increases, the transmission drops continuously. When the power reaches the maximum 2.5W, the transmission reduces below 1%, which is a well-defined limiter. The other case, the fiber array is kept in room temperature around 24°C, which the BPLC should be below BPI phase. In the chiral highly scattering phase, the transmission is extremely low. When the input power increases, the transmission also increases. At this period, the BPLC turns from BPI to BPII, where no high scattering happen so the transmission rises. However, around 0.5W, the fiber is heated through the isotropic phase; the following curve is similar to case 1 with the same mechanism. The slight difference of transmission at high input power in these two curves majorly comes from the heat needed to maintain the temperature in case 2. The three photos in the right side in Fig. 5.15 depict the mechanism clearly. At low power, the laser propagates through the fiber core perfectly. When the power increases, more laser leakages out because of the ability of guidance.

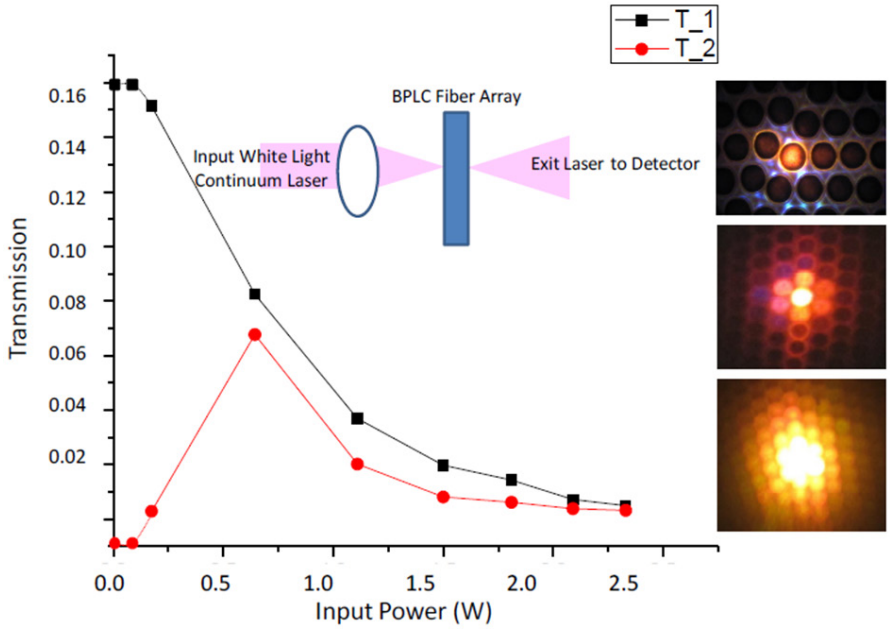

Fig. 5.16 Plots of the core transmission data as a function of the input laser power [108]

The laser we used here is the supercontinuum laser, whose spectrum under different powers is illustrated as Fig. 5.17.

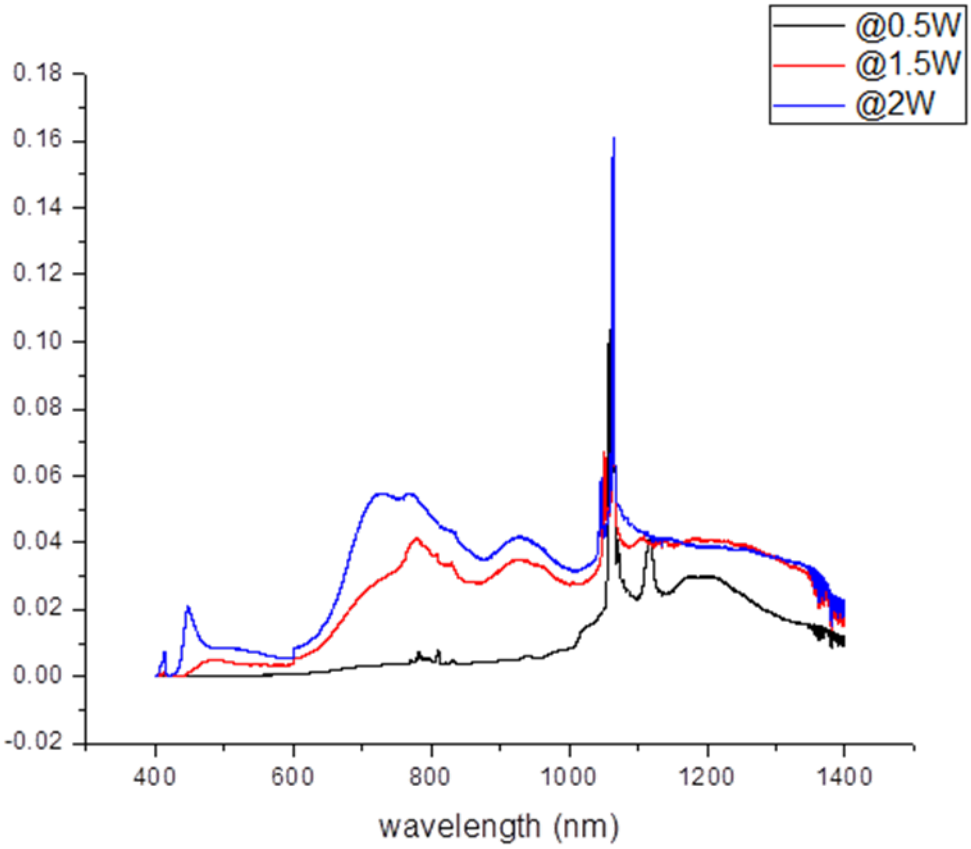

Fig. 5.17 The spectra of the super continuum under different powers

Furthermore, we used another 1mm pure BPLC bulk to prove the self-defocusing mechanism. We applied a lens to focus the light into the bulk sample and observed the output patterns. Fig. 5.18 (a) is the input beam profile whose power is around 1W and Fig. 5.18 (b) is the output beam profile. It is obvious that the center is dark and there is a bright ring outside, which is in agreement with the result of BPLC fiber array.

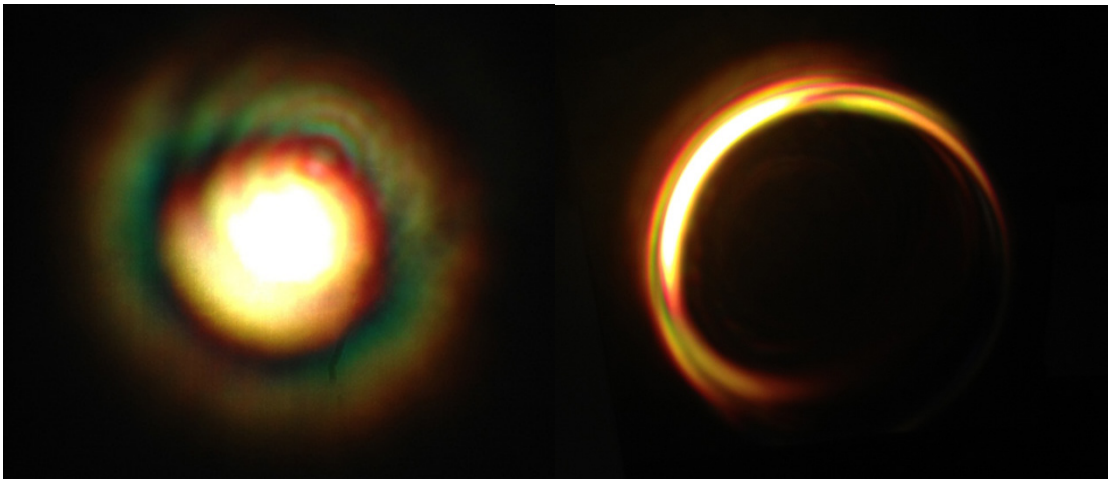

(a) (b)

Fig. 5.18 (a) Input beam and (b) output beam in BPLC fiber array self-defocusing

CHAPTER 6 SUMMARY AND FUTURE WORK

6.1 Summary

In this dissertation, I divide my research into three main topics. The first one is to understand the complicated mechanism of refractive index change in liquid crystals. To solve the electrostrictive coupled equations help investigate the nonlinear behavior. Liquid Crystals whose physical properties such as temperature, density, molecular orientation, electronic structure etc., are easily perturbed by an applied optical field are defined as highly nonlinear materials. Based on previous experiments and simulation done by many groups around the world, we try to add and strengthen the insufficient and weak part, the laser induced density effect with both digital simulation and lab experiments. So far, we have a huge progress on this part. In the limiting experiment with nano-second pulse laser, the liquid crystals show density change contribution to the refractive index change. Also, we have preliminary simulation result in a good agreement with the experiments.

The second is to use nonlinear nematic liquid crystals on image processing. The image processing discussed is divided into two parts: intensity inversion and wavelength conversion. For intensity inversion, we present a simple but efficient demonstration with dye-doped liquid crystals. Without other inputs or trigger sources, the all-optical dynamic process is only around 50μs. In addition, with the supra nonlinear liquid crystal, the input power needed to achieve the efficiency of intensity inversion is below 50 μW. In addition, we observe the intensity inversion and edge enhancement with the twisted nematic liquid crystals. For wavelength conversion, we proposed a simple real-time IR detector. With planar Epolight1125-doped LC, we successfully read the invisible signal in a visible way for the first time. Also, two different reading modes are provided because of the polarization dependent properties of thermal index. The IR power as low as 1.5mW can be read in this experiment. In addition, different parameters, such as thickness, substrates,

input intensity, and polarization are reported in this article. The response time in this passive image system is measured down to 60ms.

The last part is the new material, blue phase liquid crystals. The properties are totally different from the nematic liquid crystals though the formation of blue phase liquid crystals is to apply chiral agents in nematic liquid crystal host. The blue phase exhibits selective Bragg reflections of visible light because of its spontaneously self-assembled three dimensional cubic structures with lattice periods of several hundred nanometers. Also, polarization-independent and easy fabricate are the advantages of blue phase liquid crystals. We study the nonlinearity of blue phase liquid crystals with wave mixing, limiting, and fiber array image experiments to have further understanding of this new material.

6.2 Future Work

In the future, we still need to put more effort in these three areas. About the laser induced density effect, we understand the relationship between the laser intensity and the density change by solving the electrostrictive coupled equations. However, the relationship between the density change and refractive index change still need to explore. The density induced flow inside the liquid crystals is the next task. Once all of the related effects are well understood, we can say that we can control the optical behavior of liquid crystals.

On the other hand, image processing with nonlinear liquid crystals are very important currently. Liquid crystals can be investigated to develop some passive optical components since its large nonlinearity. Liquid crystal lens, for example, is a very successful and mature component. In this thesis, we have successfully read the invisible image with the visible probe. This technology can be applied to any wavelength regime with appropriate dopants. The doped liquid crystals can also be used for medical

detection because of the variety and sensitivity. There are many possible applications to use liquid crystals in image processing.

The blue phase liquid crystals are still under development. Therefore there are still a lot waiting for exploration because of the special optical properties resulting from the spontaneously self-assembling periodic helical structures. Recently, we tried to put this special material into photonic crystal fibers since the self-assembled lattice periods of several hundred nanometers. With the combination of photonic crystal fiber and blue phase liquid crystals, the band gap range and shift will be interesting. There are some groups investigating in this structure and applying some electric fields. 2-dimention or 3-dimension BPLC-PCF will be foreseen as a fascinating research topic.

REFERENCES

[1] F. Reinitzer, “Beiträge zur kenntniss des cholesterins,” *Monatshefte für Chemie*, vol. 9, pp. 421–441, 1888.

[2] G. Friedel, “Mesomorphic states of matter,” *Annales de Physique*, vol. 18, pp. 273, 1922.

[3] “The Nobel prize in physics 1991.” [Online]. Available: http://nobelprize.org/nobel_prizes/physics/laureates/1991/.

[4] P.-G. DeGennes, The physics of liquid crystals, Clarendon: Oxford Press, 1974.

[5] I. C. Khoo, J.-H. Park, and J. Liou, “All-optical switching of continuous wave, microsecond lasers with a dye-doped nematic liquid crystal,” *Applied Physics Letters*, vol. 90, no. 15, pp. 151107, 2007.

[6] L. W. Tutt. and T. F. Boggess, “A review of optical limiting mechanisms and devices using organics, fullerenes, semiconductors and other materials,” *Progress in Quantum Electronics*, vol. 17, no. 4, pp. 299–338, 1993.

[7] K. M. Nashold and D. P. Walter, “Investigations of optical limiting mechanisms in carbon particle suspensions and fullerene solutions,” *Journal of the Optical Society of America B-Optical Physics*, vol. 12, no. 7, pp. 1228–1237, 1995.

[8] I. C. Khoo, M. Wood, M. Y. Shih, and P. Chen, “Extremely nonlinear photosensitive liquid crystals for image sensing and sensor protection,” *Optics Express*, vol. 4, no. 11, pp. 432–442, 1999.

[9] I. C. Khoo, R. R. Michael, and G. M. Finn, “Self-phase modulation and optical limiting of a low-power CO2 laser with a nematic liquid-crystal film,” *Applied Physics Letters*, vol. 52, no. 25, pp. 2108–2110, 1988.

[10] I. C. Khoo, D. H. Werner, X. Liang, A. Diaz, and B. Weiner, “Nanosphere dispersed liquid crystals for tunable negative-zero-positive index of refraction in the optical and terahertz regimes,” *Optics Letters*, vol. 31, no. 17, pp. 2592–2594, 2006.

[11] Q. Zhao, L. Kang, B. Du, B. Li, J. Zhou, H. Tang, X. Liang, and B. Zhang, "Electrically tunable negative permeability metamaterials based on nematic liquid crystals," *Applied Physics Letters*, vol. 90, no. 1, pp. 011112, 2007.

[12] I. C. Khoo, A. Diaz, J. Liou, M. V. Stinger, J. Huang, and Y. Ma, "Liquid Crystals Tunable Optical Metamaterials," *Selected Topics in Quantum Electronics, IEEE Journal of*, vol. 16, no. 2, pp. 410–417, 2010.

[13] F. Du, Y.-Q. Lu, and S.-T. Wu, "Electrically tunable liquid-crystal photonic crystal fiber," *Applied Physics Letters*, vol. 85, no. 12, pp. 2181–2183, 2004.

[14] M. W. Haakestad, T. T. Alkeskjold, M. D. Nielsen, L. Scolari, J. Riishede, H. E. Engan, and A. Bjarklev, "Electrically tunable photonic bandgap guidance in a liquid-crystal-filled photonic crystal fiber," *Photonics Technology Letters, IEEE*, vol. 17, no. 4, pp. 819–821, 2005.

[15] C. W. Chen, H. C. Jau, C. T. Wang, C. H. Lee, I. C. Khoo, and T. H. Lin, "Random lasing in blue phase liquid crystals," *Optics Express*, vol. 20, no. 21, pp. 23978-23984, 2012.

[16] H. Coles and M. N. Pivnenko, "Liquid crystal 'blue phases' with a wide temperature range," *Nature*, vol. 436, no. 7053, pp. 997–1000, 2005.

[17] C. T. Wang, H. C. Jau, and T. H. Lin, "Bistable cholesteric-blue phase liquid crystal using thermal hysteresis," *Optical Materials*, vol. 34, no. 1, pp. 248–250, 2011.

[18] Y. Hisakado, H. Kikuchi, T. Nagamura, and T. Kajiyama, "Large Electro-optic Kerr Effect in Polymer-Stabilized Liquid-Crystalline Blue Phases," *Advanced Materials*, vol. 17, no. 1, pp. 96–98, 2004.

[19] S. Chandrasekhar, Liquid Crystals. 2nd ed. Cambridge: Cambridge University Press, 1992.

[20] A. Ciferri, W. R. Krigbaum, and R. B. Meyer, Polymer liquid crystals, Academic Press, 1982.

[21] G. W. Gray, K. J. Harrison, and J. A. Nash, "New family of nematic liquid crystals for displays," *Electronics Letters*, vol. 9, no. 6, pp. 130–131, 1973.

[22] P. J. Collings and M. Hird, Introduction to liquid crystals: chemistry and physics (Vol. 1), CRC, 1997.

[23] S. T. Wu, D. Coates, and E. Bartmann, "Physical properties of chlorinated liquid crystals," *Liquid Crystals*, vol. 10, no. 5, pp. 635–646, 1991.

[24] A. Golemme, B. L. Volodin, B. Kippelen, and N. Peyghambarian "Photorefractive polymer-dispersed liquid crystals," *Optics Letters*, vol. 22, no. 16, pp. 1226–1228, 1997.

[25] G. P. Wiederrecht and M. R. Wasielewski, "Photorefractivity in polymer-stabilized nematic liquid crystals," *Journal of the American Chemical Society*, vol. 120, no. 13, pp. 3231–3236, 1998.

[26] I. C. Khoo, Yana Zhang Williams, B. Lewisb, and T. Malloukb, "Photorefractive CdSe and Gold Nanowire-Doped Liquid Crystals and Polymer-Dispersed-Liquid-Crystal Photonic Crystals," *Molecular Crystals and Liquid Crystals*, vol. 446, no. 1, pp. 233–244, 2006.

[27] S. Kobayashi, T. Miyama, N. Nishida, Y. Sakai, H. Shiraki, Y. Shiraishi, and N. Toshima, "Dielectric spectroscopy of metal nanoparticle doped liquid crystal displays exhibiting frequency modulation response," *Display Technology, Journal of*, vol. 2, no. 2, pp. 121–129, 2006.

[28] I. C. Khoo, Liquid crystals, 2nd ed. New Jersey: Wiley-Interscience, 2007.

[29] S. M. Kelly and M. O'Neill, "Liquid Crystals for electro-optic applications", Handbook of Advanced Electronic and Photonic Materials and Devices, Volume 7: Liquid Crystals, Display and Laser Materials, 2000.

[30] S. Jen, N. A. Clark, P. S. Pershan, and E. B. Priestley, "Polarized Raman-scattering studies of orientational order in uniaxial liquid-crystalline phases," *The Journal of Chemical Physics*, vol. 66, pp. 4635–4661, 1977.

[31] C. H. Gooch and H. A. Tarry, “Optical-properties of twisted nematic liquid-crystal structures with twist angles less than 90 degrees,” *Journal of Physics D-Applied Physics*, vol. 8, no. 13, pp. 1575-1584, 1975.

[32] F. C. Frank, “I. Liquid crystals. On the theory of liquid crystals,” *Discussions of the Faraday Society*, vol. 25, pp. 19-28, 1958.

[33] Figure is from Institut für Theoretische Physik, TU Berlin http://wwwitp.physik.tu-berlin.de/muschik/liquid_crystals/lc_intro.html

[34] G. Barbero, F. Simoni, and P. Aiello, “Nonlinear optical reorientation in hybrid aligned nematics,” *Journal of applied physics*, vol. 55, no. 2, pp. 304–311, 1984.

[35] S. Faetti, I. C. Khoo, and F. Simoni, Physics of liquid crystalline materials, Gordon and Breach, Philadelphia, 301, 1991.

[36] I. C. Khoo, “Optically induced molecular reorientation and third-order nonlinear optical processes in nematic liquid crystals,” *Physical Review A*, vol. 23, no. 4, pp. 2077, 1981.

[37] S. D Durbin, S. M. Arakelian, and Y. R. Shen, “Laser-induced diffraction rings from a nematic-liquid-crystal film,” *Optics Letters*, vol. 6, no. 9, pp. 411-413, 1981.

[38] I. C. Khoo, R. G. Lindquist, R. R. Michael, R. J. Mansfield, and P. G. LoPresti, “Dynamics of picosecond laser-induced density, temperature, and flow-reorientation effects in the mesophases of liquid crystals,” *Journal of Applied Physics*, vol. 69, no. 7, pp. 3853-3859, 1991.

[39] N. V. Tabiryan, A. V., Sukhov, and B. YA, “Orientational optical nonlinearity of liquid crystals. Molecular Crystals and Liquid Crystals,” *Molecular Crystals and Liquid Crystals*, vol. 136, no. 1, pp. 1–139, 1986.

[40] E. V. Rudenko and A. V. Sukhov, “Optically induced spatial charge separation in a nematic and the resultant orientational nonlinearity,” *Soviet Journal of Experimental and Theoretical Physics*, vol. 78, pp. 875-882, 1994.

[41] I. C. Khoo, H. Li, and Y. Liang, "Observation of orientational photorefractive effects in nematic liquid crystals," *Optics Letters*, vol. 19, no. 21, pp. 1723, 1994.

[42] H. Ono and N. Kawatsuki, "Orientational photorefractive effects observed in polymer-dispersed liquid crystals," *Optics letters*, vol. 22, no. 15, pp. 1144-1146, 1997.

[43] I. C. Khoo, H. Li, and Y. Liang, "Optically induced extraordinarily large negative orientational nonlinearity in dye-doped liquid crystal," *IEEE Journal of Quantum Electronics*, vol. 29, no. 5, pp. 1444-1447, 1993.

[44] I. C. Khoo, "Orientational photorefractive effects in nematic liquid crystal films," *Quantum Electronics, IEEE Journal of*, vol. 32, no. 3, pp. 525-534, 1996.

[45] I. Janossy, L. Csillag, and A. D. Lloyd, "Temperature dependence of the optical Freedericksz transition in dyed nematic liquid crystals," *Physical Review A*, vol. 44, no. 12, pp. 8410-8413, 1991.

[46] I. C. Khoo, S. Slussarenko, B. D. Guenther, M.-Y. Shih, P. Chen, and W. V. Wood, "Optically induced space-charge fields, dc voltage, and extraordinarily large nonlinearity in dye-doped nematic liquid crystals," *Optics Letters*, vol. 23, no. 4, pp. 253-255, 1998.

[47] I. C. Khoo, Extreme nonlinear optics of nematic liquid crystals [Invited]. JOSA B, vol. 28, no. 12, A45-A55, 2011.

[48] G. K. Wong, and Y. R. Shen, "Study of pretransitional behavior of laser-field-induced molecular alignment in isotropic nematic substances," *Physical Review A*, vol. 10, no. 4, pp. 1277, 1974.

[49] C. Flytzanis and Y. R. Shen, "Molecular theory of orientational fluctuations and optical Kerr effect in the isotropic phase of a liquid crystal," *Physical Review Letters*, vol. 33, no. 1, pp. 14-17, 1974.

[50] D. N. Rao and S. Jayaraman, "Pretransitional behavior of self-focusing in nematic liquid crystals," *Physical Review A*, vol. 10, no. 6, pp. 2457, 1974.

[51] J. Prost and J. R. Lalanne, "Laser-induced optical Kerr effect and the dynamics of orientational order in the isotropic phase of a nematogen," *Physical Review A*, vol. 8, pp. 2090-2093, 1973.

[52] I. C. Khoo, A. Diaz, and J. Ding, "Nonlinear-absorbing fiber array for large-dynamic-range optical limiting application against intense short laser pulses," *JOSA B*, vol. 21, no. 6, pp. 1234-1240, 2004.

[53] I. C. Khoo, "Liquid Crystal Fiber Array for Optical Limiting of Laser Pulses and for Eye/Sensor Protection," U.S. Patent 5, 589, 101, 1996.

[54] I. C. Khoo, M. V. Wood, B. D. Guenther, M.-Y. Shih, and P. H. Chen, "Nonlinear-absorption and optical limiting of laser pulses in a liquidcored fiber array," *J. Opt. Soc. Amer*., vol. B15, pp. 1533–1540, 1998.

[55] G. P. Agarwal, Nonlinear Fiber Optics, San Diego, CA: Academic, 1989.

[56] I. C. Khoo, A. Diaz, M. V. Wood, and P. H. Chen, "Passive optical limiting of picosecond-nanosecond laser pulses using highly nonlinear organic liquid cored fiber array," *Selected Topics in Quantum Electronics, IEEE Journal of*, vol. 7, no. 5, pp. 760-768, 2001.

[57] I. C. Khoo, P. H. Chen, M. V. Wood, and M.-Y. Shih, "Molecular photonics of a highly nonlinear organic fiber core liquid for picosecond–nanosecond optical limiting effect," *Chem. Phys.*, vol. 245, pp. 517–531, 1999.

[58] I. P. Batra, R. H. Enns, and D. Pohl, "Stimulated thermal scattering of light," *Phys. Status Solidi (b)*, vol. 48, no. 1, pp. 11-63, 1971.

[59] H. J. Eichler, P. Gunter, and D. W. Pohl, Laser Induced Dynamic Grating, Berlin: Springer-Verlag, 1986.

[60] W. H. DeJeu and P. Bordewijk, "Physical studies of nematic azoxybenzenes. II. Refractive indices and the internal field," *The Journal of Chemical Physics*, vol. 68, pp. 109, 1978.

[61] I. C. Khoo and R. Normandin, "The mechanism and dynamics of transient thermal grating diffraction in nematic liquid crystal film," *IEEE J. Quantum Electronics*, *IEEE Journal of*, vol. 21, no. 4, pp. 329-335, 1985.

[62] C. S. Yelleswarapu, S. R. Kothapalli, and D. V. G. L. N. Rao, "Optical Fourier techniques for medical image processing and phase contrast imaging," *Optics Communications*, vol. 281, no. 7, pp. 1876-1888, 2008.

[63] C. S. Yelleswarapu, S. R. Kothapalli, F. J. Aranda, D. V. G. L. N. Rao, Y. R. Vaillancourt, and B. R. Kimball, "Phase contrast imaging using photothermally induced phase transitions in liquid crystals," *Applied Physics Letters*, vol. 89, no. 21, pp. 211116-211116, 2006.

[64] A. Y. G. Fuh and T. H. Lin, Spatial filters based on azo-dye-doped liquid crystal films, *In Integrated Optoelectronic Devices 2007*, International Society for Optics and Photonics, pp. 65870W-65870W, 2007.

[65] M. Eich, J. H. Wendorff, B. Reck, and H. Ringsdorf, "Reversible digital and holographic optical storage in polymeric liquid crystals," *Die Makromolekulare Chemie, Rapid Communications*, vol. 8, no. 1, pp. 59-63, 1987.

[66] A. G. Chen and D. J. Brady, "Real-time holography in azo-dye-doped liquid crystals," *Optics Letters*, vol. 17, no. 6, pp. 441-443, 1992.

[67] T. J. Bunning, L. V. Natarajan, V. Tondiglia, R. L. Sutherland, D. L. Vezie, and W. W. Adams, "The morphology and performance of holographic transmission gratings recorded in polymer dispersed liquid crystals," *Polymer*, vol. 36, no. 14, pp. 2699-2708, 1995.

[68] R. G. Horn, "Refractive indices and order parameters of two liquid crystals," *Journal de Physique*, vol. 39, no. 1, pp. 105-109, 1978.

[69] J. Li and Y. T. Chen, Computational partial differential equations using MATLAB, Chapman & Hall/CRC, 2009.

[70] D. R. Lynch and W. G. Gray, “A wave equation model for finite element tidal computations,” *Computers & fluids*, vol. 7, no. 3, pp. 207-228, 1979.

[71] J. W. Goodman, Introduction to Fourier Optics, 3rd ed. New York: McGraw-Hill, 1996.

[72] G. Wernicke, S. Krtiger, J. Kamps, H. Gruber, N. Demoli, M. Dtirr, and S. Teiwes, “Application of a liquid crystal display spatial light modulator system as dynamic diffractive element and in optical image processing,” *Journal of Optical Communications*, vol. 25, no. 4, pp. 13-20, 2012.

[73] H. Zhang, D. Song, P. Wen, S. Esener, and A. Hμsain, “Optical image inversion and edge detection based on Vertical Cavity Semiconductor Optical Amplifiers (VCSOAs),” in Information Photonics, pp. 2-4, 2005.

[74] P. Gunter and J. P. Huignard, Photorefractive Materials and Their Applications Vols. 1 2 3, 1st ed. Berlin: Springer-Verlag, 1989.

[75] I. C. Khoo, “Nonlinear optics of liquid crystalline materials,” *Physics Reports*, vol. 471, no. 5, pp. 221-267, 2009.

[76] H. Ono, T. Kawamura, N. Kawatsuki, and H. Norisada, “Intensity filtering of a two-dimensional optical image in high-performance photorefractive mesogenic composites,” *Applied Physics Letters*, vol. 79, no. 7, pp. 895, 2001.

[77] A. Y.-G. Fuh and T.-H. Lin, “Electrically switchable spatial filter based on polymer-dispersed liquid crystal film,” *Journal of Applied Physics*, vol. 96, no. 10, pp. 5402, 2004.

[78] I. C. Khoo, M. Y. Shih, M. V. Wood, and P. H. Chen, “Extremely nonlinear photosensitive nematic liquid crystal film,” *Synthetic Metals*, vol. 115, no. 1, pp. 145-150, 2000.

[79] F. Simoni, L. Lucchetti, D. Lucchetta, and O. Francescangeli, “On the origin of the huge nonlinear response of dye-doped liquid crystals,” *Optics Express*, vol. 9, no. 2, pp. 85-90, 2001.

[80] M. Y. Shih, A. Shishido, P. H. Chen, M. V. Wood, and I. C. Khoo, "All-optical image processing with a supranonlinear dye-doped liquid-crystal film," *Optics Letters*, vol. 25, no. 13, pp. 978-980, 2000.

[81] I. C. Khoo, K. Chen, and A. Diaz, "All-optical neural-net-like image processing with photosensitive nonlinear nematic film," *Optics Letters*, vol. 28, no. 23, pp. 2372-2374, 2003.

[82] M. Y. Shih, A. Shishido, and I. C. Khoo, "All-optical image processing by means of a photosensitive nonlinear liquid-crystal film: edge enhancement and image addition-subtraction," *Optics Letters*, vol. 26, no. 15, pp. 1140-1142, 2001.

[83] T. Ikeda and O. Tsutsumi, "Optical switching and image storage by means of azobenzene liquid-crystal films," *Science (New York, N.Y.)*, vol. 268, no. 5219, pp. 1873–1875, 1995.

[84] T. R. Wolinski, A. Jarmolik, and W. J. Bock, "Development of fiber optic liquid crystal sensor for pressure measurement," *Instrumentation and Measurement, IEEE Transactions on*, vol. 48, no. 1, pp. 2-6, 1999.

[85] P. Yeh and C. Gu, Optics of Liquid Crystal Displays, 2009.

[86] T. Ikeda, "Photomodulation of liquid crystal orientations for photonic applications," *Journal of Materials Chemistry*, vol. 13, no. 9, pp. 2037, 2003.

[87] K. M. Johnson, M. A. Handschy, and L. A. Pagano-Stauffer, "Optical computing and image processing with ferroelectric liquid crystals," *Optical Engineering*, vol. 26, no. 5, pp. 265385-265385, 1987.

[88] I. C. Khoo, M. Kaczmarek, M. Y. Shih, M. V. Wood, A. Diaz, J. Ding, Y. Zhang, and J. Patel, "Nonlinear Optical Effects in Nematic Liquid – Crystal Films in the 1.55 um Spectral Region," *Molecular Crystals and Liquid Crystals*, vol. 374, no. 1, pp. 315–324, 2002.

[89] E. Wolf, "Electromagnetic diffraction in optical systems. I. An integral representation of the image field," *Proceedings of the Royal Society of London. Series A. Mathematical and Physical Sciences*, vol. 253, no. 1274, pp. 349-357, 1959.

[90] http://www.epolin.com

[91] K. M. Chen, S. Gauza, H. Xianyu, and S. T. Wu, "Hysteresis effects in blue-phase liquid crystals," *Display Technology, Journal of*, vol. 6, no. 8, pp. 318-322, 2010.

[92] S. Meiboom, J. P. Sethna, W. P. Anderson, and W. F. Brinkman, "Theory of the blue phase of cholesteric liquid crystals," *Physical Review Letters*, vol. 46, no. 18, pp. 1216-1219, 1981.

[93] Z. Ge, L. Rao, S. Gauza, and S. T. Wu, "Modeling of blue phase liquid crystal displays," *Journal of Display Technology*, vol. 5, no. 7, pp. 250-256, 2009.

[94] H. Y. Liu, C. T. Wang, C. Y. Hsu, T. H. Lin, and J. H. Liu, "Optically tuneable blue phase photonic band gaps," *Applied Physics Letters*, vol. 96, no. 12, pp. 121103-121103, 2010.

[95] C. T. Wang, H. Y. Liu, H. H. Cheng, and T. H. Lin, "Bistable effect in the liquid crystal blue phase," *Applied Physics Letters*, vol. 96, no. 4, pp. 041106-041106, 2010.

[96] R. M. Hornreich, S. Shtrikmans, and C. Sommers, "Photonic bands in simple and body-centered-cubic cholesteric blue phases," *Physical Review E*, vol. 47, no. 3, pp. 2067-2072, 1993.

[97] D. C. Right and N. D. Mermin, "Crystalline liquids: the blue phases," *Reviews of Modern Physics*, vol. 61, no. 2, pp. 385, 1989.

[98] S. Meiboom, M. Sammon, and D. W. Berreman, "Lattice of Disclinations: The Structure of the Blue Phases of Cholesteric Liquid Crystals," *Physical Review A*, vol. 27, no. 1, pp. 438, 1983.

[99] I. Dierking, Textures of liquid crystals, Wiley-VCH Verlag GmbH, 2003.

[100] H. Kitzerow and C. Bahr (Eds.), Chirality in Liquid Crystals, Springer, New York, 2001.

[101] Y. Chen, J. Yan, J. Sun, S. T. Wu, X. Liang, S. H. Liu, P. J. Hsieh, K. L. Cheng, and J. W. Shiu, "A microsecond-response polymer-stabilized blue phase liquid crystal," *Applied Physics Letters*, vol. 99, no. 20, pp. 201105-201105, 2011.

[102] K. M. Chen, S. Gauza, H. Xianyu, S. T. Wu, "Submillisecond gray-level response time of a polymer-stabilized blue-phase liquid crystal," *Journal of display technology*, vol. 6, no. 2, pp. 49-51, 2010.

[103] Z. Ge, S. Gauza, M. Jiao, H. Xianyu, and S.-T. Wu, "Electro-optics of polymer-stabilized blue phase liquid crystal displays," *Applied Physics Letters*, vol. 94, no. 10, pp. 101104-101104, 2009.

[104] S.-Y. Lu and L.-C. Chien, "Electrically switched color with polymer-stabilized blue-phase liquid crystals," *Optics Letters*, vol. 35, no. 4, pp. 562-564, 2010.

[105] H.-Y. Liu, C.-T. Wang, C.-Y. Hsu, and T.-H. Lin, "Pinning effect on the photonic bandgaps of blue-phase liquid crystal," *Applied Optics*, vol. 50, no. 11, pp. 1606-1609, 2011.

[106] J. Yan, H. C. Cheng, S. Gauza, Y. Li, M. Jiao, L. Rao, and S. T. Wu, "Extended Kerr effect of polymer-stabilized blue-phase liquid crystals," *Applied Physics Letters*, vol. 96, no. 7, pp. 071105-071105, 2010.

[107] H. Kikuchi, M. Yokota, Y. Hisakado, H. Yang, and T. Kajiyama, "Polymer-stabilized liquid crystal blue phases," *Nature Materials*, vol. 1, no. 1, pp. 64-68, 2002.

[108] I. C. Khoo, K. L. Hong, S. Zhao, D. Ma, and T. H. Lin, "Blue-phase liquid crystal cored optical fiber array with photonic bandgaps and nonlinear transmission properties," *Optics Express*, vol. 21, no. 4, pp. 4319-4327, 2013.

[109] I. C. Khoo and T. H. Lin, "Nonlinear optical grating diffraction in dye-doped blue-phase liquid crystals," *Optics Letters*, vol. 37, no. 15, pp. 3225-3227, 2012.

[110] I. Janossy and T. Kosa, "Influence of anthraquinone dyes on optical reorientation of nematic liquid crystals," *Optics Letters*, vol. 17, no. 17, pp. 1183-1185, 1992.

[111] H. Li, Y. Liang, and I. C. Khoo, "Transient laser induced orthogonal director-axis reorientation in dye-doped liquid crystals (DDLC)," *Molecular Crystals and Liquid Crystals*, vol. 251, no. 1, pp. 85-92, 1994.

[112] I. C. Khoo, J. Ding, Y. Zhang, K. Chen, and A. Diaz, "Supra-nonlinear photorefractive response of single-walled carbon nanotube-and C-doped nematic liquid crystal," *Applied Physics Letters*, vol. 82, pp. 3587, 2003.57

[113] L. Lucchetti, M. Gentili, and F. Simoni, "Effects leading to colossal optical nonlinearity in dye-doped liquid crystals," *Selected Topics in Quantum Electronics, IEEE Journal of*, vol. 12, no. 3, pp. 422-430, 2006.

[114] I. C. Khoo, M. Y. Shih, M. V. Wood, B. D. Guenther, P. H. Chen, F. Simoni, S. Slussarenko, O. Francescangeli, and L. Lucchetti, "Dye-doped photorefractive liquid crystals for dynamic and storage holographic grating formation and spatial light modulation," *Proceedings of the IEEE*, vol. 87, no. 11, pp. 1897-1911, 1999.

[115] D. Wei, A. Iljin, Z. Cai, S. Residori and U. Bortolozzo, "Two-wave mixing in chiral dye-doped nematic liquid crystals," *Optics Letters*, vol. 37, no. 4, pp. 734-736, 2012.

VITA

Kuan-Lun Hong

Kuan-Lun Hong was born in Taichung, Taiwan. He received his B.S. degree in Civil Engineering from National Chiao Tung University in 2003 and an M.S. degree in Electronic and Computer Engineering from National Taiwan University of Science and Technology in 2006. In August 2008, he joined Penn State University to pursue his Ph.D. in Electrical Engineering. He worked as a Research Assistant under the direction of Dr. Iam-Choon Khoo in the laboratory of Liquid Crystals and Nonlinear Optics Lab. He is a member of International society of for Optical Engineering (SPIE) and Optical Society of America (OSA).